Thermomechanical Response of Polycrystalline α -Uranium

A Dissertation

Presented to

the faculty of the School of Engineering and Applied Science

University of Virginia

---

in partial fulfillment

of the requirements for the degree
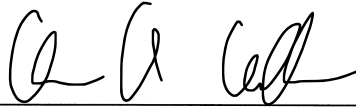
Doctor of Philosophy

by

Christopher A. Calhoun

August

2016

APPROVAL SHEET

The dissertation

is submitted in partial fulfillment of the requirements

for the degree of

Doctor of Philosophy

_____
AUTHOR

The dissertation has been read and approved by the examining committee:

Sean Agnew
Advisor

Jerrold Floro

_____

Matthew Panzer

_____

Baoxing Xu

_____

Marko Knezevic

_____

Elena Garlea

_____

Accepted for the School of Engineering and Applied Science:

Craig H. Benson, Dean, School of Engineering and Applied Science

August

2016

To: *Liviu Lebrescu and the other 31 Hokies that lost their lives on April 16, 2007.*

"Whereas mechanics is rigorous (and often unimaginative), materials tends to be descriptive and qualitative (and is often intuitive and innovative). Mechanics is rooted in mathematics, and its method can tackle difficult problems and provide insightful quantitative answers that are highly relevant. Materials is rooted in physics and chemistry and deals with problems that are immensely complex; in some ways, it resembles biology, which deals with organisms. The synthesis of these two disciplines is not an easy one"

M.A. Meyers, R. W. Armstrong, & H. O. K. Kirchner, <u>Mechanics and Materials</u> (1999)

Acknowledgements

First and foremost, I must thank the Creator for providing a beautiful balance of complexity in the world around us and the intellect within us to make this and all science possible. Secondly, I thank my family. Their support, both financial and emotional, has enabled any successes I've had and helped me to overcome any failures. Without my mom, dad, brother and extended family none of this work gets completed. I acknowledge my bride to be the stunning Ms. Guida. She has provided great balance in my life during the last leg of my PhD studies.

Sean Agnew has not only been a great technical advisor; he has also been a great role model/friend/mentor in life. I am truly grateful to have been a student of his for 4 years. I am lucky to have received a position in his group, and for this, I will be forever grateful. Our shared experiences will serve as the ammo for great advisor stories (particularly the lessons taught to intrusive groundhogs, and heavy metal group sound tracks) as well as life lessons. My lab mates in MechMet, Rupalee, Jishnu, Joha, Fulin, Matt and Robert have been great friends and co-workers by putting up with my smattering of questions and disruptions.

I would not have pursued a PhD had it not been for my high school calculus teacher, John Perrin. He started me on the path toward a PhD by teaching me that knowledge is something to be sought out rather then received. His guidance taught me that not all answers are in books, and some must be figured out on their own. That was the trailhead of the path toward this PhD and the rest of my research career. John started the passion for research, and my high school physics teacher, Don Rotsma, aimed that passion toward mechanical deformation. He showed me (at age 15-16) a sample tested at the University of Nevada Reno of a necked and broken steel tensile sample. I did not even get to see the test, but the image of what I now know as the classic cup-cone fracture surface served as the starting point for my passion in metal deformation and the pursuit of a career in the business of breaking metals. I recognize Norm Dowling who gave me the first paid position to break things, and Mark Stremler who provided valuable advice during my undergraduate days at Virginia Tech.

Abstract

The research conducted represents an entirely new application of the self-consistent modeling strategy originally developed by Kröner to describe the elastic behavior of polycrystalline aggregates. The modeling is employed along with experiments to investigate the unique thermo-mechanical response of polycrystalline α-uranium. The orthorhombic crystal structure leads to high levels of anisotropy in its thermal, elastic and plastic response, as compared to cubic, or even hexagonal metals. Most interesting, the anisotropic thermal expansion response has one direction with a negative coefficient of thermal expansion, which in a polycrystal induces thermal residual stresses in polycrystals during cooling from thermo-mechanical processing temperatures. Unlike most metals, a fully annealed sample of α-uranium has strong thermal residual stresses. Furthermore, these thermal residual stresses are strong enough to induce plastic flow, which makes it unique compared to other metals which exhibit thermal stresses such as Zr alloys. During thermal cycling, the plastic strains accumulate and lead to a unique response of permanent shape change, termed thermal ratcheting. Textured polycrystalline α-uranium samples have a permanent shape change as a result of cooling and heating back to an initial temperature. This response has been well documented and qualitatively explained, but a complete explanation of the ratcheting response that incorporates all of the key factors, especially preferred orientation has been missing, until now.

To approximate the development of the thermal residual stress state and understand its effects on mechanical deformation, a combination of neutron diffraction experiments and self-consistent based polycrystalline plasticity modeling are employed. Initially, the thermal stresses were approximated assuming the stresses were relaxed by the known slip modes, predominately the chimney mode. This approach lead to quantitatively accurate estimates of the internal stresses. Subsequently, theses internal thermal stresses are shown to affect the deformation modes and internal strain evolution, but have little effect on the macroscopic stress-strain response. The same model and experimental techniques showed that the presence of hydrogen embrittles the material without affecting the mechanisms of plastic deformation which control macroscopic flow. Additionally, the model is used to explore the effects of temperature on the mechanical deformation up to 150 ^{o}C. It was seen that the elevated temperature shifted the thermal stress state, and provided an apparent increase in twin resistance.

Finally, as a capstone to the dissertation research, additional $in-situ$ neutron experiments conducted during thermal cycling and literature review suggested that essentially isotropic, rate sensitive plastic deformation occurrs during temperature cycling. A rate sensitive polycrystalline plasticity model was developed and used to predict thermal ratcheting including the important effect of crystallographic texture. The thermal ratcheting response is explained through mechanisms of creep deformation. Diffusional flow mechanisms explain the ratcheting, and the rate dependence and temperature sensitivity of the plastic deformation are revealed to be critical to predict thermal ratcheting.

Keywords: Polycrystalline Plasticity, α-uranium, Thermal Residual Stresses, Thermal Ratcheting, Mechanical Deformation

Contents

List of Figures

List of Tables

Chapter 1

Introduction: α-Uranium and Polycrystalline Plasticity

1.1 α-Uranium

Orthorhombic α-uranium exhibits high anisotropy in its elastic [3], thermal expansion [4, 5] and plastic response [6, 7]. Studies on single crystals have shown these properties are temperature dependent [2, 3, 5]. A complete set of single crystals stiffness properties have been reported in ref. [3] for temperatures ranging from 25 to 650 ^{o}C. In terms of elastic properties, the stiffnesses at room temperature are C_{11}= 215 GPa, C_{22}= 199 GPa, and C_{33}=267 GPa along the a, b and c directions, respectively [3]. At higher temperatures, the anisotropy decreases (C_{22}/C_{33} to 0.80 at 650 ^{o}C from 0.74 at room temperature). Of particular interest, for the current work, is the anisotropy of the thermal expansion properties. In the b direction, the coefficient of thermal expansion is negative or near zero, while both the a and c direction exhibit positive thermal expansion [4, 5].

Along with the noted thermo-elastic anisotropy, α-uranium crystals exhibit strong plastic anisotropy as a result of the active deformation mechanisms: 4 dislocation slip modes and 3

deformation twinning modes [6, 7]. The [100](010) mode, denoted *wall slip*, serves as the primary (i.e., the softest) slip mode at room temperature and has only one slip system [6, 7]. The [100](001) mode, denoted *floor*, acts as a secondary slip mode, which involves cross-slip of [100] dislocations from the wall mode, and also contains only one slip system. At temperatures closer to the α to β allotropic transformation, the floor mode becomes the primary slip mode [6, 7]. The $\frac{1}{2}\langle 1\bar{1}0\rangle\{110\}$ mode, denoted *chimney slip*, is comprised of two slip systems and exhibits a larger critical resolved shear stress (CRSS) than the aforementioned slip modes at all temperatures up to the phase transformation temperature [2]. Despite this fact, this hard mode has been observed, via slip trace analysis, in coarse-grained α-uranium at room temperature [7]. Finally, the $\frac{1}{2}\langle 1\bar{1}2\rangle\{021\}$ mode, denoted *roof slip*, has four slip systems and the largest CRSS among all the modes. Roof slip is usually observed only near the β transition temperature in single crystals [2], but has been considered in crystal plasticity modeling of low temperature deformation [1, 8] as it is necessary to close the single crystal yield surface [9]. A schematic showing the slip modes is shown in Figure 1.1.

Three twinning modes usually occur in addition to the four slip modes. The $\langle 3\bar{1}0\rangle\{\bar{1}30\}$ twin mode has two twin variants. It is the most widely observed twinning mode and is a compound twin with a shear of 0.299 [1, 6, 10]. The $\langle 3\bar{1}2\rangle\{172\}$ twinning mode has four twin variants and is a type II twin with a shear of 0.227 [1, 6, 11]. The $\langle 3\bar{7}2\rangle\{112\}$ has four twin variants and is a type I twin with a shear of 0.227. This twin is a conjugate twin of the $\langle 3\bar{1}2\rangle\{172\}$. In crystal plasticity modeling studies carried out on uranium, this twinning mode has not been included since its contribution cannot be discriminated from its reciprocal twin, and it is seen in smaller fractions and occurs under similar loading conditions [1, 6, 10]. Under high impact loading, another twinning mode, $\{176\}\langle 512\rangle$, has been observed [12].

Single crystal studies showed plastic deformation mechanisms all exhibit independent temperature dependencies, meaning each mode's strength varies independently. Temperature sensitivities for the four slip and the single $\{130\}$ twinning mode [2] have been measured on single
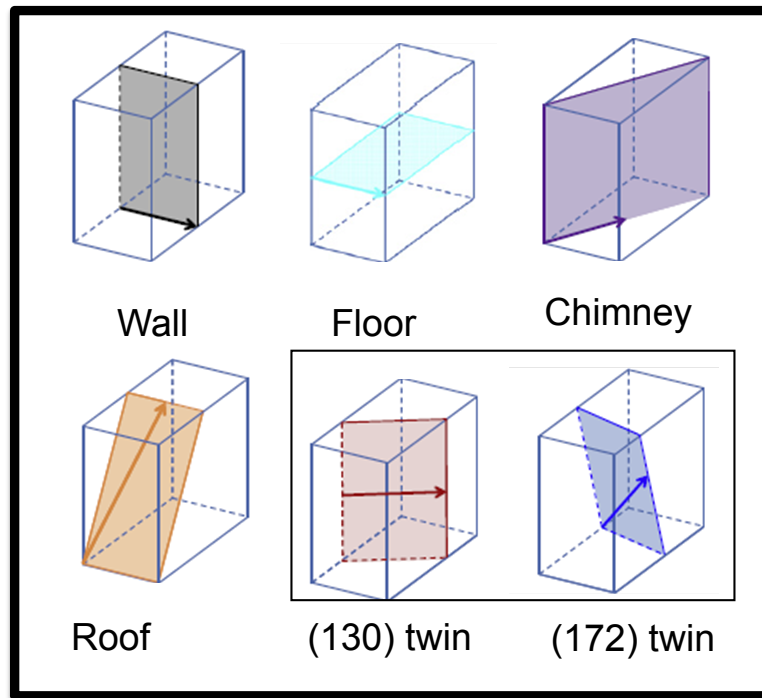
Figure 1.1: Schematic of the deformation systems in the crystal structure include the 4 dominant slip modes and 2 most predominant deformation modes (boxed), (drawings taken from [1])

crystals, and Figure 1.2 presents the results for the slip systems. As previously mentioned, the *wall* [100](010), mode is the softest, and room temperature, 23 ^{o}C, falls in the athermal plateau. However, room temperature lies within the thermally activated slip region for the other slip modes. In addition to the temperature dependence of slip, twinning also portrays a temperature dependence [2]. Unlike most metals, where deformation twinning resistance is thought to increase or remain invariant with temperature [13], the {130} twin softens with increasing temperature. Interestingly, it is does not portray "thermally activated" like behavior. Rather, it portrays an apparent linear dependence with temperature.

The temperature sensitivity and anisotropy of the plastic and thermal properties combine in polycrystals to create unique phenomena: strong plastic anisotropy, tension-compression asymmetry, and strong thermal residual stresses. Most interestingly, textured α-uranium is
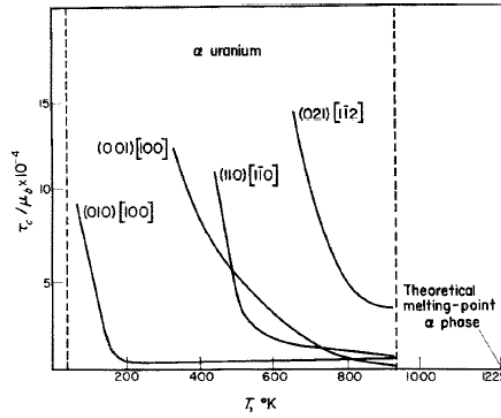
Figure 1.2: Plot of temperature dependence of the critical resolved shear stresses as function of temperature for the slip modes [2]

known to plastically deform when thermally cycled which will lengthen along some processing directions and shrink along others, which is termed thermal ratcheting [14, 15, 16, 17, 18]. For example, a piece of extruded bar of uranium will be longer after being heated (without inducing a phase transformation) and cooled back to its starting temperature, while the diameter of the bar will have decreased. This elongation will continue through continued thermal cycling.

The driving force for the ratcheting stems from the thermal expansion anisotropy. This anisotropy leads to a mismatch in the thermal strains between individual grains and the overall polycrystal which are accommodated initially by the development of elastic strains with a corresponding stress. These stresses increase to levels sufficient to induce plastic deformation. However, inducing plastic deformation alone is not sufficient to induce ratcheting. One clear example would be the case of a randomly textured polycrystal. The mismatch stresses would induce plastic deformation at the grain level, but would all average out to cause a net-zero plastic strain in a polycrystal. As such, crystallographic texture is another key ingredient in the ratcheting process. Thermal ratcheting has been studied in uranium a number of times, predominately in the 50's and 60's [14, 15, 16, 17, 18]. However, a complete explanation and associated physically based model of the phenomena has not been reported, until now.

1.2   Polycrystalline Plasticity

Polycrystalline plasticity models originally started with the Sach's model and were later extended by Taylor. What distinguishes these models from other traditional plasticity models (i.e. Von-Mises or J-2 based models) is the direct accounting for the distribution of crystallographic orientations within a polycrystal, which is commonly termed the 'texture' of the polycrystal, and the single crystal plastic response. In such an approach, a polycrystal is seen as the aggregate of individual crystals, often termed 'grains [1] ,' all possessing a unique orientation. Accounting for the single crystal response can be more computationally expensive, but incorporates the single crystal anisotropy, which becomes critical in certain circumstances, especially for lower symmetry metals. In FCC alloys, there is typically only 1 slip mode considered and for BCC materials, various authors will account for a variety of different slip modes. Magnesium and its alloys 3 slip modes and a deformation twinning mode are usually considered in this kind of modeling. In α-uranium, the 4 slip modes and two deformation twin modes previously discussed are considered.

The challenge within this class of models is the capturing of the distribution of stresses between grains. In the two extremes, one can assume that all of the grains are under the same applied stress and use this to compute the strain response, known as the Sach's model. Conversely, one can assume all of the grains undergo an identical strain state, and compute the stress response from there, this is known as the Taylor approximation. Self-consistent approaches offer an intermediate approximation. These models invoke micro-mechanics to account for localization for each grain. It is noted that other approaches exist to provide this intermediate approximation between the Sach's and Taylor model, but they are not invoked in this dissertation. A few examples are: Crystal Plasticity Finite Element approaches, Fast Fourier Transforms based method (VP-FFT), n-site, and relaxed constraints.

---

[1]A grain in the model represents the collection of grains with the same orientation in a real polycrystal, the grain to grain interaction and localization due to neighboring grains is inherently averaged in these models.

1.2.1   Self-Consistent Modeling

Visco-Plastic Self-Consistent (VPSC), Elasto-Plastic Self-Consistent (EPSC) and Elasto-Visco-Plastic Self-Consistent (EVPSC) are examples of self-consistent polycrystal plasticity modeling. Prior works have explained VPSC [19], EPSC [20], the modeling technique [21], and EVPSC [22] in great detail, so the current chapter aims to only provide necessary background information to understand how the approach will be employed. These models are distinguished by the assumptions regarding the single crystal constitutive response and homogenization/interaction scheme.

In these models, a polycrystal is modeled as a discretized set of grains. Each "grain" has a unique orientation (three Euler angles, per Bunge's convention) relative to the specimen coordinates, and an associated volume fraction. Each grain is assumed to be embedded in a homogenized effective medium (HEM), and load and/or deformation is applied. The behavior of the HEM is assumed to exhibit the volume weighted average behavior of each of the individual grains, but in general, this behavior is not known *a priori*. The polycrystal stiffness (that of the HEM) is solved iteratively through the self-consistent scheme originally presented by Hutchinson [23]. Such a scheme invokes the Eshelby solution, which allows for the computation of the stress state in each grain, if the stiffness of the HEM is known. The challenge becomes that the grain stiffness vary with local stress when a grain is plastic, so iterative steps need to be taken, but, the elastic stiffness does not change with stress. As such, the elastic case is much easier to solve.

To account for plasticity in each grain, a single crystal flow rule used for each grain and which will ultimately be used to modify the stiffness used in the self-consistent scheme is ascribed. The reader is reminded that thermo-elastic (lattice) strains always obey Hooke's law, $\sigma = C\epsilon_e$, but when plastic strains are present, Hooke's law alone is no longer sufficient. When the stress state reaches the boundary of the yield locus, the stress induces plastic in addition

to the thermo-elastic strains. For the EPSC modeling effort, the additive decomposition of the total strain is employed, $\boldsymbol{\varepsilon}_t = \boldsymbol{\varepsilon}_e + \boldsymbol{\varepsilon}_p + \alpha \Delta T$, which is appropriate for infinitesimal strain problems. In EVPSC modeling, an additive decomposition is employed as well [22], though the kinematics may be adapted to render the approach valid for finite strain problems. For a strain hardening material, the flow stresses increase with accumulated plastic strain. The rate of expansion of this surface is defined by the hardening rule, which relates the resistance to further plastic strain (i.e. the flow stress) to the accumulated plastic strain (or more rigorously, to the plastic 'state' of the material). This is often expressed in terms of dislocation densities [1, 8, 24, 25, 26]. In EPSC, this hardening plays a critical part of the iterative solution of the problem during each straining step, but in EVPSC and VPSC the hardening rule is handled separately as an update to the constitutive parameters at the end of each straining step.

Crystal plasticity allows for more physically-based plasticity rules then the J-2 continuum rules. Physically, dislocation glide and deformation twinning serve as the plastic deformation mechanisms for typical deformation and each produces a prescribed shear strain in a particular straining direction lying within a particular plane. For slip or twinning on the system α, the resulting plastic strain rate is $\boldsymbol{\epsilon}_p^\alpha = \mathbf{m}^\alpha \gamma^\alpha$, where $\mathbf{m}^\alpha$ is the Schmid tensor (the symmetric portion of the dyadic cross product of the shear direction b_α and the shear plane n_α). We assume that each slip and twinning mode has an associated Critical Resolved Shear Stress (CRSS or τ_{cr}^α) required to activate that slip system. In other words, the Schmid law is assumed. In a crystal plasticity context, the resolved shear stress on a slip system is directly computed, and relative activities of different slip modes are tracked. In EVPSC, the resolved shear stress is directly used to compute the shear rate through a viscoplastic law. In EPSC, the resolved shear stress is compared to the CRSS, and if they are considered close enough, the local stiffness is adjusted to account for plastic flow.

1.2.2 Experimental Techniques

A model alone, without experimental validation, is insufficient for a full understanding, so in this this dissertation, $in-situ$ neutron diffraction serves as the primary experimental method. Neutron diffraction experiments allow for the measurement of internal lattice strains as a function of stress and temperature in large polycrystal samples. This serves as an internal thermo-elastic strain gage that acts to average all of the grains which satisfy a given diffraction condition. This type of experiment provides an idea of the stress distribution between different sets of grains by providing a measure of the thermo-elastic strain within a grain set. Such an approach pairs well with the polycrystalline plasticity models to allow for direct comparison, and gain further insights. The polycrystalline plasticity models can compute volume-averaged thermo-elastic strains within the set of 'grains' that satisfy the diffraction conditions for direct comparison.

The current work utilized the Spectrometer for Materials Research at Temperature and Stress (SMARTS) in the Manuel Lujan, Jr. Neutron Scattering Center, at Los Alamos National Laboratory [27], and the VULCAN instrument at Oak Ridge National Laboratory (ORNL) [28]. In these spectrometers, specimens can undergo a combination of uni-axial tension/compression loadings and temperature changes while inside the neutron beam. A spallation source supplies packets of neutrons with a range of velocities (i.e. wavelengths). Knowing the distance between the chopper (time zero location) and the detector, along with the corresponding time of flight allows for the measurement of the speed, which is then turned into a wavelength via the de Broglie equation: $\lambda = \frac{ht}{mL}$, where h is Plank's constant, t is the time of flight, m is the mass of an electron, and L is the length of the flight path. From the wavelength, Bragg's law reveals the lattice- or d-spacing. The time of flight experiment allows for a fixed diffraction geometry (unlike in typical x-ray measurements or reactor sources of neutrons, where the diffraction angle 2θ is varied during an experiment). The positioning of the detectors puts the diffraction vectors

parallel and perpendicular to the loading direction in the case of uni-axial deformation experiments or in two orthogonal directions in temperature experiments, as illustrated in previous publications [27, 28].

Monitoring the change in lattice spacing for different *hkl* diffraction peaks as a function of macroscopically-applied stresses, strains, or temperature shifts provides insight into the active plastic deformation mechanisms. A strain is associated with each *hkl* diffraction peak and is computed using a standard engineering strain definition given by equation 1.1:

$$\varepsilon^{hkl} = \frac{d^{hkl} - d_o^{hkl}}{d_o^{hkl}} \tag{1.1}$$

where d^{hkl} is the lattice spacing at the current load increment, and d_o^{hkl} is the lattice spacing at zero macroscopic stress. Ideally, d_o^{hkl} would be the stress free lattice parameter, but since polycrystalline α-uranium material has strong residual stresse, the experimental setup is most accurate at measuring a relative change in lattice spacing. Using the initial value provides a relative change in lattice spacing during the deformation. The same protocol is employed in the polycrystalline plasticity models previously described, such that the comparison between model and experiment is consistent. It is noted that each *hkl* reflection corresponds to the measurement of all of the grains with the {hkl} planes perpendicular to the diffraction vector. As such, a set of grains {hkl} refers to all of the grains with a *hkl* plane perpendicular to the diffraction vector.

In an elastically isotropic material without residual stresses, the strength of each set of grains would be proportional to the amount of internal strain carried by that set of grains. Grains showing higher internal strain would be harder, since the stress in directly related to the strain (through Hooke's Law). However, elastic anisotropy and thermal residual stresses convolute direct interpretation of this data, so polycrystalline modeling is required to better interpret these experiments. Elastic anisotropy varies the resulting strains, as more compliant

grains carry more strain for a given stress. Residual stresses affect the d_o^{hkl} value, so that apparent strain reflects the average change in local stress rather then to absolute stress within a grain. Further details of the experimental setup are found in the literature [27, 28].

1.3   Broader Impacts

While α-uranium does not have widespread commercial use, it does make for a great material for academic study. Studying this material has provided insights and understanding of the development of thermal stresses that can be applied in other materials with anisotropy or heterogeneity in the thermal expansion coefficients. Insights gained here can directly be provided to any material with thermal residual stresses, and can indirectly be provided by growing the conceptual understanding of plastic deformation. One example direct extension would be to a material that exhibits thermal ratcheting developed by Monroe and co-workers [29]. They developed a technique to control the thermal expansion coefficients in martensitic wires by controlling the distribution of martensitic variants by imposing different strains (i.e. changing the texture with deformation). Their so-called 'Tailored thermal expansion alloys' exhibit a ratcheting response. It is suspected the same type of deformation mechanisms are at play in those alloys as in the pure α-uranium.

1.4   Overview of Dissertation

This dissertation has 6 chapters of original content that follow this initial introductory chapter. In the second chapter, the development of thermal residual stresses is investigated using a combination of neutron diffraction and EPSC modeling, and was published in *Scripta Materialia* [30]. In the third chapter, the effects of the thermal residual stresses on room temperature deformation are investigated by extending the EPSC model introduced in the second chapter and

using that model to interpret in-situ neutron diffraction experiments. This portion of the work was published in *Acta Materialia* [31]. In the fourth chapter, the effects of hydrogen on the deformation are examined using essentially the same approach as was employed in Chapter 3, together with tests to failure and fractography. This portion of the work was published in *Journal of Nuclear Materials* [32]. In the fifth chapter, the temperature dependent nature of compression along the rolling direction is studied using the model presented in Chapter 3 and accounting for the temperature dependence. This portion of the work is being submitted to *Materials Science and Engineering A*. In the sixth chapter, $in-situ$ thermal cycling experiments are presented, and potential mechanisms for thermal ratcheting are discussed. In the seventh chapter, a rate sensitive polycrystalline plasticity model, termed EiVPSC, is developed and used to predict thermal ratcheting. These two chapters will combine for one journal publication. The final chapter summarizes this work, and provides direction for future research.

1.5   Contributions of Co-authors

The work shown in chapters 2-7, could not have happened without the help of many collaborators. As such, it necessary to identify the contributions of the collaborators in each of the chapters to allow for the contributions of the primary author to be identified for the purposes of the dissertation committee.

This work was done with many co-authors, so I've tried to identify them in order of contribution:

- Sean Agnew- worked with as a significant contributor throughout all the research reported in this dissertation. Many discussions were conducted, so to ascribe this as solely my work would be dishonest. His contributions were much more significant in the earlier chapters, and by the later chapters played a less significant role. He always served

as a great resource to help answer any background research question and act as a guide through the vast literature on mechanical deformation.

- Elena Garlea- has worked with us all the way through this project. She supplied material for the work in chapters 3, 4 and 6. She conducted the experiments at Los Alamos prior to my arrival as The University of Virginia which served as the basis for the work presented in Chapter 5.

- Rupalee Mulay- was a post-doctoral fellow when I started at UVa, and helped get this project started. She taught me the basics of operating EPSC as well as gathered preliminary input files necessary to run the code. She also helped gather the literature on α-uranium deformation mechanisms (slip and twinning) as we got this project started.

- Thomas Sisneros- worked as an instrument scientist at the Lujan Neutron Scattering Center at Los Alamos National Lab. He helped get samples machined and tested at Los Alamos. He was intimately involved in all the experiments reported here that were conducted at Los Alamos. He also helped get the electron microscopy completed for the hydrogen embrittlement study.

- James Wollmershauser- spent a summer in Los Alamos and conducted the experiments presented in Chapter 2.

- Don Brown- worked with James to conduct the measurements reported in Chapter 2, and helped Elena complete the experiments reported in Chapter 5.

- Ke An- worked as an instrument scientist at Oak Ridge, and help conduct the ratcheting and annealing experiments reported in Chapter 6.

- Laurent Capolungo- worked hand in hand to help develop an EVPSC code (not contained here), as well as helped derive key parts of the EiVPSC model presented in Chapter 7.

Chapter 2

Thermal Residual Strains in Depleted α-U

C.A. Calhoun, J.A. Wollmershauser, D.W. Brown, R.P. Mulay, E. Garlea, and S.R. Agnew [1]

The anisotropy of the thermo-elastic-plastic response of the orthorhombic crystal structure of α-U leads to the generation of stresses and strains in polycrystalline forms during temperature changes, including the so-called thermal ratcheting phenomenon [14]. Ratcheting indicates that plastic relaxation mechanisms are activated during thermal cycling. The current fundamental research uses Elasto-Plastic Self-Consistent (EPSC) polycrystal modeling, similar to prior works [20] on Zircaloy, combined with the in situ neutron diffraction observations to help elucidate the deformation mechanisms activated during cooling.

Early studies on α-U single crystals identified four slip modes and three twin modes that activate during mechanical loading at room temperature [1, 2]. The [100](010), denoted wall slip, acts as the primary slip mode at room temperature [6, 7]. The [100](001) mode, denoted floor slip, behaves as a secondary slip mode [6, 7]. Both of these modes make up one slip system. The edge-chimney slip mode, $\frac{1}{2}\langle 1\bar{1}0\rangle\{110\}$, has 2 slip systems and a critical resolved shear stress (CRSS) much greater than that of the primary slip mode at room temperature.

However, researchers observed activation of this mode in coarse-grained α-U [2, 6]. Finally, the $\frac{1}{2}\langle1\bar{1}2\rangle\{021\}$ mode, commonly called roof slip, has 4 slip systems and also has a CRSS value greater than the wall mode at room temperature [2]. The three twinning modes commonly seen in α-U are $\langle3\bar{1}0\rangle\{\bar{1}30\}$, $\langle3\bar{1}2\rangle\{172\}$ and $\langle3\bar{7}2\rangle\{112\}$. The $\langle3\bar{1}0\rangle\{\bar{1}30\}$ mode has two variants and is a compound twin with a shear of 0.299. The $\langle3\bar{1}2\rangle\{172\}$ mode is a type I twin with four variants and a shear of 0.227 [1, 6, 10]. The type II $\langle3\bar{7}2\rangle\{112\}$ twin has four twin variants and a shear of 0.227 [1, 6]. Under certain loading conditions with large grain sizes, the $\{176\}\langle512\rangle$ twins can be also activated [12].

Recently, McCabe et al. [1] showed, through the use of electron back scatter diffraction (EBSD) and the ViscoPlastic Self-Consistent (VPSC) model, that the $\langle3\bar{1}0\rangle\{\bar{1}30\}$ twinning mode acts as the primary twinning mode during mechanical loading of a clock-rolled textured polycrystal. The work also concludes that the harder slip and twinning modes must activate in order to explain the mechanical response. In a follow-on study, Knezevic and co-workers [8] studied the mechanical loading and texture evolution in three different initial textures of α-U (clock-rolled, straight rolled and swaged). Cooling from 400 ^{o}C (the hot deformation process-ing temperature) was simulated in order to account for the presence of thermal residual stresses. However, plastic deformation during cooling was neglected. The researchers again predicted $\{130\}$ twinning occurred in certain directions of loading. It is noted that the VPSC model em-ployed in these previous studies neglects elastic contributions, so results cannot be compared with in-situ neutron diffraction measurements. Finally, in a study conducted around the same time, Brown and co-workers [33] used in-situ neutron diffraction measure measurements to show the internal strain evolution of textured α-U during mechanical loading at three different temperatures, 23 ^{o}C, 200 ^{o}C and 400 ^{o}C. The experiments showed evidence of a change in relaxation mechanism with changing temperature.

The two specimens used for the current study came from the same clock-rolled material, with grain size of 25 μm, as used in Ref. [33]. Both cylindrical specimens had a diameter of

6 mm and height of approximately 15 mm. The specimens were placed in the Spectrometer for Materials Research at Temperature and Stress (SMARTS) and heated to and held at 500 ^{o}C under stress-free (no external load) conditions to allow any residual stresses to relax. One specimen had its cylinder axis aligned with the rolling direction, denoted RD, and the other with the transverse direction, denoted TD. The RD specimen was oriented so one detector bank would correspond to a diffraction vector in the normal direction, and the other bank was oriented to have the diffraction vector in the transverse direction. The TD specimen was oriented to have diffraction vectors in the rolling and transverse directions. Then, the internal lattice spacings were measured, and the temperature was lowered to room temperature with interruptions every 25 ^{o}C for lattice measurements. As previously seen [14], ratcheting was observed in the specimens after testing. The TD and RD specimens had initial lengths of 14.96 and 14.95 mm, respectively. The final lengths were 14.98 and 15.00 mm.

To interpret the measured lattice spacings, we employ EPSC modeling, which provides insight into potentially active slip systems. Details of the EPSC model are found in the literature [20]. In such a model, a discretized version of the initial texture is provided by a finite number of grains each with a defined volume fraction and a unique crystallographic orientation relative to the processing directions. Each grain is assumed to act as an ellipsoidal inclusion inside an infinite matrix of "bulk" material with properties which represent the volume-averaged properties of all the individual grains. The current model assumes spherical inclusions, which is consistent with reported microstructures in similar plate material [1]. The stress/strain state of each grain is computed using the Eshelby solution for an anisotropic ellipsoidal inclusion embedded within a homogeneous, anisotropic medium. Potentially active slip systems are identified from the computed stress state and the generalized Schmid law. The stress evolution (strain hardening) is modeled for each individual slip system using a linear hardening law, which is used to compute an elasto-plastic stiffness tensor for each individual grain at each increment (in strain, stress and/or temperature). The elasto-plastic stiffness tensor for each grain is then

used to iteratively compute the global stiffness tensor using the self-consistent approach. The macroscopic stress/strain state is then computed by using the elasto-plastic stiffness tensor. We assume that the temperature dependence of the themo-elastic properties of individual grains is consistent with prior single crystal experiments [5]. Quadratic functional descriptions of the 9 unique components of the orthorhombic single crystal elastic stiffness tensor were determined. Similarly, quadratic functions were fit to previously reported single crystal thermal expansion properties shown in Fig. 2.1(a) [5]. The functional form of the thermo-elastic tensor component values, x, are described by eq. 2.1, and the corresponding coefficients a, b and c, are presented in Table 2.1.

$$x = aT^2 + bT + c \tag{2.1}$$

the corresponding coefficients a, b and c, are presented in Table 2.1.

Table 2.1: Coefficients describing the approximate temperature dependence of the thermo-elastic single crystal properties of α-U

	C_{11} (GPa)	C_{22} (GPa)	C_{33} (GPa)	C_{12} (GPa)	C_{13} (GPa)	C_{23} (GPa)	C_{44} (GPa)	C_{55} (GPa)	C_{66} (GPa)	α_1 (1/K)	α_2 (1/K)	α_3 (1/K)
a (1/K^2)	-8.2×10^{-5}	-4.4×10^{-5}	-4.4×10^{-5}	-2.9×10^{-5}	-3.1×10^{-5}	-1.5×10^{-5}	-2.5×10^{-5}	-9.4×10^{-5}	-4.5×10^{-5}	6.8×10^{-11}	-7.7×10^{-11}	4.7×10^{-11}
b (1/K)	3.6×10^{-2}	-1.7×10^{-2}	-7.8×10^{-2}	-1.0×10^{-2}	-1.3×10^{-2}	-4.1×10^{-2}	-5.1×10^{-2}	-7.3×10^{-2}	-8.1×10^{-3}	-1.6×10^{-8}	4.9×10^{-8}	-1.6×10^{-9}
c (n/a)	211	207	293	48	23	120	142	96	80	2.3×10^{-5}	-7.2×10^{-6}	1.5×10^{-5}

At each temperature increment (0.5 ^{o}C), the stiffness and thermal expansion properties are recomputed, and the adjusted elastic stiffness tensor for each of the grains are used to compute effective elasto-plastic stiffness tensor as previously described. The current EPSC frame work allowed for the prediction of the thermal expansion properties of the textured α-U with temperature. Figure 2.1 (a) shows the experimentally measured thermal expansion properties of single crystal and (b) the predicted thermal expansion properties of the textured polycrystal from the self-consistent method. Some anisotropy is preserved macroscopically, but is reduced

from single crystal observations. Similarly, the properties along each direction show less temperature dependence than the primary directions of the single crystal. The textured material shows positive thermal expansion values in all directions, whereas [010] in the grains shows a near zero or negative coefficient of thermal expansion for the relevant temperature range. It is noted that large temperature excursions would lead to the sorts of plastic relaxation events described in detail later in this paper.
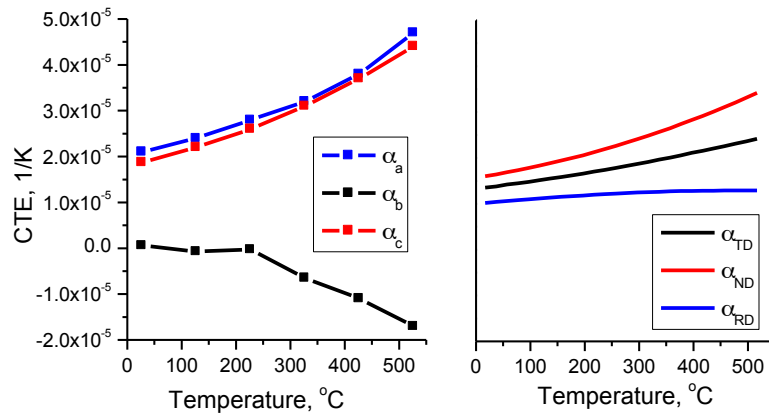
Figure 2.1: Single crystal thermal expansion properties (right) [12] and computed effective thermal expansion properties of textured polycrystalline (left) α-U

From Figure 2.1, it can be concluded that, during cooling, the large mismatch in thermal expansion properties (between individual grains and the surrounding aggregate) results in large compressive stress along the [010] direction in all grains. These stresses would be most prominent in grains with the [010] axis aligned with the normal direction (since it has the most positive aggregate CTE). Also, tensile stress would be expected to arise along [100] and [001] directions during cooling, because thermal expansion properties in both directions exceed those of any direction in the aggregate. Also, the internal strain rate (with temperature) diminishes as cooling continues (Figure 2.1), because the thermal expansion coefficients tend toward each other (i.e. toward isotropy) as temperature decreases, and the temperature sensitivity decreases. From the experimental neutron diffraction spectra, the lattice strains were computed based upon the change in the average lattice spacings for all grains oriented for

diffraction, according to Bragg's law, $d = \frac{n\lambda}{2\sin\theta}$, with the relaxed lattice spacings at 500 ^{o}C

taken as a reference, d_o. The total strain (mechanical and thermal) during cooling is given by:

$$\varepsilon_{total} = \frac{d - d_o}{d_o} \tag{2.2}$$

Thermal strains result purely from thermal expansion/contraction and occur independent of

boundary conditions. Subtracting thermal strains from total strain results in mechanical strain,

so mechanical strain, ε_{mech}, can be written as:

$$\varepsilon_{mech} = \varepsilon_{total} - \varepsilon_{thermal} = \varepsilon_{total} - \int \alpha(T)dT \tag{2.3}$$

Integration of the functional forms of the single crystal thermal expansion properties allows

for determination of the thermal strains.

Theoretical predictions of the mechanical strains were performed in which the grains were

assumed to be purely elastic. Figure 2.2 shows a comparison between the results of the purely

elastic prediction and the experimentally observed mechanical strain evolution from the two

different specimens. It is noted that two measurements were made of lattice strains in the TD

direction, and their evolution was consistent between experiments. The measured strains relax

during cooling, as they are much lower in magnitude than the thermo-elastic prediction. The

predicted elastic strains are of highest magnitude in [010] directions, normal to the measured

(020) plane spacing, independent of the grain orientation, but the experimental observations

indicate that internal strains in [001] are the greatest. As such, the [010] strains relax the

most, which highlights the anisotropy of the relaxation mechanism. This is one reason why we

focus on dislocation glide as a likely relaxation candidate, since other relaxation mechanisms

(e.g. diffusional mechanisms) are expected to be more isotropic even though the diffusivities

themselves have been reported to be anisotropic [34].

A Schmid tensor analysis reveals that the wall and floor, the two softest slip modes, cannot relax [010] stresses and strains. Recall that the Schmid tensor, $m = sym(\hat{b}x\hat{n})$, where $\hat{b}$ and $\hat{n}$ are the slip/twin direction and plane normal, respectively. Also, note that the {172} and {176} twinning modes can only minimally accommodate these stresses. Additionally, prior studies did not indicate a significant volume fraction of twins after cooling from processing temperatures in material with similar grain sizes [1, 33], but in material with much larger grain sizes, twinning was observed during cooling [6]. As such, only the roof and chimney modes can relax compressive [010] stresses that arise during cooling. Finally, the lack of relaxation in the strain within grains oriented for (002) diffraction (i.e. along the [001] direction) indicates the roof mode acts in an auxiliary role. Throughout the rest of the paper text, only the direction will be noted. The roof mode not only relaxes compressive stresses in [010], it also relaxes tensile stresses in [001]. However, Figure 2.2 shows the [001] strains directions are not relaxed to the same extent as the [100] strains. As such, the so-called base-chimney mode appears to be the primary relaxation mechanism.

In the EPSC modeling, the rank order of the CRSS values is consistent with prior experimental work [2], in which the wall and floor modes had the lowest CRSS, followed by the chimney, and roof had the highest, at 7, 10, 35 and 235 MPa, respectively. The model also included the {130}⟨310⟩ and {172}⟨312⟩ twinning modes, but the activation stresses were set sufficiently high to prevent activation at ~80 MPa and 140 MPa respectively. It is noted that the {112}⟨372⟩ and {172}⟨312⟩ activate under similar stress conditions, thus only the more frequently observed {172}⟨312⟩ mode was included. A small level of linear strain hardening, 10 MPa, of each deformation mode permitted numerical convergence. Such a low value is consistent with the activity of high temperature recovery processes.

Figure 2.3 shows that the model simulation results compare well with the experimentally observed strain evolutions. The model over-predicts the level of [010] compressive stresses, but qualitatively captures many trends. The [010] strains are highest when oriented with the RD, as
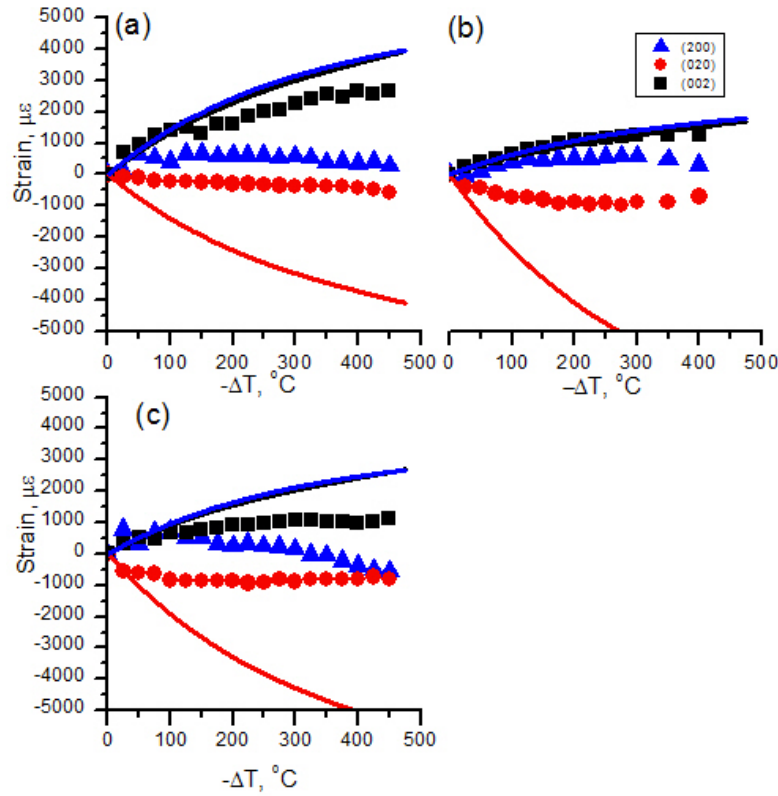
Figure 2.2: Plot of the internal mechanical strains (experimental data points and purely elastic model predictions) with change in temperature for grains from RD (a), ND (b) and TD (c) directions.

this is the direction in which there is the largest mismatch between the thermal expansion properties of the [001] crystallographic direction and the macroscopic properties. The model also predicts that the [100] strains start positive in the TD and ND directions and become compressive during cooling. The large [010] stresses activate the chimney mode alone which in-turn generates a compressive stress in the [001] direction. The [001] direction relaxes to a lower extent than the other crystallographic directions, again indicating minimal activity from the roof mode. Figure 2.3(d) shows that the chimney mode activates almost immediately upon cooling in the EPSC simulation, and stays active throughout cooling. It is also seen that the floor mode is the second most active slip mode during cooling, initiating slightly after the chimney mode whereas the roof and wall modes play only auxiliary roles. With the current parameter set, the

model predicts no activation of either of the two included twinning modes, which is consistent with experimental observations (no twins in material cooled from a processing temperature [1]).
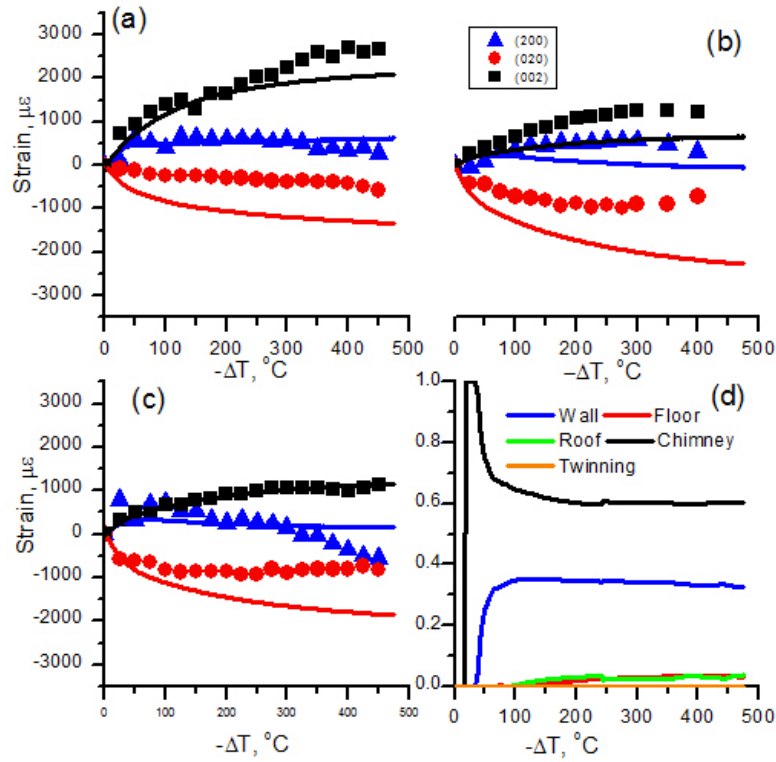
Figure 2.3: Plot of the internal mechanical strains (experimental data and model predictions) with slip modes activated, with change in temperature for grains from RD (a), ND (b) and TD (c) directions along with the activity plot (d) showing the relative activity of the 4 slip modes.

Assuming the CRSS values remain independent of temperature provided the best model of the experimental data despite the strong temperature variation in CRSS previously observed in single crystals [2] and polycrystals [35]. Simulations that incorporated the temperature dependence of CRSS under-predicted the level of observed relaxation. Such discrepancy between the single crystal experiments and polycrystal models, with regards to the CRSS ratios between hard and soft slip modes has been noted previously [36, 37]. Because the tests were conducted at relatively high homologous temperature ($\frac{T}{T_M}$ = 0.21 - 0.55) and took on the or-

der of 15 hours to complete, yielding an average cooling rate of 0.5 ^{o}C/minute, it remains likely that the temperature dependence of the CRSS was masked by the varying strain rate and possibility of diffusional flow. A prior study has shown creep to occur in randomly textured polycrystalline α-U [38] in a similar temperature range, for at least the start of the cooling, but the previous researchers could not identify the active creep mechanisms. As such, diffusional flow, diffusion-controlled dislocation climb and glide (power law) creep, and plasticity via dislocation glide are all potential relaxation mechanisms. Prior researchers have shown that the bulk diffusional flow is anisotropic [34], but in the current temperature range diffusion is most likely along high diffusivity paths such as dislocation cores and grain boundaries, which would not readily explain the anisotropy in the relaxation mechanism.

We also considered the possibility that power law creep through dislocation climb and glide could explain the relaxation. However, we cannot conceive of a means by which dislocation climb would provide an obvious explanation for relaxation (evidenced by no stress development) in both [010] and [100] but not [100] directions. A prior TEM study on an annealed thin film specimen observed a hexagonal array of pinned dislocations [39], which provided evidence of dislocation glide in the wall and chimney modes. The fact that the strains in the [100] direction reduce in magnitude and even switch sign in the transverse direction, provides additional evidence that glide along the chimney mode occurs rather than dislocation climb. Stress-free cooling of textured α-U specimens from 500 ^{o}C to room temperature with in-situ neutron diffraction measurements to monitor the internal strain evolution combined with EPSC modeling shows:

- The instantaneous thermal expansion coefficients for textured polycrystalline α-U as a function of temperature, based upon published single crystal elastic and thermal expansion data

- Mechanical strains develop in each grain due to the anisotropic interactions between

individual grains and the surrounding aggregate

- [001] strains relax minimally and nearly reflect the elastic solution, whereas [010] strains relax the most

- If dislocation glide is assumed to be the primary mechanism for relaxation, chimney slip, $\frac{1}{2}\langle 110 \rangle \{110\}$, acts as the primary relaxation mechanism during cooling of α-U

- Accounting for the temperature dependence of the CRSS values observed in single crystals was not required to most accurately model the current experimental data

Chapter 3

Investigation of the Effect of Thermal Residual Stresses on Deformation of α-Uranium through Neutron Diffraction Measurements and Crystal Plasticity Modeling

C.A. Calhoun, E. Garlea, R.P. Mulay, T. A. Sisneros, and S. R. Agnew [1]

3.1   Introduction

α-Uranium crystals exhibit strong anisotropy in their thermo-elastic and plastic response [2, 6, 10]. The thermo-elastic anisotropy leads to the generation of thermal residual stresses when

---

[1]Originally published in *Acta Materiallia*

polycrystalline uranium cools from processing temperatures [14, 30]. To the authors' knowledge, no efforts have been made to determine the quantitative effects of these thermal residual stresses on the constitutive response of α-uranium. However, they are held responsible for the unique phenomenon of thermal ratcheting, which is the progressive straining of textured α-uranium components that has been observed to occur during repeated thermal loading in the absence of any applied mechanical loads [14]. Along with the noted thermo-elastic anisotropy, α-uranium crystals exhibit strong plastic anisotropy, as a result of the active deformation mechanisms: 4 dislocation slip modes and 3 deformation twinning modes. The [100](010) mode, denoted wall slip, serves as the primary (i.e., the softest) slip mode at room temperature and has only one slip system [6, 7]. The [100](001) mode, denoted floor, acts as a secondary slip mode, which involves cross-slip of [100] dislocations, and also contains only one slip system. At temperatures closer to the α to β (orthorhombic to tetragonal) allotropic transformation, the floor mode becomes the primary slip mode [6, 7]. The $\frac{1}{2}\langle 1\bar{1}0\rangle\{110\}$ mode, denoted chimney slip, is comprised of two slip systems and it exhibits a larger critical resolved shear stress (CRSS) than the primary slip modes at all temperatures up to the phase transformation temperature [2]. This has been observed, via slip trace analysis, in coarse-grained α-uranium at room temperature [7]. Finally, the $\frac{1}{2}\langle 1\bar{1}2\rangle\{021\}$ mode, denoted roof slip, has four slip systems and the largest CRSS among all the modes, up to the transformation temperature of α-uranium. Roof slip is usually observed only near the β transition temperature in single crystals, but has been considered in crystal plasticity modeling of low temperature deformation [8] as it is necessary to close the single crystal yield surface [9]. The rational for including such a slip mode is the fact that compatibility requirements between neighboring grains in polycrystals can result in stresses of sufficient magnitude to nucleate slip, even on such hard secondary systems.

Three twinning modes usually occur in addition to the slip modes. The $\langle 3\bar{1}0\rangle\{\bar{1}30\}$ twin mode has two twin variants. It is the most widely observed twinning mode and is a compound twin with a shear of 0.299 [1, 6, 10]. The $\langle 3\bar{1}2\rangle\{172\}$ twinning mode has four twin variants

and is a type II twin with a shear of 0.227 [1, 6, 11]. The $\langle 3\bar{7}2 \rangle \{112\}$ has four twin variants and is a type I twin with a shear of 0.227. This twin is a conjugate twin of the $\langle 3\bar{1}2 \rangle \{172\}$. In crystal plasticity modeling studies carried out on uranium, this twinning mode has not been included since its contribution cannot be discriminated from its reciprocal twin, and it is seen in smaller fractions and occurs under similar loading conditions [1, 6]. Under high-impact loading, another twinning mode, $\{176\}\langle 512 \rangle$, has been observed [40].

Recent work on polycrystalline α-uranium by McCabe et al. [1] confirmed, through the use of Electron Backscatter Diffraction (EBSD) and the ViscoPlastic Self-Consistent (VPSC) polycrystal plasticity model, that the $\{130\}\langle 310 \rangle$ twinning mode acts as the primary twinning mode during mechanical loading during large strain deformations. In particular, the use of the VPSC model has shown that the polarity of this deformation twinning mechanism is the main source of the tension-compression strength asymmetry observed in wrought α-uranium [1, 8]. (By polarity it is meant, for instance, that the $\{130\}$ twin is activated by shear stress in the $\langle 310 \rangle$ direction, but not in the opposite $\langle \bar{3}\bar{1}0 \rangle$ direction.). VPSC modeling neglects elastic contributions which can comprise a significant fraction of the deformation at small strains. More recently, Knezevic et al. utilized the VPSC model in conjunction with finite element methods to predict the response in four-point bending [41]. The model was able to capture the texture evolution through the thickness and plastic deformation state of the beam after loading. Brown et al. [33] published in-situ neutron diffraction results of the internal strain evolution of textured α-uranium during mechanical loading. At room temperature, it was observed the internal strain evolution was not very sensitive to the loading direction during tensile loading between the rolling (RD) and transverse (TD) direction despite seeing anisotropy in the bulk response. Strong texture evolutions occurred during TD tensile loading at large plastic strains (20%), but not during RD tension experiments. Clocked rolled plate that underwent identical processing as in refs. [1, 33] was further thermally aged as part of a comprehensive study on internal hydrogen embrittlement corrosion conducted by the present authors, and subsequently

used for this paper.

The goal of the current paper is to compare model predictions with in-situ neutron diffraction experimental results, which critically depends upon accounting for elasticity, since the measured lattice strains are purely elastic (or thermo-elastic). The employed Elasto-Plastic Self-Consistent (EPSC) modeling scheme enables exploring an issue relevant to small strain behavior (e.g. yielding), which is frequently of interest for component applications, whereas VPSC modeling is often more relevant to metal forming. It is noted that a combined ElastoVis-coPlastic Self-Consistent (EVPSC) approach, which is valid at finite strains, has recently been introduced [22]. This will be an ideal approach for subsequent work, especially moderate temperature deformation, which will likely suffer more greatly from load relaxation. However, the focus on room temperature, small strain deformation of material with a pre-existing residual stress did not appear to require this more complex approach.

The authors reported, in a prior article [30], on thermal residual strain development in uranium during cooling through the use of polycrystalline plasticity modeling and in-situ neutron diffraction measurements. The internal lattice spacings were monitored during cooling from 550 ^{o}C, and lattice strains were then computed in a similar fashion to the current work. Comparison between known thermal expansion parameters and the measured changes showed mechanical strains developed during cooling. The EPSC code was used to model the thermal residual lattice strains along specific sample directions, and showed that plastic deformation must occur during cooling. These results enabled a reasonable estimate of the thermal residual stress (TRS) state within the grains after cooling, which is employed as an initial condition in the present study. Therefore, this article includes new in-situ neutron diffraction strain results on an aged α-uranium, and makes use of the EPSC model to account for the impact of TRSs on subsequent deformation. Implications for modeling the behavior of a wide variety of polycrystalline materials with non-cubic crystal structures or composites containing phases with distinct thermoelastic properties are also presented.

3.2 Experimental Method

Depleted uranium was initially cast into a 254 mm ingot. It was hot cross-rolled at 640 ^{o}C to a thickness of 32 mm, then warm clock-rolled at 330 ^{o}C to a thickness of 15 mm, before an intermediate anneal of 480 ^{o}C for two hours. Subsequently, the plate was further warm clock-rolled at 330 ^{o}C to a gage of 7.6 mm and given a final anneal of 550 ^{o}C for two hours. Bars (~114 mm long and ~11 mm in diameter) were cut from the rolled plate using electro-discharge machining (EDM). Each bar's length was considered such that it allows for a tension and compression specimen to be machined and was oriented along the final rolling direction (RD) or the in-plane direction transverse (TD) to it. Before machining into tension and compression specimens, each bar individually underwent an aging process that consisted of annealing at 630 ^{o}C for three hours in vacuum for hydrogen outgassing followed by water quenching. It is noted that this treatment was part of a broader study on hydrogen embrittlement, which will be reported in another publication. This processing left the material with a grain size of 25 μm measured by line intercept method in accordance with ASTM standard E112-96. The compression specimens were round cylinders with a diameter of 6.25 mm and a length of 15.75 mm, and oriented with the cylindrical axis along the RD or TD. The tension sample was a threaded round dog bone specimen with a gauge length ~28 mm and diameter of ~5 mm inside the gauge length and had the loading axis parallel to RD. Mechanical tests were conducted at room temperature to 9% macroscopic strain in compression and 5% in tension in position control to ensure there was not rupture for safety reasons. The texture of each sample was measured using the HIgh-Pressure-Preferred Orientation (HIPPO) instrument at Los Alamos National Laboratory [42] before and after mechanical deformation. The initial texture is a critical input for the modeling work and is shown in Figure 3.1. It is noted that the b-axes tend to align parallel to the rolling direction of the final pass and c-axes align in the normal direction. The additional aging process resulted in a slightly weaker texture than what

was previously reported on the starting plate [33], particularly the peak intensity of the {020} pole figure.
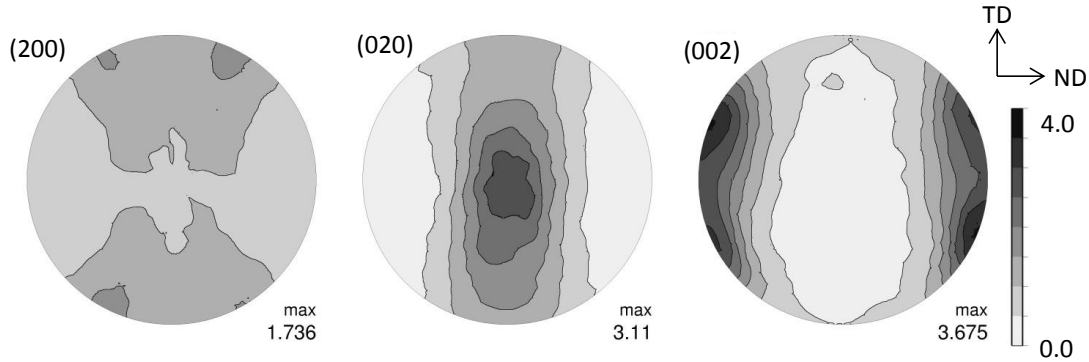
Figure 3.1: Texture measured on the RD compression sample prior to loading showing the final processing direction rolling (RD), transverse (TD), and normal (ND).

The Spectrometer for MAterials Research at Temperature and Stress (SMARTS) in the Manuel Lujan, Jr. Neutron Scattering Center, at Los Alamos National Laboratory [27] was employed for in situ monitoring of the internal strain evolution under uniaxial macroscopic deformation. The measurements were conducted in stress control in the elastic region, and in position control after the onset of plastic deformation to prevent creep. It is noted that stress relaxation still occurs during collection of diffraction spectra, which takes ~20 minutes per data point. The spallation source supplies packets of neutrons with a range of velocities (i.e. wavelengths). The beam size was 8 mm x 6 mm without any collimation. The positioning of the detectors puts the diffraction vectors parallel to the loading direction and perpendicular to it, as illustrated in previous publications [27]. However, only the strains along the loading direction are considered here, as they are the most sensitive to imposed deformation.

Monitoring the change in lattice spacing for different hkl diffraction peaks as a function of macroscopically applied stresses and strains provides insight into the plastic deformation mechanisms active. A strain is associated with each hkl diffraction peak and is computed

using:

$$\varepsilon^{hkl} = \frac{d^{hkl} - d_o^{hkl}}{d_0^{hkl}} \tag{3.1}$$

where d^{hkl} is the lattice spacing at the current load increment, and d_o^{hkl} is the lattice spacing at zero macroscopic stress. Ideally, d_o^{hkl} would be the stress free lattice parameter. However, this material has strong residual stresses and the experimental setup is most accurate at measuring a relative change in lattice spacing. Small shifts in specimen placement in the diffractometer can lead to shifts on the scale of the elastic strains in the peak positions [43]. As such, the initial value measured at 5 MPa load (the preload stress) was used as the initial lattice spacing. This approach is commonly accepted in materials with strong residual stresses [44]. The same protocol is employed in the simulation tool described below, such that the comparison between model and experiment is consistent. It is noted that each *hkl* diffraction peak corresponds to the measurement of all of the grains with the {*hkl*} planes perpendicular to the diffraction vector. As such, we refer to a set of grains {*hkl*} as all of the grains with a particular *hkl* plane perpendicular to the loading direction. The strength of each set of grains is related to the amount of internal strain carried by that set of grains. For example, grains that show higher internal strain are considered to be harder as the elastic stress directly relates to the internal strain state. Further details of the experimental setup are found in the literature [27, 45].

3.3   Modeling Approach

Previous studies have explained the EPSC algorithm [20] and the modeling technique [21] in great detail, hence only features developed specifically for the current work will be described. The polycrystal is modeled as a discretized set of grains. A "grain" in the EPSC modeling context represents the set of crystalline grains that share a specific orientation with respect to the polycrystal independent of its neighborhood. Each "grain" has a unique orientation (three

Euler angles, per Bunge's convention) relative to the specimen coordinates, and an associated volume fraction. Both are computed from the experimentally determined Orientation Distribution Function (ODF), which defines an intensity or volume fraction at each point in the three dimensional Euler angle space. This space is discretized to provide a finite set of grains for the computation. Here, 16,000 grains were employed in each of the simulation runs to describe the initial texture. Separate texture files were generated from the measured pole figures for each of the three different samples tested to accurately reflect the subtle changes in the texture between each sample.

Self-consistency simply means that the volume weighted average of the stress and strain within each grain equals the stress and strain levels of the aggregate, respectively. Each "grain" has the anisotropic thermo-elastic properties of the single crystal at room temperature. From there, each grain is assumed to be embedded in a homogenized effective medium (HEM), and load is applied through assumed boundary conditions. The behavior of the HEM is initially assumed to be the volume weighted average of each of the individual grains, but in general, this stiffness is not known. More specifically, the Hill approximation (the arithmetic average of the upper and lower bounds, Voigt and Ruess averages, respectively) is employed. The Eshelby solution allows for the computation of the stress state in each grain, if the stiffness of the HEM is known. The self-consistent iteration scheme developed by Hutchinson [23] is used to determine the stiffness of the HEM. From here, the loading (stress or strain) is into linear segments, each of which can have a different stiffness. After the first load increment, the HEM stiffness of the previous straining step provides an initial guess for the stiffness during the present step. For elastic loading, the stiffness will not change, but once plastic deformation begins, the effective stiffness of the flowing grains (and hence the medium as well) evolves during plastic deformation.

Notably, EPSC modeling does not account for nearest neighbor interactions that can affect the stress state within an individual grain. Rather, these interactions are assumed to average

out over the numerous grains with similar orientation within the polycrystals, each of which likely have a distinct neighborhood. Conveniently, such an assumption corresponds well with the neutron diffraction strain measurement technique, as the irradiated sample volume is large, and each diffraction peak represents unique subset of grains with a common crystallographic direction (i.e. have a specific crystallographic plane normal (hkl) parallel to the diffraction vector). Thus, the model outputs the average lattice (elastic) strain within all of the model grains with orientations that satisfy each diffraction condition of interest.

For slip and twinning systems α, the resulting plastic strain rate, $\dot{\varepsilon}_p^\alpha = m^\alpha : \dot{\gamma}^\alpha$, where m^α is the Schmid tensor (the symmetric portion of the dyadic cross product of the shear direction b^α and the shear plane n^α). It was assumed that each slip and twinning mode has an associated Critical Resolved Shear Stress (CRSS or τ_{cr}^α) required to activate that slip system, i.e., slip (or twinning) on system α will occur when the stress satisfies the following relation: $\tau_{cr}^\alpha = m^\alpha : \sigma$. The CRSSs of the slip and twinning modes define a single crystal yield surface for each grain. The yield surface is the locus of stress conditions which cause the material to yield, and it bounds the region in stress space within which Hooke's law, $\sigma = C\varepsilon$, fully describes the deformation. For the modeling effort, the additive decomposition of the total strain is employed, $\varepsilon = \varepsilon_e + \varepsilon_p + \alpha\Delta T$, which is appropriate for infinitesimal strain problems.

Satisfaction of the evolution law, $\dot{\tau}_{cr}^\alpha = m^\alpha \dot{\sigma}$, is also required throughout the straining increment (again, satisfactory for infinitesimal strain problems), since the CRSS value typically increases during the straining step due to strain hardening (or more rigorously, to the plastic 'state' of the material), which is often expressed in terms of dislocation densities [24]. During an infinitesimal straining step, an effective elasto-plastic stiffness may be defined which accounts for the combined effects of strain hardening and elasticity. The secant linearization procedure is employed as detailed in the original paper of Turner and Tomé [20].

Either the extended Voce (3 parameter) or linear hardening (1 parameter) empirical hardening rules are employed for each slip system. In the interest of limiting the number of fitting

parameters, a linear hardening rule was adopted if possible, because there are many independent deformation modes (4 slip and 2 twinning). The hardening rates of the reference stresses of each slip and twinning mode depend on the total accumulated plastic shear strain in the grain. The functional form of the hardening law is written as:

$$\tau_{ref}^{\alpha} = \tau_{o}^{\alpha} + (\tau_{1}^{\alpha} + \theta_{1}^{\alpha}\Gamma)(1 - \exp{-\frac{\theta_{o}^{\alpha}\Gamma}{\tau_{1}^{\alpha}}}) \tag{3.2}$$

where Γ is the total plastic strain, and θ_{1}^{α}, θ_{o}^{α}, τ_{1}^{α}, and τ_{o}^{α} are plastic hardening parameters. The actual resolved shear strength of the individual slip and twinning systems are governed by both self- and latent-hardening interactions introduced through a hardening matrix, which describes the amount of hardening of a single system per unit strain of another. Again, in order to keep the number of free parameters in this study to a minimum, all of the self and latent hardening coefficients were set equal to 1 and not adjusted. The focus of the present study was on determining the relative contributions of the individual slip and twinning modes during deformation as well as exploring the possible influence of pre-existing thermal residual stresses. For a dislocation density-based approach to modeling the strain hardening, the interested reader is referred to the work of McCabe et al. [1] and Knezevic et al. [8].

Typically, the EPSC scheme is relegated to small strain deformation [46] , where the crystallographic reorientation of the grains due to slip may be ignored. That is true in the employed modeling scheme as well. However, the level of texture evolution due to deformation twinning is shown to be significant [1], even for the relatively small strains of interest and, thus, cannot be ignored. EPSC has been adapted to account for twin reorientation [21] since twinning is more than just a polar slip mechanism. New 'child' grains are created once a critical stress level (the CRSS) for twinning is reached within the grain [21]. These 'children' represent the twins and have orientations that are dictated by twinning crystallography. Note that each

'parent' grain can have multiple twin 'children', one for each active twin variant. The volume fraction of the parent grain is transferred to the children while keeping the total volume fraction associated with the parent and child constant. The incremental increases in the twin volume fraction, δw^t, for each twin t and the decrease in the parent volume fraction, δw^{parent}, are given by:

$$\delta w^t = \frac{\delta \gamma}{s^t} \ \& \ \delta w^{parent} = -\Sigma_t \delta w_t \tag{3.3}$$

where is the shear increment contributed by the twin system t of the parent grain, and is the characteristic twin shear. These changes in volume fraction are imposed at the end of each strain increment. After being created, the twin is treated as a new independent grain and the only coupling between child and parent is through the above volume fraction transfer. It is noted that recently an even more physically-based model of twin growth that considers the stress state in the child and parent twin has been introduced [47], but this has not been employed currently.

An initial stress and strain state must be assigned to the newly formed twins. It was previously concluded that a finite initial volume fraction (FIF) of twin must form upon nucleation, since this would give rise to a relaxation within the newly formed twin, which had been revealed by previous in-situ diffraction measurements on Mg alloys [21, 48, 49]. The present results do not reveal a strong relaxation within the twins. Therefore, the 'continuity' assumptions for tractions and displacements across the twin boundary described are employed [21]. The accumulated plastic strain in the twin, Γ, is also assumed to be equal to that of the parent grain, 'parent, as dislocations present in the parent grain are likely to be inherited within the twin, though in some way 'transmuted' by the twinning event itself (e.g. [50]). This assumption sets the level of strain hardening within the twin at its formation. Since we potentially vary

the volume fractions of the grains and introduce new grains at the end of each step after self-consistent convergence is obtained, the overall stress and strain increments are recalculated.

Although EPSC was originally developed to account for the thermal residual stresses in Zircaloy [20], an additional step was required to account for the impact of such thermal residual stresses on subsequent deformation. Recently, the authors reported on the build-up of thermal residual strains during cooling of depleted α-uranium using in-situ neutron diffraction [30]. The EPSC simulation code enabled modeling of those residual strains and quantification of the thermal residual stresses. In the present study, the residual stresses were recomputed for the precise texture employed, following the same procedure reported previously [30]. This has three important implications: first, it means that each 'grain' starts with its own stress state prior to the onset of mechanical deformation. (Obviously, in order to satisfy self-consistency the volume weighted average of these stress states must equal zero, prior to any applied loading.) Second, it means that the computed lattice strains are relative to this pre-stressed starting configuration. Third, there are implications for the single crystal yield loci which require more detailed consideration. To further understand the stress development, we present a schematic evolution of the yield surface through each step of the loading (Figure 3.2). It was defined 630 ^{o}C (the aging temperature) as the stress free temperature represented by (a). At this temperature, the stress state for all grains is set to zero and, thus, lies within the yield surface. Upon cooling, thermal stresses arise inside the textured polycrystal due to the thermal expansion anisotropy, which is schematically shown for a specific grain in (b). Ultimately the stresses rise sufficiently to reach the yield surface, resulting in plastic flow (c) (previously shown in [30]). As implied earlier, the slip mechanisms in α-uranium are thermally activated [2], i.e. they become softer as the temperature increases. In a comprehensive model, this temperature dependence of the critical stresses and hardening rates would be incorporated directly. However, it was found that essentially perfectly plastic behavior with low (temperature independent) critical stresses best captured the residual strain development. We postulate that most

of the plastic relaxation, which occurs during cooling, does so at high temperatures where the mechanisms are athermal and where dynamic recovery (minimal strain hardening) is promoted. However, the CRSS values which well-describe the low strain rate plasticity during cooling are too soft to capture the subsequent finite strain rate deformation at ambient temperatures. As such, a new set of CRSS values are introduced to describe the ambient temperature deformation (d). To ensure all stress states stay within (or on) the yield surface, a comparison between the old (from cooling) yield surface and the new desired ambient temperature yield surface is performed. The higher CRSS values are retained for further calculations. As will be seen later, this precaution did not result in any changes in the CRSS values in the current study. However, any time the CRSS values are changed between processes (e.g. stress-free cooling, followed by deformation) it is important to make this verification. Additionally, the overall plastic strain is reset to zero, which simplifies the subsequent strain hardening parameterization and implicitly assumes no anisotropic strain hardening is induced by cooling. The above procedure allows modeling the asymmetry from the residual stresses by biasing the proximity of the stress state with respect to facets on the yield surface which are associated with different deformation modes. After the yield surface is expanded, mechanical deformation occurs (e), which ultimately leads to the yielding at a point different than what would be predicted without the thermal residual stresses (f). In sub-figure (e), it becomes clear that the stress state lies closer to the yield surface in one direction than in others. Within a single slip system (two parallel lines), we see how an asymmetry can arise in the yield behavior, as forward slip is more easily activated than the opposite mode. This would not happen in the absence of thermal residual stresses.
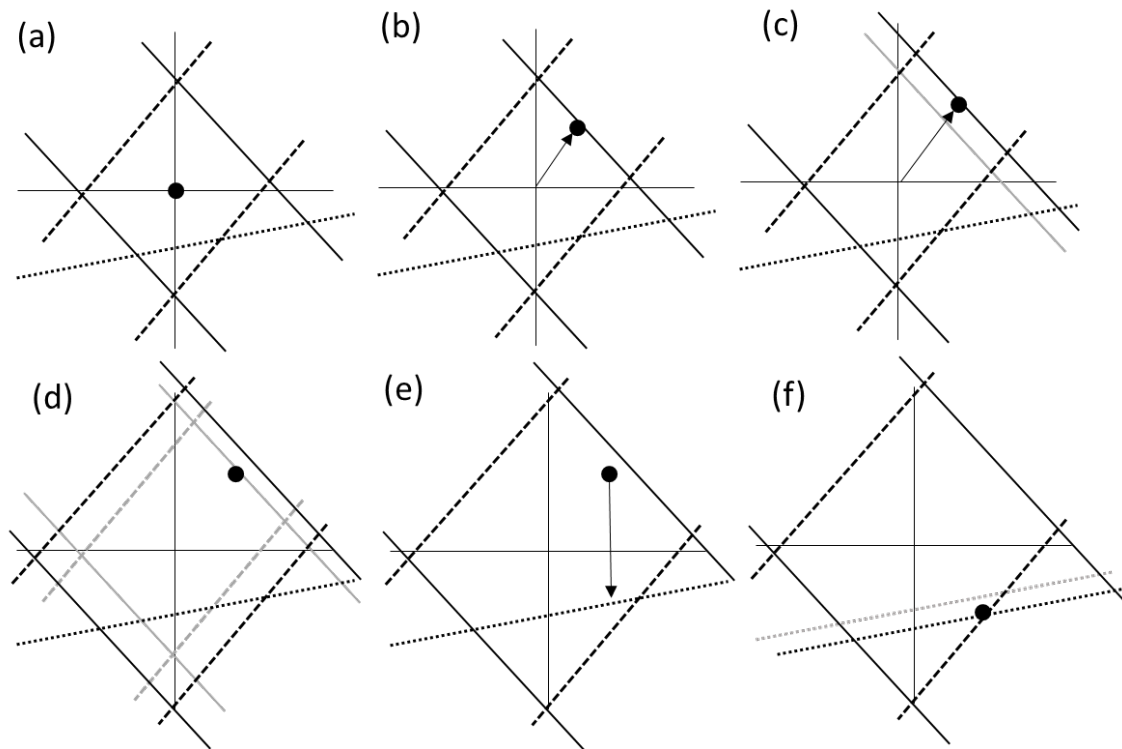
Figure 3.2: Schematic showing the evolution of the yield surface within a single "grain" during stages of cooling and subsequent deformation, where pairs of solid and dashed lines denote forward and backward shear directions for slip and the single dotted line denotes the forward direction for twinning. Figure (a) shows the completely relaxed condition assumed to be 630 ^{o}C, (b) stresses arise from the anisotropy in thermal expansion, (c) yielding caused by the thermal stresses, (d) expansion of the yield surface after cooling is completed, (e) stresses applied through mechanical deformation, and (f) yielding that occurs during room temperature deformation.

3.4   In-situ Experimental Observations

In-situ neutron diffraction data collected during tension and compression deformation along RD and compression in TD on aged polycrystalline uranium are presented. Figure 3.3 shows data collected during compressive loading along RD and TD. Sub-figures (a) and (d) show the macroscopic stress-stress response for the RD and TD respectively. Sub-figures (b) and (e) show the internal strain evolution for seven different families of grains oriented with the labeled lattice plane normal parallel to the loading direction. It is seen that the {021} grains are the softest, and {002} grains are the hardest in loading along both directions. It is also seen the rank order of strength is maintained between the RD and TD loading, but some changes are observed. In particular, there is more spread between the {131} and {021} grains in TD then in the RD, and the converse is true between the {112} and {200} grains. Sub-figures (c) and (f) show the normalized intensity shift with variation in applied macroscopic stress. The intensity for a given {hkl} at each loading point is normalized by the first measured intensity at ~5 MPa. The strong shift in intensity indicates twinning occurs during loading, especially in the case of RD compression, (c). In particular, it shows the {040}, {021}, and {131} grain sets lose volume fraction (intensity scales linearly with volume fraction) and the {200}, {112}, {002} and {111} gain volume fraction when compressed along RD and TD. It is noted there is a stronger shift in intensity in the {200} peak intensity during RD compression then during TD compression. From these data, the specific reorientation changes cannot be concluded (i.e. {002} grains shift into the {200}). However, it can be discerned that the onset of twinning occurs at a somewhat lower macroscopic stress, in RD, around -300 MPa, than along TD, around -400 MPa. Interestingly, an apparent 'yield' in the {200} grains occurs simultaneously with the drastic intensity shift. The original {200} grains may not actually yield (as suggested by the shift) in either loading condition. Rather, the additional volume fraction transferred into that orientation (by twinning) is at a lower stress state than the grains, which originally have that

orientation. The measured {200} strain represents the volume average of the strains in these two subsets of {200} oriented grains (original and mechanical twins). The significant occurrence of twinning observed during RD compression is also evidenced by the experimentally measured texture evolution after the straining experiment, which is discussed later in the paper. Experimental observations for tensile loading along the plate rolling (RD) α-U have already been published [33], so for brevity they are not included separately here, but are compared with the model in the next section.
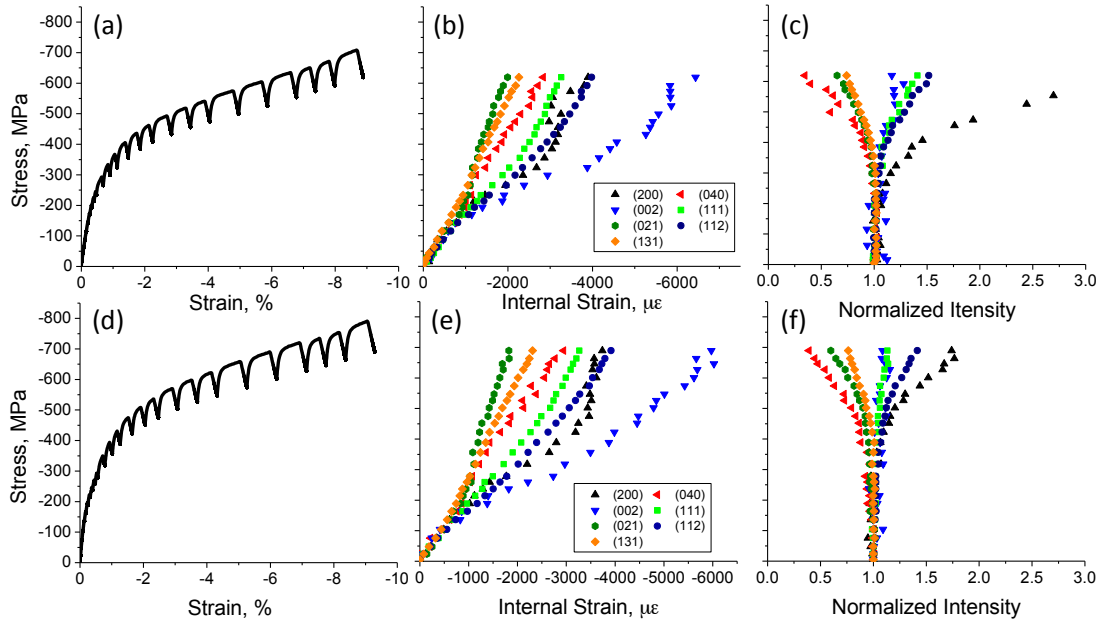
Figure 3.3: Experimental results from compression loading along the (a-c) rolling and (d-f) transverse directions showing the macroscopic stress-strain curves (a & d), internal strain evolution (b & e), and normalized intensity shifts (c & f).

After comparing the tension and compression data along the rolling direction, a tension-compression asymmetry can be observed, as previously reported [35]. Figure 3.4 shows the macroscopic stress-strain curves for loading along the rolling direction. The serrations in the measured stress-strain curves originate from relaxation during the constant position holds to collect the neutron diffraction data. Note the asymmetry in the observed micro-yield, the bulk

flow stress, and the strain-hardening behavior on the measured curves. Two mechanisms are likely to be responsible for this asymmetry: (1) the polar nature of twinning that is known to be active in this material and (2) the thermal residual stresses. Experimental in-situ diffraction results provide insight into the activation of twinning, and EPSC modeling will be used to investigate the effects of the residual stresses. From the changes in intensity shown in Figure 3.3, it is clear that twinning occurs in compression. However, there is not a clear change in peak intensity at the observed micro-yield in tension, which were not included for brevity. As such, it is clear that twinning plays a role in creating the asymmetry, as previously suggested by VPSC modeling [1]. The role of thermal residual stresses is further addressed in the discussion.
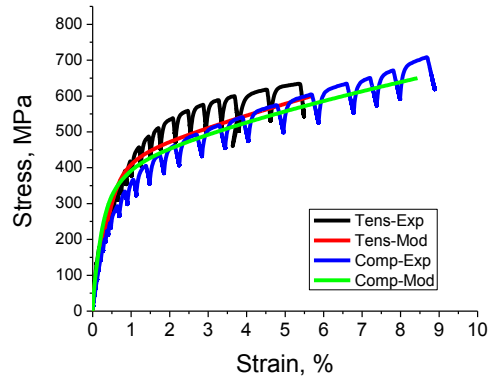
Figure 3.4: Stress-strain curves taken from RD tension and compression showing the observed tension-compression asymmetry. Predicted asymmetry from the EPSC modeling in compression and tension loading along the rolling direction.

3.5 Insights Gleaned from Modeling

EPSC modeling permits additional mechanistic insights to be obtained. The modeling results from the prior study [30] were further analyzed to provide insight into the stress state prior to loading. EPSC modeling was used to identify the relative strength and activity of the different known deformation mechanisms discussed earlier. In order to calibrate the model, some of

the experimental data had to be used for fitting. Specifically, the RD tension and compression experiments were used for model parameter selection and the TD compression experiment was used for model validation.

3.5.1   Thermal Residual Stresses

The prior simulation computed the stress state in each of the individual grains after cooling. When cast in sample coordinates, the volume weighted average stress obviously equals zero for this unconstrained cooling experiment. However, a volume weighted average of the stress state in each of the grains with respect to their crystal coordinates results in the following:

$$
\begin{pmatrix}
9.5 \pm 21 & 0 & 5.7 \pm 8 \\
- & -79 \pm 21 & -4 \pm 45 \\
- & - & 68.7 \pm 34
\end{pmatrix}
\tag{3.4}
$$

The thermal anisotropy (distinct from cubic metals) and elastic anisotropy are responsible for the non-zero deviatoric stresses. From the residual stress state, the volumetric average resolved shear stress (RSS) on each of the deformation modes were computed through employing the Schmidt tensor defined for each system (Table 3.1). The roof and chimney slip and {130} twin modes had nearly uniform RSS values across all of the variants. However, the {172} twin has a RSS of 20 MPa on two of the variants and -20 MPa on the other two variants. The maximum and minimum RSS are also presented to give the reader a sense of the variation in RSS that will become critical in predicting the resolved shear stresses.

Table 3.1: Volume average resolved shear stresses (in MPa) on different slip/twin systems computed from the average thermal residual stress inside a grain.

Mode	Wall	Floor	Roof	Chimney	{130}	{172}
Average	0	0	34	57	-25.5	±20
Maximum	2	2	125	144	-10	55
Minimum	0	0	0	23	65	-82

3.5.2 Mechanical deformation

The model parameters (CRSS and hardening parameters) were determined by fitting simulation results to the experimental data through an iterative process to create the best fit (qualitatively) for the macroscopic stress-strain data, the internal strain evolution, the texture evolution and the twin volume fraction. (The latter was reported by McCabe and co-workers using electron backscattered diffraction measurements (EBSD) for the same material with different processing conditions [1].) Table 3.2 shows the complete set of plastic parameters used for all simulations shown in this paper.

Table 3.2: Best-fit Voce hardening parameters for the 6 deformation mechanisms under consideration.

Mode	τ_o	τ_1	θ_o	θ_1
Floor	15	0	50	50
Wall	90	0	50	50
Roof	220	225	600	300
Chimney	175	150	400	100
{130}	90	0	5	5
{172}	325	0	125	125

Rolling Direction (model parameterization)

EPSC modeling showed the importance of the incorporation of thermal residual stresses for predicting the mechanical deformation. Figure 3.5 shows a comparison of the experimental

data and EPSC modeling results in which the thermal residual stresses were neglected (a-c) and incorporated (d-f) for a RD tension experiment. It is noted that only a few hkls are included to show internal strain for clarity. However, all of the hkls in Figure 3.3 were included in model calibration. Aside from a distinct microyielding behavior, the macroscopic flow curves do not have strong dependence on the residual stress state, but the internal strain evolution does. Sub-figures (b) and (e) show a change in rank order of the internal strain carried by the set of grains (hkls). For example, without the residual stress, the EPSC model predicts the {111} grains to sustain similar internal strain as the {131} grains, but the experiments show the {111} grains carry less internal stress. Similarly, neglecting the thermal residual stresses causes the model to predict drastically different yield behavior in the internal strains. However, this effect averages out to create the macroscopic flow curve in either case. The level of the internal strains within {200} grains is not well captured, but these grains only comprise a small volume fraction along the rolling direction, as seen by the low intensity at the center of the {200} pole figure in Figure 3.1.

Incorporating the residual stress corrects the error in predicted rank order in the level of internal strain within the various *hkl* grain sets. It is noted that the strength of the grain is not changed in an absolute sense (i.e. the yield surface, based upon crystallography and the data in Table 2, is identical in both simulations). However, the residual stress acts as a bias, moving the stress state away from one side of the yield surface and toward the other. In some grains, this leads to earlier than normally expected yield and in others it leads to delayed yielding. Figure 3.5 also shows an improved fitting of the internal strains; not only is the rank order correct, but the predictions also quantitatively match the observed to within $600\,\mu\varepsilon$, except in the case of the {020} grains, which are under predicted with or without the thermal residual stresses. Because incorporation of the residual stress state improved the model results, it has been used a 'worst case scenario' condition defined as the maximum possible residual stress state, consisting of cooling without any plastic relaxation. The model still under-predicted the internal strain level
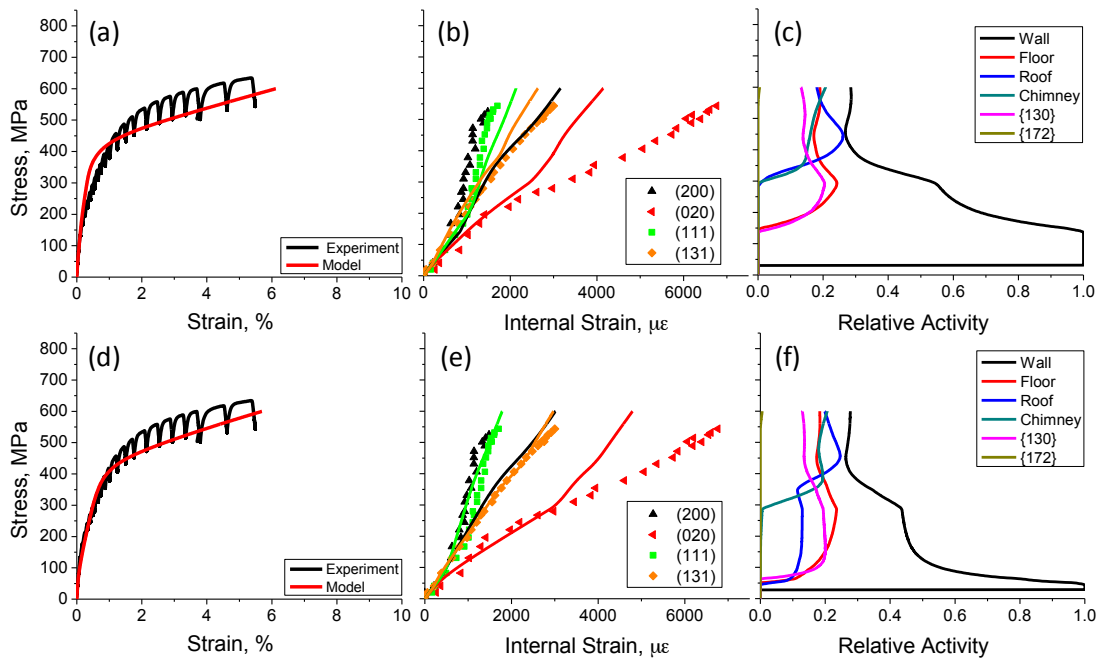
Figure 3.5: Experimental and EPSC modeling results from RD tension loading showing the macroscopic stress-strain response (a & d), the internal strain evolution (b&c), and activities of the different deformation mechanisms (c & f). Simulations neglected (a-c) and incorporated (d-e) thermal residual stresses.

in the {002} grains. The grains with their crystallographic *c*-direction oriented along the loading direction do not appear to significantly yield, based upon the internal strain data, but the EPSC model requires plastic deformation of these grains for macroscopic flow. This result suggests that the present grain interaction scheme employed may be too compliant, even though the secant linearization employed is the stiffest commonly used within self-consistent modeling. (See Wang et al. [51] for a recent discussion of the impact of linearization scheme on self-consistent predictions.) Simulations performed with more compliant linearization schemes departed even more strongly from experimental data. Another possibility is that the elastic stiffness matrix employed is not quite correct. For example, employing a C_{33} value reduced by 10% from the accepted value in the literature did result in somewhat better agreement for the predicted and experimentally measured internal strains in {002} oriented grains. However, there is no reason to expect that the elastic properties of the present uranium plate material would be suppressed, especially since the experimental data was of such high fidelity (claimed uncertainties of less than one half percent [3].)

Figure 3.6 shows the EPSC modeling results compared with the experimental data collected during compression loading along the rolling direction. Again, simulations are shown that neglected (a-c) and included (d-f) thermal residual stresses, respectively. Without TRSs, the {020} and {002} oriented grains exhibit nearly equal internal stress level, which does not match the experiment, but including the TRSs rectified the discrepancy. The {131} and {111} grains are not as strongly affected by the TRSs, but the model agreement still improves with their inclusion. It is also noted that in both the tension and compression cases the rank order of the plastic deformation mechanism activity plots varies drastically when incorporating the thermal residual stresses, but the macroscopic stress-strains curves do not.
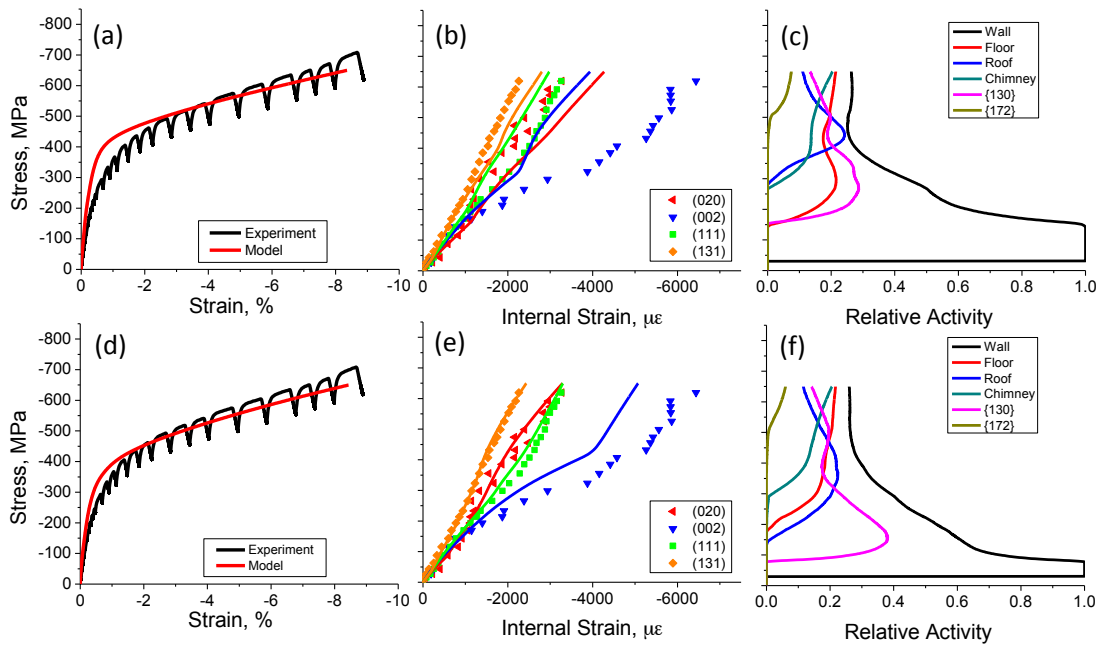
Figure 3.6: Experimental and EPSC modeling results from RD compression loading show-ing the macroscopic stress-strain response (a & d), the internal strain evolution (b & e), and activities of the different deformation mechanisms (c & f). Simulations neglected (a-c) and incorporated (d-e) thermal residual stresses.

Measurements and predictions of crystallographic texture evolution

Figure 3.7 shows a comparison of the measured (top) and predicted (bottom) post deformation textures from the RD compression experiment. Qualitatively, these two textures match. Notably the 200 pole figure shows an increase in intensity along the loading (RD) direction after deformation, and the intensity in the RD for the {020} pole figure spreads out from the center. Prior experimental work showed tensile loading to 5% total strain does not induce strong texture changes [33]. The EPSC modeling also showed little texture evolution during the tension experiment, consistent with the low level of twinning predicted (Figure 3.5(f)).
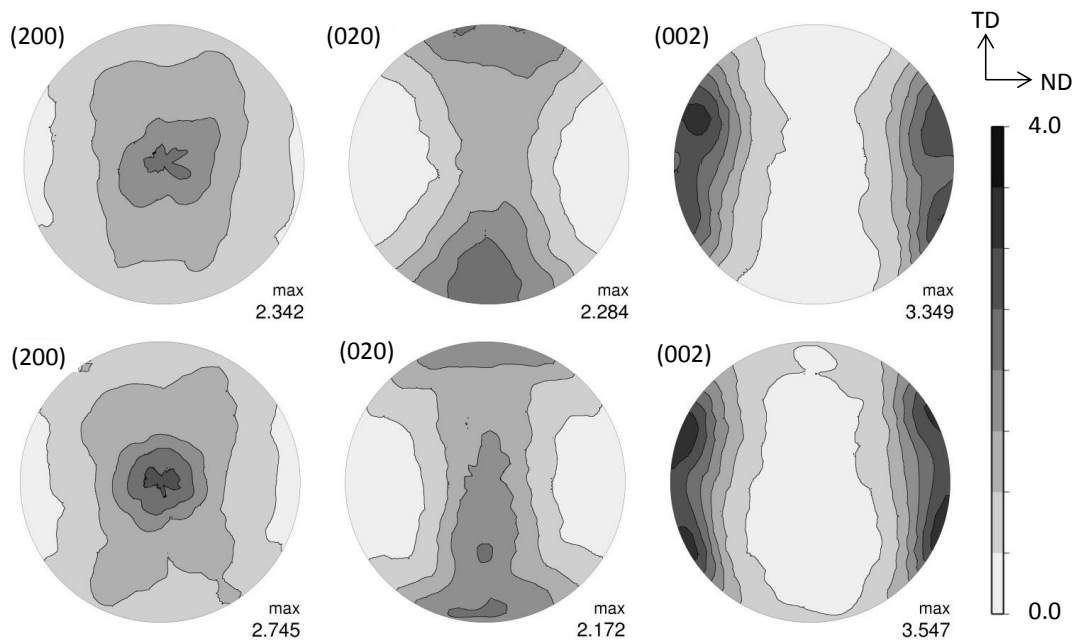
Figure 3.7: Post deformation textures from the RD compression test after 8.5% strain showing the measurements (top) and predicted from EPSC (bottom).

Transverse Direction (Model validation)

Using the model parameters determined from the RD loading and incorporating the thermal residual stresses, a simulation of the TD compression experiment was performed. Figure 3.8

shows that the model well predicts the macroscopic flow curve. In addition, the predicted internal strains all match well except for the strains in the {200} and {002} grains. In both cases, the inflection occurs prematurely, but both qualitatively follow the experimental trends. The accuracy in prediction of the internal strain evolution for a loading direction not used for model calibration provides increases confidence in the model. The error in the {002} grains seen in the RD tension (Figure 3.8(e)) loading is not as drastic along the TD compression, as the model well captures this grain set, and has near perfect rank order between the strength of the grains.
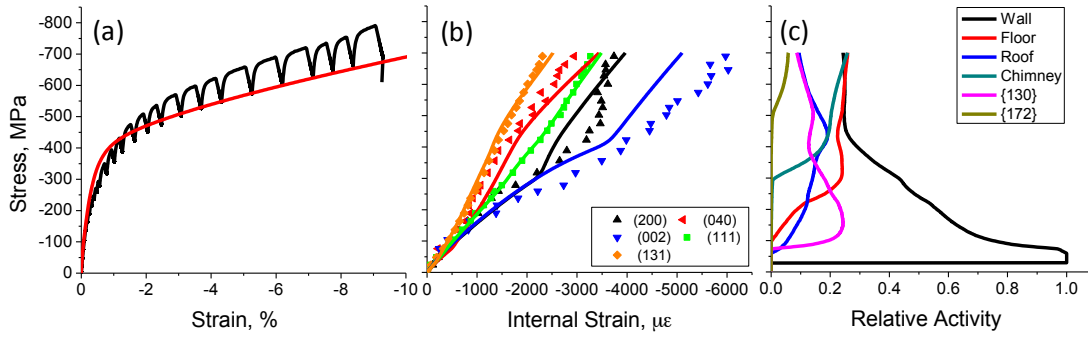
Figure 3.8: Experimental and EPSC modeling results from TD Compression loading showing (a) the macroscopic stress-strain response , (b) the internal strain evolution , and (c) activities of the different deformation mechanisms . Simulations incorporated thermal residual stresses, and used parameters fit from the RD loading (tension and compression).

3.6   Discussion

During parameter selection, the previously reported rank order of the strengths between the modes was maintained (i.e. roof remained the hardest mode, and wall the softest) [6]. Activation of wall slip had little effect on either the predicted bulk flow or the internal strains. Thus, it was maintained at a soft level consistent with aggregate microyielding and internal strain evolutions. In RD tension, the {130} twinning, roof, and floor modes all yield at nearly the

same point (100 MPa) (Figure 3.8(f)). The simultaneous activation allowed for the capturing of the yielding observed in the {111} and {112} (not shown) oriented grains, and maintained their rank order in internal stress during tension. The {002} grains are still carrying significant elastic load. It was observed that twinning or a combination of roof and floor would allow for capturing of the microyield observed in the {111} and {112} grains. Under all loading conditions, it was discovered that activation of the roof, floor, chimney and wall modes were all necessary to induce bulk flow for both the tension and compression cases. As such, the strength of the roof mode was chosen to provide a compromise for the flow point for the tension and compression bulk curves. The roof mode served as the controlling factor in tension, but due to the higher level of twinning during compression, it is not the limiting factor in that case. In compression, the model predicts that the floor and chimney modes control the onset of bulk flow. The floor mode was set at a high enough level to capture the yield in tension. If this CRSS was any lower, the yield in tension would be predicted to occur sooner in the {111} grains than what is measured. Increasing it any higher causes the flow stress in compression to be further over predicted.

The twin strengths were determined by computing the predicted twin volume fraction and comparing with literature. The model simulations resulted in 16 vol% in compression and 7 vol% in tension along RD. This agrees well with McCabe et al. which reports roughly 12 vol% of {130} twins formed during compression to a strain level of 10%, and roughly 5 vol% formed at a tensile strain of 5% along the RD [33]. In particular, activation of {130} twinning during compression prevented the 002 grains from carrying much elastic load, noted by the much lower internal strains in compression than in tension. The predicted internal strain values match well with the experimental values for these grains. Although only a small volume fraction was observed, the parameters controlling {172} twinning were employed to match the tension/compression asymmetry in strain hardening.

The hardening parameters were determined by comparing the macroscopic stress-strain

curves. The roof and chimney modes control the hardening during bulk flow, so the linear hardening terms were fit to capture bulk flow in tension and compression. The Voce terms were fit to capture the elasto-plastic transition. Without the Voce parameters, i.e. with only linear hardening, the transition was too abrupt. Additionally, it was seen that twinning modes required hardening, because the flow curve was too soft otherwise. The hardening of the floor mode was determined by looking at the bulk flow curve in tension at the micro-yield.

It is admitted that, while the asymmetry does increase marginally with the incorporation of the thermal residual stress, the complete asymmetry is still not captured with the current model. Figure 3.4 shows the model predictions of the macroscopic stress strain response that accounts for TRS. It is believed that the majority of the asymmetry arises from the polar nature of twinning rather than the biasing imposed by the thermal residual stresses, since accounting for them does not properly capture the observed behavior. Further work is necessary to better understand such a shortcoming, and the twinning-detwinning model of Wang et al. [47] may provide a better description. Trial simulations that neglected the effects of twin reorientation resulted in a higher level of asymmetry. However, the level of twinning predicted in these cases far exceeded that observed experimentally for both tension and compression.

It is encouraging that the model well-described the bulk elasto-plastic response (macroscopic and grain-level internal strains) along the transverse processing directions, despite the fact the model parameters were determined purely from the rolling direction tension and compression experiments. This creates confidence that (1) the predicted thermal residual stresses are accurately estimated and (2) the relative strengths of the different slip and twinning systems are correct.

3.7 Conclusions

In-situ deformation experiments were performed along RD in tension and compression and TD in compression, and the results complement prior in-situ tensile test results along RD presented in ref. [33]. From these experimental observations, the following conclusions are drawn:

- In-situ neutron diffraction intensity data confirms that twinning occurs much more in compression than in tension along the RD.

- Neutron diffraction confirmed yielding during RD compression is caused by twinning and slip, as the diffracted intensities of some of the yielding grains decrease during deformation (indicative of reorientation due to twinning) while other grains are well-oriented for soft slip modes.

Using this new and complete data set, EPSC modeling was employed to gain further insights. Simulating the macro stress-strain curves is easily done, given the large number of fitting parameter, however, predicting the internal strain is more demanding. The model which was calibrated using data collected during tension and compression experiments along the rolling direction, and validated using compression test data collected along the transverse direction lead to the following conclusions:

- Thermal residual stresses cause a biasing toward certain slip/twin variants, and are necessary to model the internal strain evolution. Incorporation of the thermal residual strains strongly alters the predicted deformation mode activities. The improved internal strain predictions provide greater confidence in these distinct deformation mechanism behaviors.

- The floor, roof and chimney modes combine to control the flow curves since they all need to be active for macroscopic plastic flow to occur.

- Micro-yielding indicated by inflections in the internal strain data obtained from the {110}, {111}, and {112} diffraction peaks can be predicted with the roof, chimney or $\langle 130 \rangle$ twinning modes.

- Deformation twinning was determined to be the primary cause of tension/compression asymmetry, but incorporation of thermal residual stresses improved the model predictions of the nature of the elastoplastic transition as well as internal strain evolutions.

- The predicted twin volume fraction closely matches previously reported measurements performed using EBSD on samples with different thermal processing.

- The grains with their crystallographic c-direction oriented along the loading direction do not significantly yield based upon the internal strain data, but the EPSC model requires plastic deformation of these grains for macroscopic flow of the stress-strain response. This apparent inconsistency remains to be explained.

Chapter 4

Effects of Hydrogen on the Mechanical Response of α-Uranium

C.A. Calhoun, E. Garlea, T. A. Sisneros, and S. R. Agnew [1]

4.1   Introduction

The presence of hydrogen can drastically reduce the ductility of metals even at small concentrations. There exists some controversy in the literature as to the specific mechanisms of how dissolved hydrogen degrades the ductility and fracture toughness. For the sake of completeness, we present the three prevailing mechanisms discussed in the literature, which are: (1) stress induced hydride formation, (2) hydrogen enhanced localized plasticity (HELP), and (3) hydrogen enhanced decohesion embrittlement (HEDE) [52, 53, 54]. Hydride formation leads to second phase particles that cause stress concentrations (including those due to dislocation pile-ups), which ultimately lead to the reduction in ductility. In some instances, hydrides can

form at the grain boundaries and lower their apparent cohesive strength by inducing stress concentrations, serving as sites for dislocation pileups, having low interface cohesive strength with the matrix phase, or intrinsic brittleness themselves. Any of these specific mechanisms would ultimately lower the ductility. However, the hydride mechanism is typically invoked in the context of Group 4 and 5 metals and alloys, like titanium, which have a higher solubility for hydrogen, which permits hydrides to form during loading in the stress fields around the crack tip [54]. It is often assumed that, in the cases where the reaction between the metal and hydrogen is exothermic, these hydrides readily form. Under conditions where hydrides do not form, the other mechanisms, (2) or (3) serve as cause for embrittlement. Under the HELP theory, it is believed that the hydrogen stays in solution and concentrates around dislocation cores. This alters the energetics of dislocation motion and ultimately promotes dislocation propagation and shear localization leading to failure.

In the decohesion theory, it is believed hydrogen lowers the cohesive strength, leading to cleavage or intergranular fracture. The latter case is believed due to H segregation to grain boundaries which lowers their cohesive strengths. Indeed, the decohesion mechanism often manifests itself by decreasing the resistance to intergranular cracking. It remains distinctly possible that embrittlement in the absence of hydride formation occurs as a combination of these two mechanisms. An example of the hydride formation is seen in the hexagonal close packed (HCP) metals titanium [55]. At low stress intensities, hydrides formed in the high stress regions around a crack tip in Ti and resulted in failure. The hydrides locally change the stress field around the crack tip, and ultimately serve as a path for crack growth. This was also observed in zircaloys, where the residual stress around the crack tip enhanced the precipitation of hydrides leading to accelerated crack growth rates [40].

α-Uranium has a relatively low solubility for hydrogen (0.0001 ppm) at room temperature and above which hydrides can form [56]. The formation of hydrides in α-uranium has been reported extensively [57, 58, 59, 60] . The hydride formed is UH$_3$, which has a simple cubic

crystal structure with a lattice parameter of 6.63 Å. These hydrides are known to form at the grain boundaries even at low concentrations of hydrogen (~0.2 ppm) in some cases [56, 60]. In a more recent study, Bingert et al. [60] confirmed that hydrides form at high and low angle grain boundaries and also observed hydrides along twin interfaces. Also, it is noted that localized residual stresses develop during hydride formation due to density mismatches between the cubic (hydride) and orthorhombic (α-uranium) phases which leads to a 70% volumetric change [56]. This large volume expansion leads to large local stresses that are believed to be responsible for the weakening of the grain boundary [56, 59]. Small angle neutron scattering has revealed hydrides form at submicron scale inside α-uranium [61]. The exact details of hydride nucleation and growth in polycrystalline uranium depends on the specific processing history [56].

α-Uranium possesses an orthorhombic crystal structure, which induces anisotropy in its thermo-mechanical response. In single crystalline form, the elastic [3], thermal expansion [5] and plastic [2, 30] properties all exhibit strong anisotropy. These lead to the generation of thermal residual stresses during cooling from annealing temperatures in polycrystals, which are strong enough to induce plastic deformation and can result in thermal ratcheting [7]. The anisotropy in the plastic deformation is realized through the activation of the 4 slip modes and 3 deformation twin modes. The [100](010) mode, denoted wall slip, serves as the primary (i.e., the softest) slip mode at room temperature and has only one slip system [6, 7]. The [100](001) mode, denoted floor, acts as a secondary slip mode, which involves cross-slip of [100] dislocations, and also contains only one slip system. At temperatures closer to the α to β allotropic transformation, the floor mode becomes the primary slip mode [6, 7]. The $\frac{1}{2}\langle 1\bar{1}0\rangle\{110\}$ mode, denoted chimney slip, is comprised of two slip systems and it exhibits a larger critical resolved shear stress (CRSS) than the primary slip modes at all temperatures up to the phase transformation temperature [2]. This has been observed, via slip trace analysis, in coarse-grained α-uranium at room temperature [7]. Finally, the $\frac{1}{2}\langle 1\bar{1}2\rangle\{021\}$ mode, denoted roof slip, has four

slip systems and the largest CRSS among all the modes, up to the transformation temperature of α-uranium. Roof slip is usually observed only near the β transition temperature in single crystals [2], but has been considered in crystal plasticity modeling of low temperature deformation [41] as it is necessary to close the single crystal yield surface [9]. The interplay between these different deformation mechanisms has been recently investigated [1, 8, 30, 31, 35].

Huddart et al. [62] observed that annealed uranium exhibits a combination of ductile tearing/dimpling and intergranular cracking in the absence of hydrogen, but did not seek to observe any hydrides. Hughes, Orman and Picton observed that annealed polycrystalline α-uranium fails through intergranular cracking in the presence of hydrogen and transgranular cracking without any hydrogen present [58]. Beevers and Newman [59] showed that hydrides formed at concentrations as low as 1.25 ppm along the grain boundaries. In addition to the microscopy, they conducted monotonic tension tests until failure to observe the changes in ductility with increasing hydrogen content. They observed a minimum occurred in the fracture stress at 2.5 ppm hydrogen. In a more recent study, it was observed that the drop in ductility plateaued at ~0.3 ppm hydrogen when hydrogen charged at 630 ^{o}C followed by a water quench [63].

The present paper documents a further investigation of the mechanisms of H embrittlement of aged polycrystalline α-uranium which is focused on elucidating any possible changes in the behavior of the active plastic deformation mechanisms at the grain-level. In-situ neutron diffraction experiments combined with polycrystalline plasticity were employed to study any changes in deformation behavior. Monotonic tension tests to failure and postmortem fractography allowed for the investigation of changes in ductility.

4.2   Sample Preparation

This same material was used in another publication [31], and for completeness, the processing history is included here as well. Depleted uranium was initially cast in to a 254 mm ingot. It

was hot cross-rolled at 640 ^{o}C to a thickness of 32 mm, then warm clock-rolled at 330 ^{o}C to a thickness of 15 mm, before an intermediate anneal of 480 ^{o}C for two hours. Subsequently, the plate was further warm clock-rolled at 330 ^{o}C to a gage of 7.6 mm and given a final anneal of 550 ^{o}C for two hours. Bars (~120 mm long) large enough for one compression and one tension sample were machined from the plate. They were oriented to place the loading axes of the samples parallel to the final rolling (RD) or transverse direction (RD) [9]. The bars were then charged with hydrogen to produce three different hydrogen concentrations: 0.0, 0.3 and 1.8 ppm (by weight) hydrogen, respectively. All of the specimens were charged with varying hydrogen partial pressures during the three hour charging anneal at 630 ^{o}C followed by a water quench. The 0.0 ppm sample stayed under a vacuum for the entire treatment. The 0.3 ppm and 1.8 ppm samples underwent two hours in a vacuum to ensure that all the hydrogen that might have been present in the bulk was eliminated before the desired amount of H_2 was introduced. The procedure published in ref. [63] was followed. That study showed how the partial pressure of hydrogen can be used to control the amount of hydrogen intake by the sample. For each level of charging, the processing left the material with a grain size of approximately 25 μm, as determined by optical metallography following ASTM E112-96. The hydrogen contents were not directly measured for the current study. Rather, the hydrogen content was assumed to be similar to those reported and measured in ref. [63]. Similar embrittlement behavior at each charging level was observed, providing evidence in support of this assumption.

After the hydrogen charging process was completed, threaded round dog-bone tensile specimens and cylindrical compressive specimens were electro-discharge machined (EDM'd) out of each of the bars. It is noted that any oxide that could form during the water quench and the possible surface-rich-hydrogen is removed during machining to form the specimens. The machining of the surface helps to ensure a homogenous hydrogen bulk distribution. The tension samples had a diameter of 5 mm inside the test gauge. The compression specimens were right cylinders with a diameter of 6.25 mm and a height of 15.75 mm, and oriented with the

cylindrical axis parallel to the rolling direction. It is noted that hydrogen could have been intro-duced during EDM'ing. However, the ductility and fracture surface of the nominally uncharged specimens suggest that only minimal hydrogen uptake could have occurred.

Prior to in-situ testing, the texture of the material was measured using the HIgh-Pressure-Preferred Orientation (HIPPO) instrument at Los Alamos National Laboratory. Details of the technique can be found in the literature [42]. The diffraction data were analyzed using MAUD software package to compute the complete orientation distribution function (ODF), the details of which are found in the literature [64]. The pole figures were ultimately plotted using MTEX software package [65]. Figure 4.1 shows a representation of the initial textures for two different charged samples, 0 ppm and 1.8 ppm respectively showing the variation between them. For brevity, only two of the initial textures are reported, since these represent the largest variation between samples and they are still quite similar. The variation in texture features and intensity did not seem to correlate to hydrogen charging level and appeared random. In the pole figures, the (020) poles align with the rolling direction of the final pass, and the (002) poles align along the normal direction to the rolling. As compared with the as-received samples [30], a slight decrease in the (002) peak intensity is observed after the hydrogen charging anneal.

4.3 Mechanical Deformation Experiments

All of the mechanical deformation experiments were conducted on the Spectrometer for MAte-rials Research at Temperature and Stress (SMARTS) in the Manuel Lujan, Jr. Neutron Scatter-ing Center (LANSCE), at Los Alamos National Laboratory [27]. One set of experiments was conducted with in-situ lattice strain monitoring, and the other set was conducted without the neutron diffraction monitoring, referred to here as ex-situ. The ex-situ experiments were con-ducted to failure and were used to illustrate the changes in ductility between the charging levels, while the in-situ experiments will reveal any changes in the onset of the different deformation
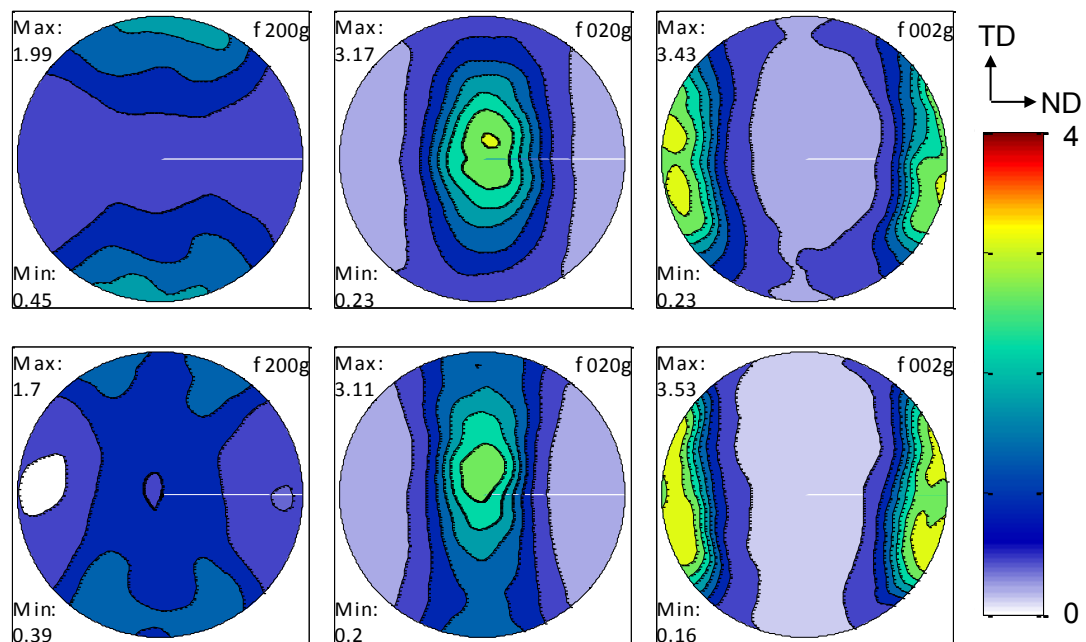
Figure 4.1: Initial texture taken from (top) 0.0 ppm TD tension sample (bottom) 1.8 ppm TD compression sample.

mechanisms. Standard ex-situ uniaxial tension experiments were conducted with a constant displacement rate of 1.68 mm/min, which resulted in an initial strain rate of $1.0\mathrm{x}10^{-3}$ s^{-1}, with a 10 mm gage length extensometer.

During in-situ experiments, specimens undergo uniaxial tension/compression while being irradiated with neutrons. The spallation source at LANSCE supplies packets of neutrons with a range of velocities (i.e. wavelengths). Knowing the distance between the chopper (time zero location) and the detector, along with the corresponding time of flight allows for the measurement of the speed, which is then turned into a wavelength via the de Broglie equation: $\lambda = \frac{ht}{mL}$, where h is Plank's constant, t is the time of flight, m is the mass of an electron, and L is the length of the flight path. From the wavelength, λ, Bragg's law reveals the lattice- or d-spacing. Such an approach allows for a complete diffraction spectrum to be obtained with fixed diffraction geometries, unlike monochromatic x-ray and neutron diffraction where sources and/or detectors must be moved to collect a spectrum with a constant diffraction vector. Each diffraction spectra required 20 - 40 min. of collection time. The positioning of the detectors places the diffraction vectors parallel to the loading direction and perpendicular to it, as shown in Figure 4.2. Currently, only the strains along the loading direction are considered, as this is the most sensitive to the imposed mechanical deformation.
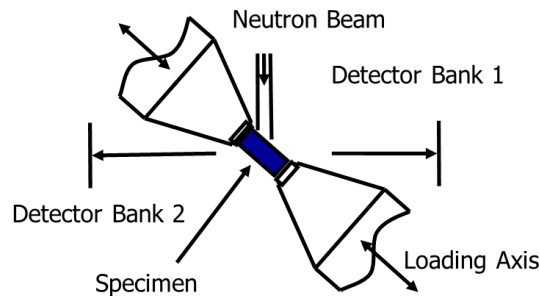
Figure 4.2: Schematic showing the testing geometry, showing the detector banks oriented in such a way that the diffraction vector associated with Bank 2 is parallel to the loading direction and that of Bank 1 is normal to the loading direction.

The change in lattice spacing during deformation for different *hkl* diffraction peaks provides insight into the plastic deformation mechanisms active, and when used in conjunction with micromechanical modeling, can be used to quantify the relative strengths, as seen in work by the current authors on uranium [30, 31], beryllium [66], zirconium [67], stainless steels, intermetallics [68], and magnesium [48]. Here, the measurements are used to show any changes in deformation mechanisms between the different levels of hydrogen charging. A strain is associated with each *hkl* diffraction peak and is computed using a standard engineering strain definition given by equation 4.1:

$$\varepsilon^{hkl} = \frac{d^{hkl} - d_o^{hkl}}{d_o^{hkl}} \tag{4.1}$$

where d^{hkl} is the lattice spacing at the current load increment, and d_o^{hkl} is the lattice spacing at zero macroscopic stress. Ideally, d_o^{hkl} would be the stress free lattice parameter. However, this material has strong intergranular residual stresses, and the experimental setup is most accurate at measuring a relative changes in lattice spacing rather than precise determination of lattice parameters. As such, the initial value of the *d*-spacing was used to normalize the relative changes observed for each set of grains interrogated. Each *hkl* reflection parses from all of the grains within the irradiated volume, those grains which with {hkl} planes perpendicular to the diffraction vector. Information about the strength of each set of grains is revealed by the amount of internal strain carried by that set of grains. For example, grains that show higher internal strain are typically considered to be harder in elastically isotropic materials, since the stress is directly related to the strain. In anisotropic systems with large thermal residual strains, all of these details become convoluted. Polycrystalline plasticity modeling is needed to interpret these results. Further details of the experimental setup are found in the literature [27, 45].

To further interpret the in-situ diffraction experiments, polycrystalline plasticity modeling,

specifically the Elasto-Plastic Self Consistent (EPSC) model is employed. Complete details of the model are presented in the paper of Turner and Tome [20], and the exact treatment currently employed is presented in ref. [31]. In this model, a polycrystal is discretized into a finite set (14,000-16,000 depending upon the case) of "grains." The grains are assigned an orientation (i.e. a set of Euler angles following a Bunge convention) and a volume fraction in order to best represent the experimentally measured crystallographic texture. Each grain is assumed to exhibit an elastic-plastic single crystal response given by the fully anisotropic Hooke's law and Schmid-based rules for slip system activation, respectively. (Again, see previous publications [31, 20] for details). Each grain is assumed to be embedded in an anisotropic homogenized effective medium, and a self-consistent homogenization scheme is used to iteratively determine the properties of the medium during each incremental straining step. To compare with the experiment, the volume-averaged lattice strain along the loading direction of all of the grains which satisfy a given diffraction condition is computed for each loading increment.

4.4   Results

Figure 4.3 shows the results from the ex-situ experiment performed at SMARTS in which samples H charged to 0.0, 0.3, and 1.8 ppm where pulled until failure along the in-plane direction which is transverse to the final rolling direction. The ductility is observed to decrease with increasing hydrogen content. As was previously seen [63], hydrogen charging to 0.3 ppm decreased the ductility appreciably, and charging to 1.8 ppm reduced the ductility even further. Additionally, it is seen that the macroscopic stress-strain response does not appreciably vary between the hydrogen charging conditions.

Neutron beam availability limited the number of in-situ experiments that could be conducted. As such, the researchers chose to focus on the two extreme (0.0 and 1.8 ppm) conditions under as many loading conditions as possible rather than test all three hydrogen levels
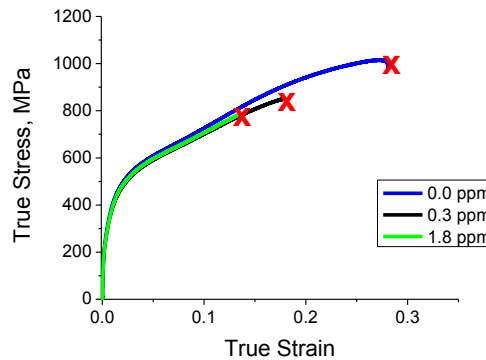
Figure 4.3: Comparison of the stress-strain response along the transverse direction under tensile loading showing the drop in ductility with increased hydrogen content.

under fewer loading directions. Prior studies have shown that different loading directions activated different deformation mechanisms at different applied stress levels [31, 35], so with the aim of identifying changes in individual deformation mechanism activities, examining more loading conditions was viewed as a priority. Compression experiments were conducted along RD and TD, and tensile experiments were conducted along RD. In all of these experiments, the diffraction spectra were analyzed for the presence of peaks associated with the UH_3 hydride, but no such peaks were observed. Given the low level of H charging, the hydrides would only comprise a very small volume fraction of the material. At a maximum, that would be 2.5 x 10^{-4} and 4.1 x 10^{-5} for the 0.3 and 1.8 ppm hydrogen samples, respectively. Thus, it was not expected that the hydride peaks would be observable. In addition, changes in the level of background scattering due to incoherent neutron scattering of the hydrogen were also considered but they were not apparent, which is likely due to large hydrogen content of the rubber bands used to attach the extensometer.

Figure 4.4 shows a comparison of the response seen during the RD compression loading for the 0.0 and 1.8 ppm hydrogen charged samples. Here we present engineering stress and strain, since they were directly measured with the load cell and on-sample extensometer on the load frame, Figure 4.4a. We note the 'saw tooth' appearance of the stress-strain curves comes

from relaxation that occurs during constant displacement dwells to collect the neutron diffraction patterns, and is consistent with similar in-situ neutron diffraction experiments performed on other materials. The internal strain evolution, symbols in Figure 4.4b and macroscopic flow curves from the two different sample types nearly overlap each other during the entire experiment. For clarity, only three {hkl} strains are included, but the results were consistent across all 11 different {hkl} strains monitored, which were {200}, {020}, {040}, {002}, {110}, {111}, {112}, {113}, {021}, {041} and {131}. Also included in Figure 4.4 are the results from Elasto-Plastic Self-Sonsistent (EPSC) modeling used to interpret the in-situ diffraction observations. Details of the modeling procedures are found in ref. [31]. However, it is important to mention one important aspect. Due to the thermal expansion, elastic, and plastic anisotropies of the material, strong thermal residual stresses are present within the material after cooling from the H charging temperature. These effects are accounted for in the current modeling, with the assumption that H content does not effect this phenomenon.

Figure 4.4: Comparison of (a) macroscopic stress-strain response, (b) internal strain and (c) normalized peak intensity evolution for 0.0 ppm and 1.8 ppm hydrogen charging tested along RD in compression. EPSC model predictions are included to show the understanding of relevant deformation mechanisms.

The model well-describes qualitative features of the macroscopic stress-strain response as well as the internal strain evolution. This qualitative agreement between the model and both H charging conditions examined suggests that there is no difference in thermal residual stress

development and it allows comments to be made about deformation mechanism activity. For example, such modeling has shown that, under compression along RD, yielding is controlled by the onset of twinning, with twinning volume fractions nearing 20% at 10% strain [1, 8, 31]. The strong intensity shift of the {040} peak (Figure 4.4c), which represents a large volume fraction of the material based upon the RD direction texture in Figure 4.1, indicates twinning occurred in these grains. In particular, it is known that the {130} twinning mode is the predominant twin mode during RD compression, as evidenced by prior EBSD [1]. Also, from the post deformation texture measurements discussed later, the large texture shifts indicate strong texturing. The nearly identical response of the samples with distinct H charging levels provides strong evidence that the presence of small concentrations of hydrogen does not affect the onset of twinning, particularly the {130} mode in this material system.

Figure 4.5 presents a comparison of the response seen during the TD compression loading for the hydrogen charged and un-charged samples. Again, the internal strains and macroscopic stress-strain response are nearly identical between the two charging conditions. The {002} grains appear to have a slight yield around 400 MPa, macroscopically, in both conditions, and the {040} and {111} grains yield at nearly the same macroscopic load. Also, the shifts in intensity of the {040} peak indicates twinning, but this peak only represents a small volume fraction of the material, as the {020} pole figures have a low intensity along TD (Figure 4.1). Also included in Figure 4.5 are more EPSC modeling predictions explained in ref. [31]. The modeling and experimental observations has shown that TD compression deformation is controlled by both slip and twinning activity [1, 8, 31], which is seen by the lack of strong texture evolution (in the next section). As such, we can conclude that the relative contributions from the multiple deformation mechanisms does not change between the two hydrogen charging levels, at the grain-level, as revealed by polycrystal measurements and polycrystal plasticity simulations.

Figure 4.6 shows the SMARTS data collected during the two tensile tests conducted along the RD for the hydrogen charged and un-charged case. In this case, the {002} grains are seen to
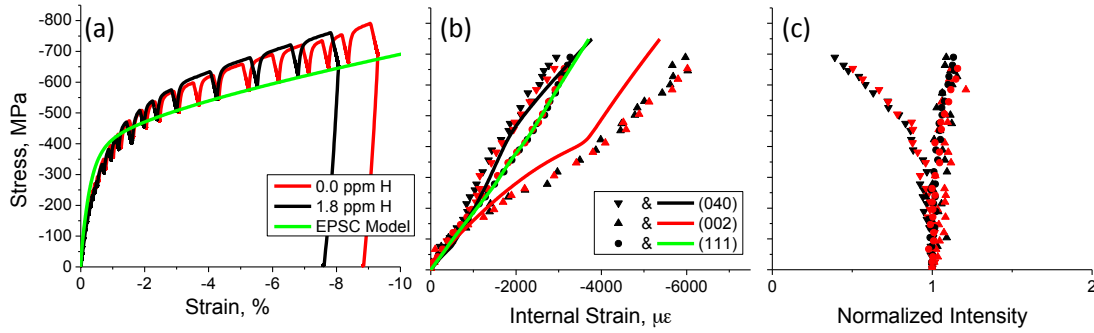
Figure 4.5: Comparison of (a) macroscopic stress-strain response, (b) internal strain and (c) normalized peak intensity evolution for for 0.0 ppm and 1.8 ppm hydrogen charging tested along TD in compression. EPSC model predictions are included to show the understanding of relevant deformation mechanisms.

carry the most elastic strain, and do not appear to yield during the entire deformation process. Under compression, this orientation yielded by twinning, so the lack of yield is understood through the effects of thermal residual stresses and the polar nature of twinning [31]. It is seen that the data in both the internal and macroscopic strains overlap between the two levels of hydrogen charging.
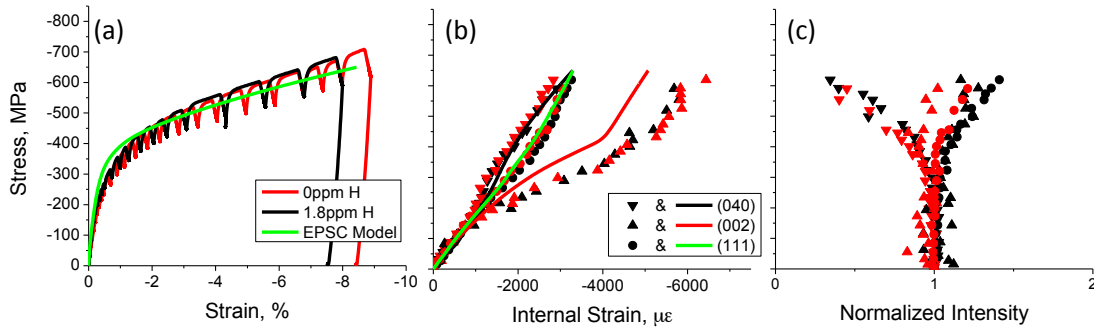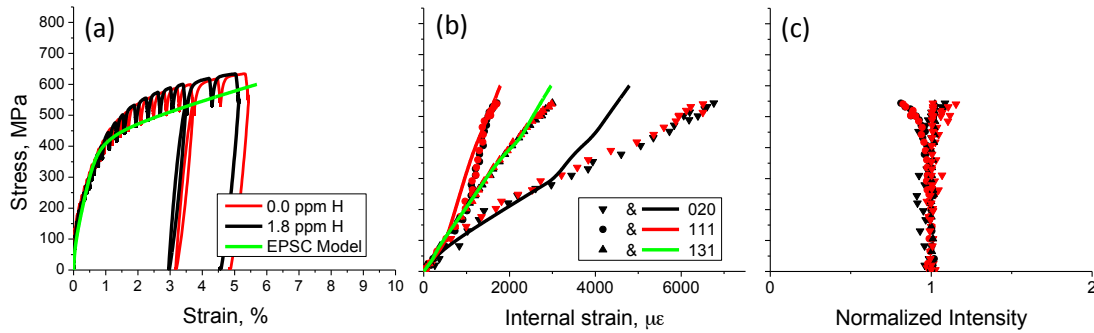

Figure 4.6: Comparison of (a) macroscopic stress-strain response, (b) internal strain and (c) normalized peak intensity evolution for 0.0 ppm and 1.8 ppm hydrogen charging tested along RD in tension.

Also included in Figure 4.6 are more EPSC modeling predictions explained in ref. [31]. Aside from the deviation between the predicted and measured internal strain within the {002}

grains, the model does a particularly good job of capturing the stress-strain response, including the microyielding behavior, as well as the internal strain evolution. This gives confidence that the model is well capturing the behavior of the individual deformation mechanisms. This case has been shown to be predominated by dislocation slip with twinning only playing a minor role in the deformation [1, 8, 31]. As such, we can conclude that overall slip activity within the grains is not affected by the presence of hydrogen in the sample.

After the in-situ deformation experiments were completed, the post deformation dimensions were measured on the compression cylinders. Specifically, the dimensions in the RD, TD and ND were measured. True strain was defined by comparing the post deformation dimension with the initial dimension, $\varepsilon = ln\frac{l}{l_o}$, where l is the final length, l_o is the initial length, and ε is the strain. Strain ratios values were defined by dividing the transverse strains by the loading direction (LD) strain for the compression samples. R-ratios between the transverse strains were defined by dividing the TD or RD strain by the ND strain, depending upon which was orthogonal (OD) to the loading direction. For example, OD is TD for the RD compression samples and RD for the TD compression samples. Table 4.1 presents the strain ratios measured on these samples as well as the associated R-values and polycrystal plasticity modeled values at the end of deformation.

The strain ratios and R-values are consistent across the two different hydrogen levels for both straining directions; i.e., there does not appear to be any dependence upon H content. The model qualitatively captures the type of plastic strain anisotropy observed. For example, the trend of less strain occurring in the ND (R-value greater than 1), during both RD and TD compression, was consistent between the model and experiment. Additionally, the TD samples and model exhibited higher R-values than the RD. The model does over predict the level of out-of-plane anisotropy (higher R-values are predicted than observed along both directions). The model under predicts the level of in-plane anisotropy (it predicts that the R-value will be similar for the RD and TD samples), while the RD is experimentally observed to have a significantly

lower R-value than the TD). R-values are strongly dependent upon the initial crystallographic texture (see Figure 4.1) and relative contributions of the individual slip and twinning mechanisms. The fact that the R-values are insensitive to the H content provides evidence that H charging does not influence the relative deformation mode activities.

Loading Direction	H Content	ND/LD	OD/LD	R-Values
RD compression	0 ppm	-0.51	-0.69	1.35
	1.8ppm	-0.56	-0.68	1.21
	Model	-0.31	-0.67	2.15
TD compression	0 ppm	-0.38	-0.78	2.05
	1.8ppm	-0.39	-0.78	2.08
	Model	-0.28	-0.70	2.5

Table 4.1: Post deformation dimensions comparing the transverse strains (along ND or OD) over the loading direction (LD) strains, as well as the R-values, which are the ratios of the two transverse direction strains as defined in the body text.

Deformation texture evolution is the net result of the imposed boundary conditions and the active mechanisms of plasticity (i.e. slip and twinning). Hence, like plastic anisotropy discussed above, the texture provides clues regarding which deformation mechanisms were responsible for accommodating the imposed strain. Post-deformation textures were measured in the same fashion as the pre-deformation textures on HIPPO. Figures 4.7-4.9 show the post deformation textures for the 6 samples (0 ppm and 1.8 ppm conditions) tested mechanically with in-situ neutron diffraction. 4.7 shows the comparison of the RD compression samples. In both cases, it is clearly seen that the strongest texture evolution is seen under RD compression, which is consistent with previous results [1, 35]. The {020} intensity shifts from along the rolling direction before deformation to the transverse direction. Also, we see the {200} peak intensity along the loading direction increase. These observations are seen for both levels of H charging. 4.8 shows a comparison of the post deformation textures for the RD tension experiments. The results show that both samples show little texture evolution during defor-

mation, which is consistent with prior studies [31, 35]. The lack of texture evolution provides

clear evidence that twinning is not a predominant deformation mechanism during this loading.

Figure 4.9 shows a comparison of post deformation textures after TD compression. It is noted

that the increased intensity of the {020} pole in the hydrogen charged sample existed prior to

deformation and was seen post deformation. It remains unclear why the initial texture varied,

but the same trend in texture evolution was observed in both samples despite having slightly

different starting textures.
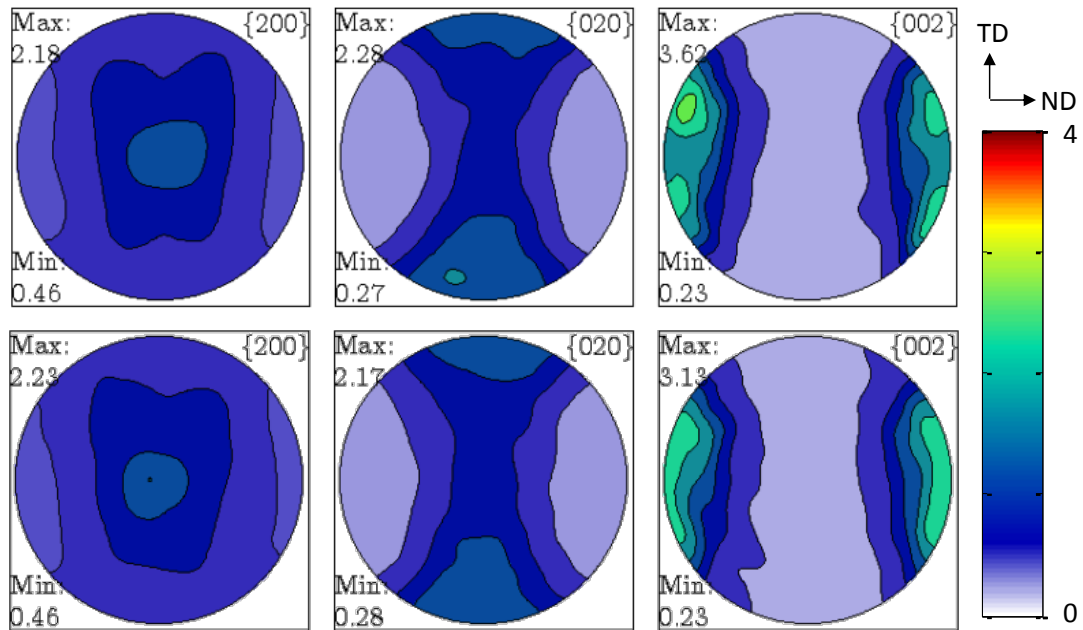
Figure 4.7: Comparison of post deformation pole figures after RD compression in the 0.0 ppm (top) and 1.8 ppm (bottom) sample loaded while collecting in-situ neutron diffraction data.

4.4.1 Fractography Analysis

After the TD tension experiments to failure (shown in 4.3), the fracture surface was investi-

gated by scanning electron microscopy. Figure 4.10 shows images of the facture surface from

three TD tension samples that were monotonically strained until failure. It is clearly seen that
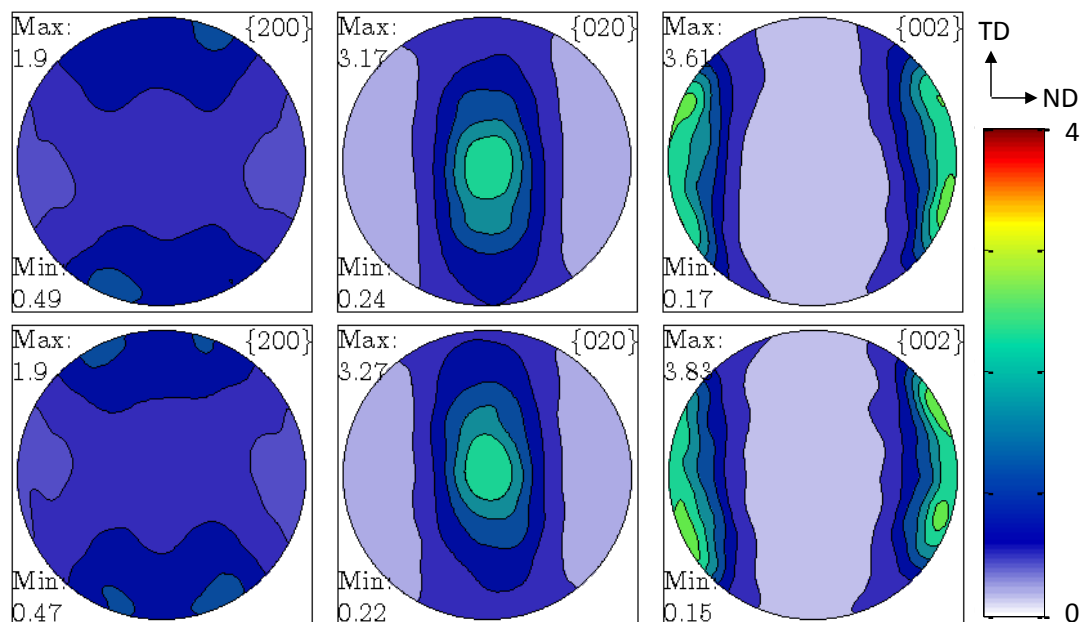
Figure 4.8: Comparison of post deformation pole figures after RD tension in the 0.0 ppm (top) and 1.8 ppm (bottom) sample loaded while collecting in-situ neutron diffraction data.
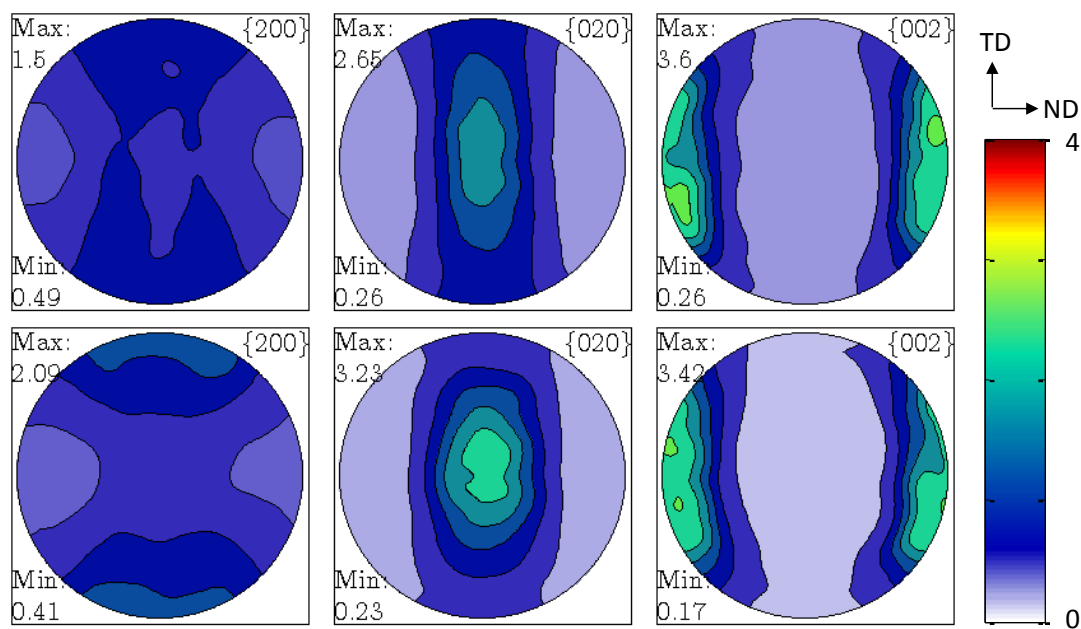
Figure 4.9: TD Comparison of post deformation pole figures after TD compression in the 0.0 ppm (top) and 1.8 ppm (bottom) sample loaded while collecting in-situ neutron diffraction data.

the uncharged sample (Figure 4.10a) exhibits a transgranular, ductile fracture mode involving microvoid nucleation, growth and coalescence evidenced by dimples all over the fracture surface. At 1.8 ppm (Figure 4.10c), the fracture surface is clearly intergranular. The 'rock candy' grain structure of the fracture surface is indicative of grain boundary decohesion, as are the perpendicular cracks indicated by arrows that also appear to be along grain boundaries. In the 0.3 ppm sample (Figure 4.10b) a combination of two fracture modes is observed. For the most part, the surface shows of intergranular cracking, but some localized ductile tearing is suggested by small regions of dimpling. These images clearly show a transition of fracture mode with hydrogen content, consistent with reports that hydrogen weakens the grain boundaries [56]. This conclusion agrees with prior observations of intergranular cracking in the presence of hydrogen and transganular fracture in its absence [56, 58, 59, 62].
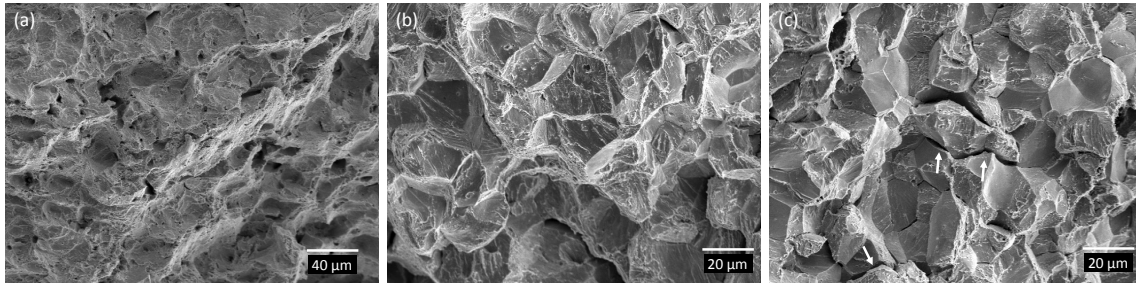
Figure 4.10: SEM images taken at 2000X of the fracture surface from the TD tensile test to failure from: (a) 0.0 ppm (b) 0.3 ppm and (c) 1.8 ppm charged samples showing the shift from transgranular cracking to intergranular cracking.

4.5   Discussion and Conclusions

Uniaxial tension tests to failure and subsequent fractography revealed a drop in ductility and transition from transgranular to intergranular cracking with the presence of hydrogen in the aged uranium. These two observations reiterate the previously observed fact that the hydrogen charging lowers the cohesive strength of the grain boundaries. As such, it is hypothesized

that the hydrogen concentrates at the grain boundaries as either segregated solute, hydrides, or both. Such mechanisms explain the drastic decrease in ductility despite the relatively low concentration of hydrogen (at most only 1.8 ppm, which is the maximum intake at atmosphere pressure).

Since the equilibrium solubility is so low, let's consider the possibility that all of the hydrogen precipitated out of the matrix. This would result in a volume fraction of 2.4×10^{-4} of hydride in the polycrystal. By approximating the $\sim 25 \ \mu$m sized grains as cubes and assuming all of the precipitation occurs at the grain boundaries (in agreement with recent observations [60]), this could result in roughly an even coating of 10 nm thick hydride at the grain boundary. It is known that sub-micron hydrides form under the hydrogen charging conditions [61]. While it is highly unlikely that the hydride forms such an even layer, it becomes clear that even small amounts of H charging could strongly alter the grain boundary behavior. Additionally, it helps explain the previously observed 'saturation' of embrittlement, meaning that there is a level of H charging (~ 0.3 ppm) above which the ductility does not decrease further [63]. If the boundaries are already completely covered by grain boundary segregation or hydrides, no further hydriding or segregation will weaken the cohesive strength any further.

In addition, the previous observations regarding the rate sensitivity of hydrogen embrittlement (that higher loading rates do not prevent the H embrittlement effect [56, 59]) provide further evidence for the above mechanistic picture. Further, Powell et al. observed that the hydrogen level, above which the ductility does not further decrease, drops with increasing strain rate [63]. Other mechanisms for hydrogen embrittlement: HELP, dynamic hydride formation, and HEDE require diffusion of dissolved hydrogen, which is time dependent. Thus, the embrittling effects of these mechanisms are greater for slower loading rates. Pre-existing grain boundary segregation or hydrides does not require diffusion during the cracking process, and results in static weakening of the cohesive strength of the grain boundaries. At higher strain rates, stresses typically increase due to the increase in strength of thermally activated disloca-

tion glide, which would ultimately increase the decohesion stresses along the grain boundaries.

The microscopy employed was not sufficient to determine if any hydrides were present on the grain boundaries, though hydride formation appears likely. Some prior studies have observed hydrides on fracture surfaces while others have not [56]. Segregation of solute H atoms to the grain boundaries may also play a role, but this would lead to locally high super-saturation of H which could increase the driving force for nucleation of the hydride phase, which could in turn help to overcome the barriers to nucleation, including the large volumetric expansion associated with hydride precipitation. In addition to the drop in ductility, the effects of hydrogen on the plastic deformation mechanisms were also studied using the in-situ neutron diffraction method. The macroscopic flow curves, internal strain evolutions, plastic strain anisotropies, and texture evolutions were observed to be consistent, independent of hydrogen concentration within the range examined (0.0 to 1.8 ppm). From the internal strain evolutions, it becomes clear that this amount of hydrogen charging does not affect the onset of any plastic deformation mechanism (slip or twinning), at the grain-level. Further, we can deduce that the apparent weakening of the grain boundaries does not affect the thermal residual stress development, since it is highly improbable that hydrogen would simultaneously alter the residual stress and plastic deformation in such a way to produce identical deformation behaviors. From the similarity of the plastic strain anisotropies and texture evolutions, it can be concluded that the grain-level activities of the various plastic deformation mechanisms are not altered by H charging up to the level examined. This result is scientifically satisfying, since neither the expected (on the basis of the fracture mode transition and low equilibrium bulk H solubility) grain boundary hydride precipitation or H solute segregation to grain boundaries are expected to drastically affect the plastic response of the grains themselves.

4.6   Acknowledgements

Chapter 5

In-situ neutron diffraction characterization of temperature dependence of deformation in α-U

C.A. Calhoun, E. Garlea, T. A. Sisneros, and S. R. Agnew [1]

5.1 Introduction

Orthorhombic α-uranium exhibits high single crystal anisotropy in its elastic [3], thermal expansion [4, 5] and plastic response [6, 7], which leads to highly anisotropic textured polycrystals. In addition to the anisotropy at a given temperature, studies on single crystals have shown these properties possess individual temperature dependencies [2, 3, 5]. The single crystal anisotropy is so strong it can lead to thermal ratcheting in textured materials [69].

The plastic anisotropy comes from the active deformation mechanisms, which include 4

---

dislocation slip modes and 3 deformation twinning modes [1, 6, 7]. The 4 slip modes are, in ascending order in relative strength at room temperature: (1) [100](010) mode, denoted *wall slip*, (2) [100](001) mode, denoted *floor*, (3) $\frac{1}{2}\langle 1\bar{1}0\rangle\{110\}$ mode, denoted *chimney slip*, and (4) finally, the $\frac{1}{2}\langle 1\bar{1}2\rangle\{021\}$ mode, denoted *roof slip* [6, 7]. Single crystal studies have revealed that each of the slip modes portrays a unique temperature dependence [2]. All of the slip modes exhibited a typical thermally activated nature with each having a unique thermally activated plateau in both stress and temperature range. Three twinning modes usually occur in addition to the slip modes. The $\langle 3\bar{1}0\rangle\{\bar{1}30\}$ twin mode has two twin variants. It is the most widely observed twinning mode and is a compound twin with a shear of 0.299 [1, 6, 10]. Single crystal studies have shown that this twin mode softens slightly with temperature, but does not portray the thermally activated nature seen by the slip modes [2]. A recent electron backscatter diffraction (EBSD) study on samples deformed at room temperature showed this mode to be the predominant twin mode, and comprised a large majority of the twinning [1]. The $\langle 3\bar{1}2\rangle\{172\}$ twinning mode has four twin variants and is a type II twin with a shear of 0.227 [1, 6, 11]. The $\langle 3\bar{7}2\rangle\{112\}$ mode has four twin variants and is a type I twin with a shear of 0.227. To date, crystal plasticity modeling studies carried out on uranium have neglected this mode since its contribution cannot be discriminated from the $\langle 3\bar{1}2\rangle\{172\}$ mode and is seen in smaller fractions [1, 6, 10].

The anisotropy in the crystalline thermal expansion coefficients leads to the development of thermal stresses during cooling from thermo-mechanical processing temperatures [30]. In the *b* direction, the coefficient of thermal expansion is negative or near zero, while both the *a* and *c* direction exhibit positive thermal expansion [4, 5]. These stresses have been shown to induce plastic relaxation mechanisms [30] and leave annealed polycrystals with inter-granular residual stresses at room temperature. Zirconium and its alloys have similar concerns with thermal residual stresses, but are not strong enough to exceed the elastic limit [20]. The Elasto-Plastic Self-Consistent (EPSC) model which has been employed to address thermal residual

stresses in Zr alloys [20] is extended to α-uranium [30].

There have been a few recent studies on the deformation of textured, polycrystalline α-uranium. Brown et al. studied the deformation of clock-rolled plate using in-situ neutron diffraction [33]. Tensile loading was done along the rolling direction at room temperature, 200 ^{o}C, and 400 ^{o}C as well as the transverse (in-plane) direction at room temperature. It was shown that the material primarily deformed due to slip, as evidenced by no large shifts in diffraction peak intensity and little texture evolution until very large strains. It was also seen that the material softened with increasing temperature which is consistent with slip based deformation in metals. McCabe et al. studied room temperature deformation behavior using a combination of EBSD and conventional stress-strain curves [1]. The Visco-Plastic Self-Consistent (VPSC) model well predicted the shape of the flow curve, and the measured twin volume fractions from the EBSD study. However, such a model is more numerically stable and computationally efficient than other crystal plasticity models. In a follow up work by Knezevic et al., the VPSC model was extended to account for the rate and temperature sensitivity of deformation in clock-rolled α-uranium [35]. This study included stress-strain response collected at various temperatures primarily in compression along the transverse direction and the through thickness direction. Most of the tests were performed under quasi-static conditions, while a few tests were conducted in a split-Hopkinson pressure bar to achieve higher strain rates.

In a previous work by the current authors, the effects of thermal residual stresses on room temperature deformation were analyzed using an EPSC model and in-situ neutron diffraction [31]. Samples were cut from an annealed plate and received an additional annealing treatment after machining. Compression tests were conducted along the rolling and transverse directions in a clock rolled plate as well as a tension test along the rolling direction. It was confirmed that twinning serves as a dominant deformation mechanism during compression along the rolling direction at room temperature. In the current paper, the previous EPSC modeling and in-situ

diffraction experiments are extended to investigate the effects of temperature on compressive loading along the rolling direction in a clock-rolled plate. The flow stresses of the slip modes are modified using the temperature sensitivities calibrated from VPSC modeling [35], while the hardening behavior of individual deformation modes is approximated as linear and empirically fit.

5.2 Methods

5.2.1 Experimental Methods

The material used for this study was the same material as published in Ref. [33]. The depleted uranium was initially cast as a 254 mm thick ingot. The ingot was first hot cross-rolled at 640 ^{o}C to 32 mm then warm clock-rolled at 330 ^{o}C to 15 mm before an intermediate anneal of 480 ^{o}C for 2 h. Subsequently, the plate was further warm clock-rolled at 330 ^{o}C to 7.6 mm and reportedly given a final anneal of 550 ^{o}C for 2h. Samples were electro-discharged machined from the plate, and tested in the as-machined condition with no additional heat treatment. Identical processing conditions were reported by many other researchers [1, 33, 35], but despite these nearly identical conditions, variation between the response of loading along the rolling direction (RD) in compression was seen to occur. It is noted that the grain size between samples were consistent and textures were similar across all of these studies, but the mechanical response varied between the different studies. The processing left the material with a typical clock-rolled texture, which is shown in Figure 5.1. All of the pole figures presented in this work were computed from orientation distribution functions that were computed using complete diffraction spectra collected on HIPPO in the Lujan Center of Los Alamos National Laboratory. More details of the neutron texture measurement can be found in reference [42].

In-situ neutron diffraction experiments were conducted at Los Alamos National Labora-
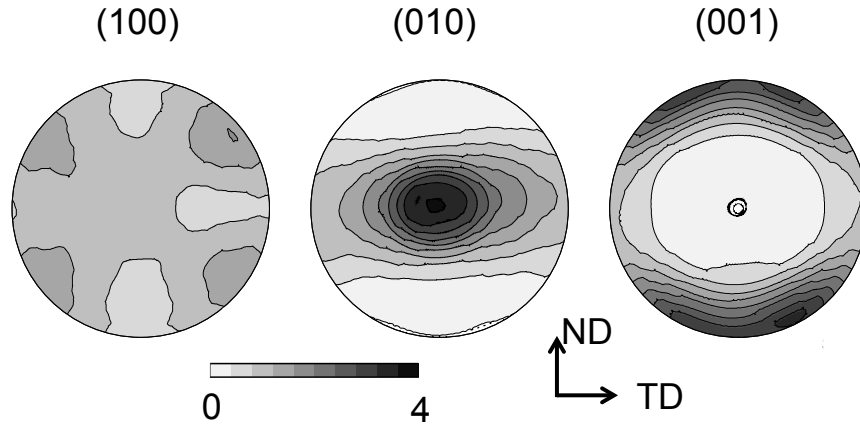
Figure 5.1: The measured pole figures from the room temperature sample prior to deformation. The loading direction is out of the page.

tory in the Lujan Center on the Spectrometer for Materials Research at Temperature and Stress (SMARTS) instrument. The experimental setup used for neutron diffraction has been published elsewhere [27, 33]. Neutron diffraction experiments allow for the monitoring of internal lattice spacings during deformation in large polycrystal samples. This gives insights into the distribution of stress between differently oriented grains, as the lattice strains are a direct result of either thermal expansion or elastic deformation. Specimens underwent compression loadings at room temperature (23 ^{o}C), 100 ^{o}C, and 150 ^{o}C while inside the neutron beam. Samples were loaded incrementally and held long enough to collect sufficient diffraction data, which required about 20 minutes per measurement. In the elastic region, this loading is performed in stress increments, but through the elasto-plastic transition and beyond, the loading was done in displacement increments. It is noted that the hold in load causes relaxation during the dwells, as evidenced by the saw tooth nature of the stress-strain curves.

The spallation source supplies packets of neutrons with a range of velocities (i.e. wavelengths). Knowing the distance between the chopper (time zero location) and the detector, along with the corresponding time of flight allows for the measurement of the speed, which is then turned into a wavelength via the de Broglie equation: $\lambda = \frac{ht}{mL}$, where h is Plank's constant,

t is the time of flight, m is the mass of an electron, and L is the length of the flight path. From the wavelength, Bragg's law reveals the lattice or d-spacing. This allows for a fixed diffraction geometry (unlike in typical x-ray measurements or monochromatic sources of neutrons, where the diffraction angle 2θ is varied during an experiment). The positioning of the detectors puts the diffraction vectors parallel and perpendicular to the loading direction in the case of uni-axial deformation experiments as illustrated in previous publications [27].

Monitoring the change in lattice spacing for different *hkl* diffraction peaks as a function of macroscopically applied stresses and strains provides insight into the plastic deformation mechanisms. A strain is associated with each *hkl* diffraction peak and is computed using a standard engineering strain definition given by equation 5.1:

$$\varepsilon^{hkl} = \frac{d^{hkl} - d_o^{hkl}}{d_o^{hkl}} \tag{5.1}$$

where d^{hkl} is the lattice spacing at the current load increment, and d_o^{hkl} is the lattice spacing at zero macroscopic stress. Ideally, d_o^{hkl} would be the stress free lattice parameter, but since this material has strong residual stresses and the experimental setup is most accurate at measuring a relative change in lattice spacing, the initial value to provide a relative change is used. The same protocol is employed in the simulation tool described below, such that the comparison between model and experiment is consistent.

It is noted that each *hkl* reflection corresponds to the measurement of all of the grains with the {hkl} planes perpendicular to the diffraction vector. As such, a set of grains {hkl} refers to all of the grains with a *hkl* plane perpendicular to the loading direction. Generally, grains showing higher internal strain represent hard grains, since the stress is directly related to the strain (through Hooke's Law). However, elastic anisotropy and thermal residual stresses convolute direct interpretation of this data, so polycrystalline modeling is required for even an initial assessment. Elastic anisotropy influences the resulting strains, because more compli-

ant grains carry more strain for a given stress. Thermal residual stresses and variations in specimen positioning affect the absolute d_o^{hkl} value, so the internal strains seen here represent relative shifts in elastic strains rather then a measure of the value of internal strain relative to the macroscopically stress free state.

5.2.2   Modeling Approach

The EPSC modeling scheme originally presented in Turner and Tome is employed [20]. Previously, the model was utilized to predict the development of thermal residual stresses [30], and to analyze the effects of these residual stresses in α-uranium on deformation at room temperature [31]. In such a model, a polycrystal is seen as a collection of single crystal grains with unique crystallographic orientations with respect to the sample/processing directions (i.e. rolling and normal directions). Each grain's response is given by an elasto-plastic single crystal law which accounts for the slip and twin modes. For each system inside the grain, the resolved shear stress is computed, and when it reaches the threshold value, the critical resolved shear stress (CRSS), the possibility of plastic deformation is explored. The resolved shear stress (RSS) must remain equal to the evolving CRSS through the straining increment to be activated. The CRSS is assumed to evolve with plastic activity, through a linear hardening law in the present study, for the sake of simplicity. The model of Clausen et al. is employed to simulate twinning [21]. In this model, volume fraction is transferred to a new grain with the proper orientation of the twin based on the stress state of the parent. Two key short comings of this model are: (1) only the stress state within the parent grain are considered, i.e. stresses inside the twin cannot propagate twinning further, [47] and (2) the stress state of a child and a parent are not directly tied to each other. It is noted that twinning relaxes stresses in three stages, nucleation, propagation and thickening (though not all twinning mechanisms undergo thickening).

To account for the interaction between grains, each grain is seen as an ellipsoid inside a homogeneous effective medium, which represents the average response of the polycrystal (i.e. the bulk response). Through the use of the Eshelby solution, the local stresses and strains are computed from the imposed stress and strain state. The effective properties of the aggregate are iteratively converged on through the self-consistent scheme [20]. The thermal residual stress state is computed using a certain set of CRSS values for cooling (see ref [30]) from 550 ^{o}C to room temperature. In order to predict the evolution of thermal residual stresses present within the sample at the beginning of the elevated temperature $in - situ$ compression tests, another set of CRSS values appropriate for lower temperature deformation (25-150 ^{o}C) was employed to simulate the stress free heating prior to simulating the mechanical deformation.

To account for the temperature dependent plastic properties, the CRSS and hardening rates for each slip system were adjusted for each temperature. However, the twinning modes were considered athermal. The temperature dependence of dislocation slip is understood in terms of thermal activation, both glide and dynamic recovery as well as the temperature dependence of the shear modulus. To account for thermal activation of glide, the functional form presented by Knezevic et al [35] is employed and written as:

$$\tau_\alpha(T) = \tau_{ref} \exp\left(-\frac{T - T_{ref}}{B_\alpha}\right) \tag{5.2}$$

where τ_α is the CRSS at temperature, T, τ_{ref} is the CRSS at the reference temperature, T_{ref}, and B_α is a fitting parameter. In the current study, T_{ref} was considered 295 K for all the slip modes, and the B term for each slip system came directly from Knezevic et al. The reference CRSS values were based upon a prior study which was employed with slight adjustment to account for lot-to-lot variations, primarily associated with annealing [31]. Values for the rest of the parameters are presented in Table 5.1.

The hardening behavior depends directly on the dislocation density and more sophisticated

models have been developed to predict the hardening behavior based on dislocation density, e.g. [35]. The shifts in shear modulus were subtle compared to the observed changes in strain hardening rates. Thus, dynamic recovery serves as the primary explanation. At higher temperatures there is more recovery, so the strain hardening rate decreases with temperature. The linear hardening rate for the roof and chimney mode were empirically fit, and the linear hardening rates for the floor and wall modes were scaled by the shift in shear modulus, which Knezevic et al. reported a functional form [35] for the relevant directions. Linear hardening rates were calibrated to the room temperature data with the CRSS values. Next, using the CRSS values coming from values fitted at room temperature and the known temperature sensitivities, the hardening rates were adjusted for the two harder modes, roof and chimney, for the data collected at 150 ^{o}C. The two hard modes were not adjusted, because they were already fairly low in comparison and did not drastically affect the predicted macroscopic response. Once fitted, the values for the 100 ^{o}C were linearly interpolated between the values for the room temperature and 150 ^{o}C values because the temperature range is narrow. A complete list of parameters is provided in Table 5.1.

Table 5.1: Parameters used in EPSC modeling, the three values of θ for the roof and chimney model correspond to RT/ 100 ^{o}C/ 150 ^{o}C

Mode	τ_{ref} (MPa)	B (K)	θ (MPa)
wall	15	250	50
floor	90	230	50
roof	200	1000	400/ 220/100
chimney	150	160	200/ 110 /50
{130}	90	-	5
{172}	325	-	150

5.3   Results and Discussion

In Figure 5.2, the measured and predicted stress-strain response is shown for the three in-situ RD compression tests. As is typically seen in metals, the flow stresses decrease as temperature is increased. Additionally, the strain hardening rate decreases to a low slope of around 980 MPa at 150 ^{o}C, while at room temperature the slope is around 3,000 MPa. At 100 ^{o}C, hardens at an intermediate rate around 1,800 MPa is observed, so the transition appears to be gradual over this temperature range. It is seen that the model is able to capture both the drop in flow stress (based on the temperature dependence of Knezevic et al [35]), and the shift in hardening behavior (based on an empirical fit of the linear hardening parameters for the roof and chimney modes).
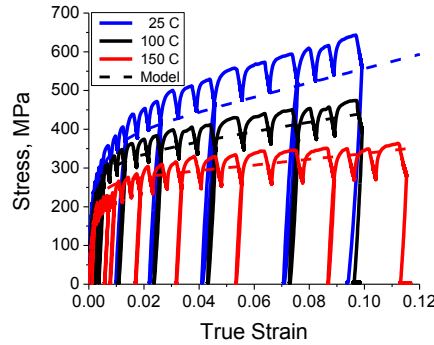
Figure 5.2: Stress-strain response from compressive loading along the RD at 3 different temperatures on SMARTS

Figure 5.3 shows the measured and predicted internal strain evolutions for cases which account for and neglect thermal residual stresses, respectively. It is seen that the internal strain predictions change greatly with the inclusion of thermal residual stresses even as temperatures increase, which lower the internal residual stress state. At all temperatures, the (002) oriented grains, meaning the grains with an (002) axis parallel to the loading axis, have the highest level of internal strain. As a result, they appear to be the hardest. More interestingly, at room

temperature the (200) oriented grains are stronger than the (040) grains, but as temperature increases, the (040) grains appear harder than the (200) grains. This is explained by a Schmid analysis and the thermal residual stress state. Based on Schmid factors, the (040) grains are well oriented for {130} twin during compression, while the (200) grains are well suited for chimney or wall slip. The slip modes soften with temperature, while it is typically seen that resistance to twinning mode behave athermally. The resistance to twinning can decrease with temperature in single crystalline α-uranium for the $\{\bar{1}30\}$ mode, if only slightly compared to the shifts seen in the slip [2].
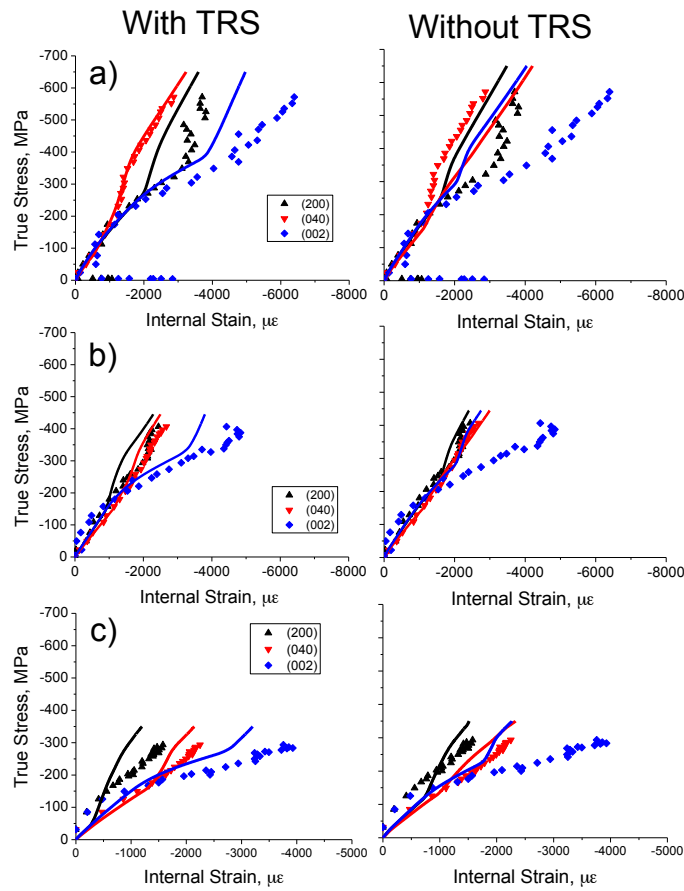
Figure 5.3: Comparison of the predicted (lines) and measured (symbols) internal strain evolutions for the (a) room temperature , (b)100 ^{o}C, and (c)150 ^{o}C experiments that account for thermal residual stresses (left) and neglect thermal residual stresses (right)

The thermal stresses for the {020} direction are compressive, since the thermal expansion along the {020} is far lower than what is expected of the polycrystal in all directions, especially the normal direction which has the largest thermal expansion coefficient. As the sample is heated the thermal stresses are relaxed relaxed, so the tensile strains along the {020} direction become less compressive, and strains along the {200} and {002} would become less tensile. Since the sample is being compressed, the reduction of compressive stress due to thermal mismatch, makes the {040} oriented grains appear stronger as temperature is increased. Figure 5.4 shows a comparison of the measured and predicted strains in the {040} oriented grains. It is seen that by capturing the thermal residual stresses, the model is able to qualitatively predict the increasing strength of the {040} grains without increasing the resistance to twinning.
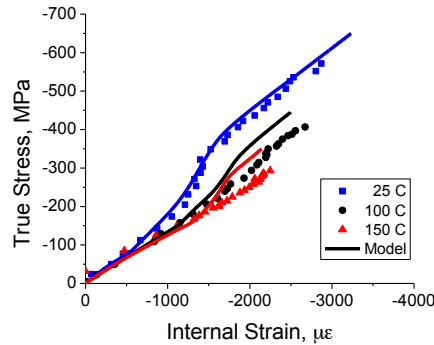
Figure 5.4: Comparison of the predicted (lines) and measured (symbols) internal strain evolutions along the (040) direction at room temperature (blue) , 100 ^{o}C (black) , and 150 ^{o}C (red) experiments that account for thermal residual stresses

Large shifts in normalized peak intensity are indications of deformation twinning, since the intensity is proportional to the volume of material in the diffraction condition. Normalized in this context, means normalized by the initial intensity. Figure 5.5 shows a plot of the relative diffraction peak intensities during deformation. The {040} grains are well oriented for {130} twinning during compression, so the drastic shift in peak intensity correlates to the onset of {130} twinning in this set of grains. The {131} and {021} oriented grains are not well suited for

this twin mode, but rather the less prevalent {172} twin mode. A simultaneous rise in intensity occurs in the {110} peak along with a drop in {131} and {021} intensities. At room temperature and 100 ^{o}C, the {110} orientation only gains volume fraction during loading. However, at 150 ^{o}C the {110} diffraction peak first loses intensity then starts to gain intensity. The {110} grains are well orientated to twin by the {130} mode, but at the lower temperatures it does not activate prior to the onset of twinning in the {131} and {021} oriented grains, which appear to give volume into the {110} diffraction condition.
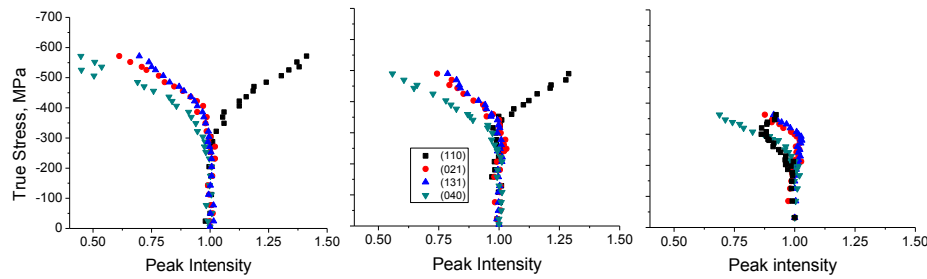
Figure 5.5: Plot of the normalized peak intensity along the loading direction indicating shifts in orientation due to deformation twinning.

Absolute determination of the prior orientation of the new volume fraction is not possible with the current diffraction experiment. However, it is possible to identify potential orientation relationships between two grain sets by comparing the angle between the diffracting plane normal and the twinning rotation axis.[2] A twin and parent have a shared axis that corresponds to the rotation axis, and this axis must have the same relationship to the diffraction vector for the possibility of shifting from one diffraction condition to another through twinning. If the angle between the diffraction vector and the rotation vector is constant between two grains sets, then activation of the twin mode explains the shift in intensity from one orientation to the other. However, it is possible to eliminate twinning connections between grain sets when the angle

---

[2]{172} is a type I twin, which corresponds to a 180° rotation about the shear direction, and the {130} is a compound twin so the transformation is equivalent to 180° about either the twin plane normal or twin shear direction.

between the rotation axes do not have a common angle between two *hkl*'s with absolute certainty. Table 5.2 lists the angle between the relevant diffraction plane normals and the twinning rotation axis. It is seen that there are some similar angles between the $\langle 3\bar{1}2 \rangle$ vectors and the diffraction peaks as well as some of the $\langle 3\bar{1}0 \rangle$. Since the {130} twin is a compound twin, so both the shear direction and the plane normal must have similar angles between variants with the diffraction vectors. As such, it is seen that the (110) direction has a similar angle with the $\langle 3\bar{1}0 \rangle$ direction for the second variant as the (021). This is not a possible connection because the twin normals do not coincide. As such, the {130} mode would not connect any peak shifts between these diffraction peaks.

Table 5.2: Angles between the diffraction vectors and the twinning rotation vectors for the two twin modes

Peak	$\langle 3\bar{1}2 \rangle$				$\langle 3\bar{1}0 \rangle$		{130}	
	variant 1	2	3	4	1	2	1	2
(110)	44	69	69	44	8	60	30	70
(131)	31	78	78	65	28	90	18	70
(021)	45	90	45	90	61	61	45	45

The {040} oriented grains are known to twin by the {130} mode drop and decrease in peak intensity from EBSD measurements [1], but there is not a corresponding increase in the intensity of any of the other peaks monitored as the resulting twins would not be in a diffraction condition. In contrast, the onset of {172} twinning, which is considered a secondary mode [1], in the grains closely oriented to {131} or {021} diffracting conditions could cause an increase in the {110} or {112} intensity. The simultaneous intensity drop and rise at all three temperatures suggests that the {131} and {021} oriented grains drop intensity due to {172} twinning, and the corresponding twins contribute to {110} or {112} diffraction peak intensity. The {110} represents roughly 1 % of the volume fraction while the {131} and {021} peaks represent 5 % and 3% respectively. As such, twinning in the initially oriented {110} would not necessarily be seen in such a plot. The shifts in internal residual stresses are believed to cause the onset

of twinning in {110} grains before twinning in {131} grains at the higher temperature, while at room temperature, the twinning in the {131} grains occur first. Post-deformation EBSD studies have revealed the dominance of {130} twinning [1]. However, the study was conducted on unloaded samples, so it is possible detwinning occurred during the unload.

EPSC modeling allows for the estimation of relative contributions of the different deformation modes. To compute relative activity, the shear strain for each mode is volume averaged and divided by total shear (sum of averages of the modes). As such, a high activity does not necessarily mean large amounts of strains are accommodated. For instance, the wall mode activates early in the deformation when only small levels of plastic strain are present, so the overall plastic strain contribution of this mode is small. Additionally, when analyzed with the internal strain evolution, the relative activities help to identify the cause of yield in different grain sets. In all of the simulations, the yield in the {040} oriented grains coincided with the onset of the {130} twin mode. The activities show a decrease in twin activity and an increase in slip activity as temperature increases, which is to be expected with the thermally activated nature of slip and near thermal character of twinning in the temperature range of interest [2]. The model predicts a shift in the order of activation of the slip modes, as chimney softens much more at these mildly elevated temperatures than the roof mode [35]. At room temperature, the chimney mode activates after the roof mode, despite having a lower CRSS due to the thermal residual stresses. In all of the simulations, the roof and floor modes activate simultaneously. This is required for macroscopic flow, but activation of the roof mode corresponds to inflection in the internal strain evolution of the {002} grains, which is not seen at higher stress levels in the experiment. This shortcoming is likely a result of uncertainty in the thermal residual stress predictions. Notably, the current model [30] permits relaxation by crystallographic slip whereas, recent evidence points to more isotropic diffusional flow mechanisms as the primary mode of internal stress relaxation.

The crystallographic texture of each specimen was measured after the heating, mechanical

deformation and subsequent cooling for the sample tested at room temperature and 150 ^{o}C. The current EPSC model allows for prediction of the texture evolution due to twinning during deformation. Figure 5.6 shows the measured and predicted pole figures for samples. At room temperature, RD compression results in large twinning volume fractions at room temperature, as previously seen [1], and results in large changes in pole figures after deformation. A large shift in texture was observed and simulated. The model over predicts the texture evolution, which suggests that the model over estimates the activity of twinning, mainly the {130} mode, as all of the (010) intensity is lost along the rolling direction during room temperature deformation. At higher temperatures, the texture evolves much less in both the measured and simulated. As the temperature increases, the slip modes become softer, and deformation twinning contributes much less to the overall plastic deformation. As such, the texture evolution is less in the samples deformed at 150 ^{o}C.

5.4 Conclusions

This work combines neutron diffraction experiments on SMARTS with polycrystalline thermo-elastic-plastic modeling to arrive upon the following conclusions:

- During RD compression loading, depleted α-uranium softens with increasing temperature both in terms of yield strength and strain hardening rate.

- Predicting the internal strain evolution measured through diffraction requires accounting for thermal residual stress. As such, determining the relative mode strengths and effects through polycrystalline plasticity modeling requires for proper accounting of the thermal stresses.

- The model was able to predict the rank order of the internal strains, and macroscopic flow curves by employing a previously generated model for thermal residual stresses, as
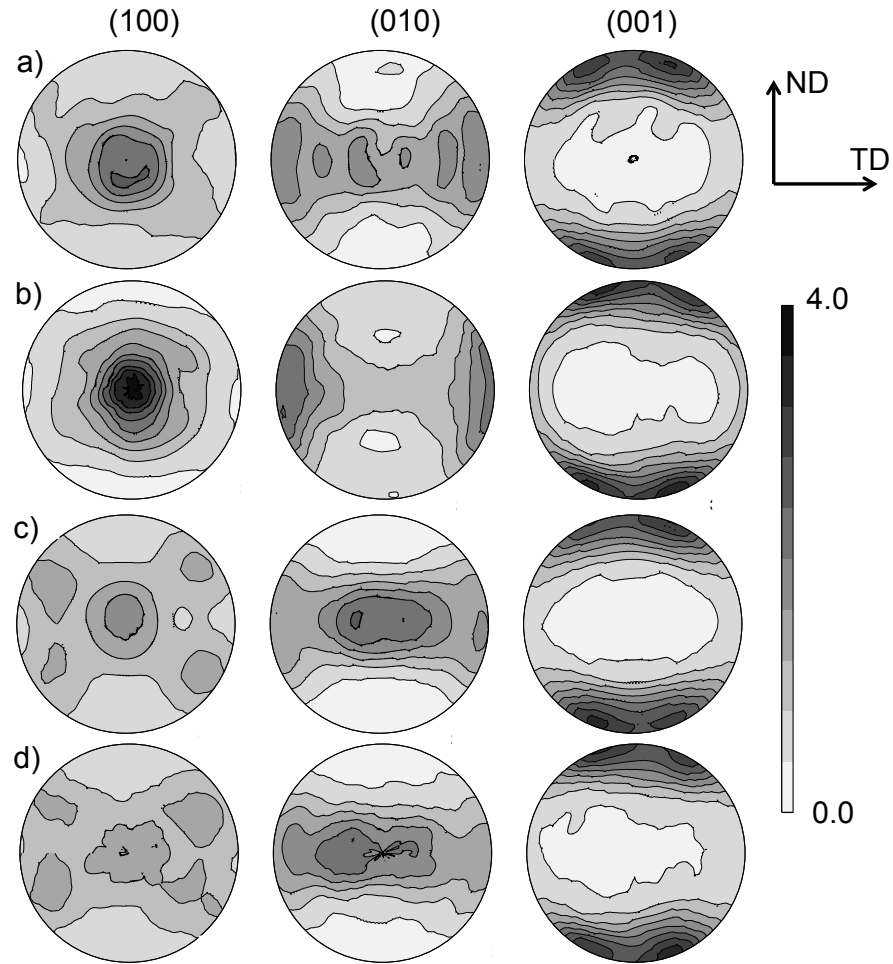
Figure 5.6: Measured and predicted post deformation textures: (a) measured after 9.5 % strain at room temperature, (b) Predicted after 12% strain at room temperature, (c) measured after 11% strain 150 ^{o}C, (d) predicted after 12 % strain at 150 ^{o}C

well as temperature sensitivities of the slip and twinning modes previously determined using a VPSC model.

- The grains which are relaxed due to twin propagation (mainly {040} along loading direction) exhibit an apparent increase in strength with increasing temperature, which is explained by a change in residual stress during heating to the test temperature.

- The {110} peaks gain intensity during loading at room temperature and 100 ^{o}C, but drop intensity before increasing at 150 ^{o}C. Again, this result can be explained in terms of changes in thermal stress states induced by heating to the test temperature.

- The drop {021} and {131} intensity and simultaneous increase in {110} and {112} intensity are revealed to indicate the activation of the secondary {172} twinning in the {021} and {131} grains.

- Due to increased slip and decreased twinning, the texture evolves to a lesser extent at higher temperatures when compressing along the rolling direction, as evidenced by the model and measured pole figures.

Chapter 6

In-situ Characterization of Thermal Ratcheting

C.A. Calhoun, K. An, E. Garlea, and S.R. Agnew

This chapter presents the results from a series of experiments that were initially aimed at studying thermal ratcheting. During the course of the study, it was seen that the previously believed to be annealed material actually underwent an apparent recrystallization. Additionally, the diffraction spectra exhibited some unique phenomena from a crystallography perspective. As such, this chapter's main goal is to look at the residual stress development during thermal cycling and discuss potential mechanisms for that deformation, but discussion of the apparent recrystallization and the unique response seen in the diffraction spectra are also included.

6.1   Introduction

Textured polycrystalline α-uranium is known to thermally ratchet when subjected to repeated thermal cycles [14, 15, 16, 17, 18]. Thermal ratcheting is characterized by the shape evolution of a polycrystal after repeated cycling. For example, an extruded bar of α-uranium will

lengthen after being heated and cooled to its initial temperature and will continue to lengthen upon subsequent cycling. Simultaneously, the diameter of the bar will decrease with thermal cycling in a volume conserving fashion. The driving force for thermal ratcheting is well known and comes from the anisotropy in the single crystal thermal expansion behavior. This anisotropy leads to the development of large mismatch strains upon a temperature change in a polycrystal. The mismatch strains are initially accommodated elastically, but achieve sufficient stresses to induce plastic strains [30]. Ratcheting has been studied a number of times predominately in the 50's and 60's [14, 15, 16, 17, 18]. The most extensive experimental work on the subject was done by Chiswick [14], who examined the effects of grain size and texture strength on macroscopic ratcheting. It was seen that the ratcheting increased with the number of thermal cycles (up to 3000 cycles, the maximum number of cycles performed on one sample), the strength of the texture, and reducing grain size. The largest strains reported for the study of texture and grain size were on the order of 10 % after around 500 cycles on the small grain, strongly textured sample, but Chiswick reported that a high-purity sample grew 5 times its original length after 3000 thermal cycles with no void formation. Another study also observed the formation of voids due to thermal cycling [18], while other works on thermal ratcheting do not report any evidence of pore formation during cycling [15, 16, 17]. Chiswick concluded that the voids formed during thermal cycling are due to the presence of impurities [14]. As such, it is speculated the latter studies had lower impurity content or the researchers did not know or did not draw attention to the impurity level. Chiswick also reported subgrains appeared with repeated cycling in the larger grained samples, but it was not as pronounced in the smaller grained samples.

One key consideration when analyzing any deformation process is understanding the potential deformation mechanisms. As has been shown in the previous chapters, glide and twin based deformation of α-uranium exhibits strong anisotropy, which includes 4 slip modes and two slip systems. Deformation by glide and twinning are the controlling mechanisms under

conditions of high stress and strain rates. At lower stress and strain rates, other thermally ac-
tivated deformation mechanisms can come into play, especially at higher temperatures. These
mechanisms are thought of as creep mechanisms and are known to be highly rate sensitive. The
main mechanisms in the creep regime are broadly categorized as dislocation-, and diffusion-
based creep. The two main mechanisms for diffusion-creep are Coble and Navarro-Herring
creep. Both involve mass flow to relax any elastic strains, but Coble creep involves diffusion
along the grain boundaries, and Navarro-Herring creep involves diffusion through the lattice.
There are a few important quantities when considering potential deformation mechanisms: (1)
Homologous temperature, (2) Stress, and (3) Strain rate. As a way to help determine potential
mechanisms, engineers employ deformation maps as pioneered by Ashby. Figure 6.1 shows a
schematic of a typical deformation map.
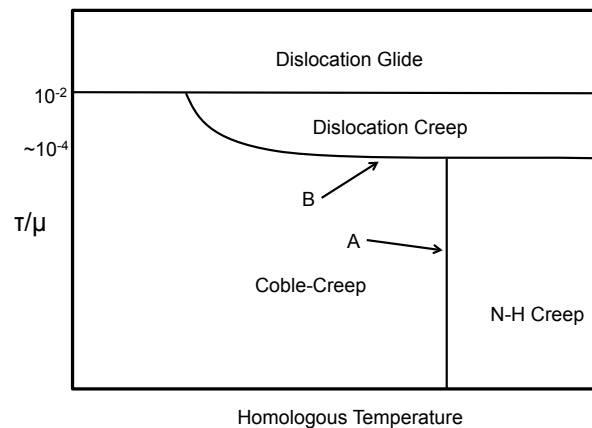
Figure 6.1: Schematic of a deformation map

The transition to dislocation glide is typically seen around normalized stresses around 10^{-2},
and that is the most universal point on this map between materials. This boundary is often
observed as "power-law break down." Depending on the material, the "triple point" where
the boundary for dislocation creep, dislocation glide and Coble-creep occurs at homologous
temperatures between 0.3-0.6. The transition from glide-creep to the Nabarro-Herring creep
depends greatly on the grain size and the material. As grain size is decreased, the transition

occurs at higher stresses. Creep deformation is viewed as a sum of the contributions from all

mechanisms and all of these mechanisms can occur simultaneously, but this map identifies the

dominant mechanism. Estimating the transition from Coble to Nabarro-Herring creep can be

easily determined using diffusion based equations. The steady-state strain rate for Nabarro-

Herring creep is shown in eq. 6.1.

$$\dot{\varepsilon}_{NH} = A_{NH} \left(\frac{D_L}{d^2} \right) \left(\frac{\sigma \Omega}{kT} \right) \tag{6.1}$$

where A_{NH}, D_L, d, σ, Ω, k, and T are a scaling constant (taken to be 10 [70]), the lattice

self-diffusivity, the grain size, a scalar form of the stress state, the atomic volume, Boltzmann's

constant, and temperature, respectively. Fortunately, the self diffusion coefficients have been

determined for α-uranium at temperatures between 580-650 ^{o}C [71], which allows for the de-

termination of the activation energy. Using this, the self diffusion coefficient can be estimated

at all relevant temperatures. Similarly, the equation for strain-rate in Coble creep can be com-

puted using eq. 6.2

$$\dot{\varepsilon}_C = A_C \left(\frac{D_{GB}\delta'}{d^3} \right) \left(\frac{\sigma \Omega}{kT} \right) \tag{6.2}$$

where D_{GB}, δ', and A_C, are the diffusivity along the grain-boundary, the effective grain-

boundary thickness, and a constant that is taken to be $10b$ for this case, respectively. Unfortu-

nately, the grain boundary diffusivity can not be easily determined, so it must be approximated.

Using the same functional form as the lattice diffusion while assuming the activation energy

of vacancy formation along the grain boundary is between 40-60% of energy required in the

lattice, the grain boundary diffusivity is computed. Using these equations, one can estimate

the transition by computing the temperature at which the two strain rates are identical. For 25 μm grain size in α-uranium, the transition is around 550 ^{o}C or higher, close to the upper temperature limit of interest in the present study. Therefore, grain boundary diffusion is more likely to occur in the temperature ranges where thermal ratcheting is observed.

Many of the above studies, which reported ratcheting, focused primarily on the creep behavior and its affects on thermal cycling [15, 16, 17, 18]. Unlike most metals, a cooling and heating cycle in the middle of a creep experiment causes a shift in the deformation rate in deplete α-uranium. Young showed that cooling and returning to temperature while under stress induced a plastic strain during the thermal cycle and essentially reset the creep state of the material [38]. In other words, the sample went through primary creep again upon returning to temperature, as opposed to going straight to steady state creep as would be expected in most other metals, especially pure metals. Creep experiments have reported a stress exponent of ~2.5 [17, 38], which is consistent with a grain boundary sliding mechanism. Grain boundary sliding is often reported to have n=2-3, and solute drag dislocation creep which is reported as n=3. Context favors grain boundary sliding, as the material is nominally pure. Presumably it is possible that interstitial impurities are present in non-negligible amounts.

6.2 Methods

As was done in the previous chapters, clock-rolled plate of α-uranium was used. The rolled plate material underwent the same processing as the material in Ref. [33]. The depleted uranium was initially cast into a 254 mm thick ingot. The ingot was first hot cross-rolled at 640 ^{o}C to 32 mm then warm clock-rolled at 330 ^{o}C to 15 mm before an intermediate anneal of 480 ^{o}C for 2h. Subsequently, the plate was further warm clock-rolled at 330 ^{o}C to 7.6 mm and was reportedly given a final anneal of 550 ^{o}C for 2h, which is likely to not have occurred based on the experimental observations. Two cylindrical samples, d=6.25 mm and L=15.25 mm, were

electro-discharged machined from the annealed plate. Both cylinders were oriented with the transverse direction (TD) along the cylinder direction, which put the RD and ND in the radial directions. The processing left the material with a texture typical of clock-rolling, which is shown in Figure 6.2. The pole figures presented in this work were computed from orientation distribution functions computed using complete diffraction spectra collected on HIPPO in the Lujan center of Los Alamos National Laboratory. More details of the texture measurement can be found in reference [42]. Figure 6.2 shows the texture in the plate initially. It is seen that the texture has a stronger intensity in the {002} pole figure then previously reported in the previous chapters.
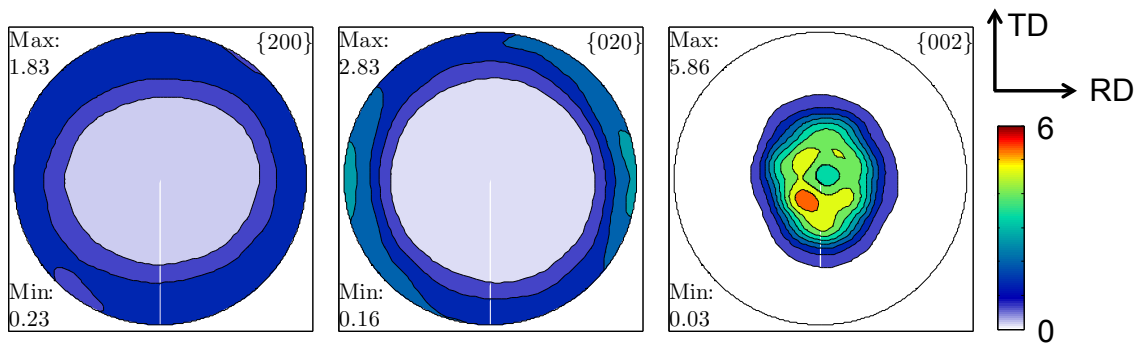
Figure 6.2: Recalculated pole figures for the as-received material

6.2.1   Experimental Techniques

In-situ neutron diffraction experiments allowed for investigation of internal thermo-mechanical strains. For this, the VULCAN beam path at in the Spallation Neutron Source in Oak Ridge National Laboratory was utilized. In this time-of-flight (TOF) instrument, neutron detectors are oriented 90 degrees to a neutron beam coming from a spallation source. A chopper allows for pulses of neutrons with varying energies (speeds) to pass at 20 Hz for the current set of experiments. By knowing the time between the detector and the chopper, the velocity of the neutron can be computed, and through the DeBroglie equation the wave length for the moving

particle is computed.

The samples were placed, one at a time, inside a vacuum furnace in the beam path. Diffraction pattern collection started at the once the vacuum was achieved. The samples were heated to an annealing temperature of 550 ^{o}C and held for 2 hours. They were then cooled to 100 ^{o}C as fast as safely possible, first by pure black body radiation to 200 ^{o}C inside the vacuum then nitrogen was introduced into the furnace and purged in ~5 minute intervals. Upon reaching 100 ^{o}C, the samples were heated back to 550 ^{o}C and immediately cooled back down following the same procedure. In total, each sample was cooled 3 times after being held at 550 ^{o}C for 2 hours. In this study, the first sample was oriented to have the diffraction vectors along the RD and ND, while the second sample was oriented to have the diffraction vectors along the TD and ND. This would allow for sample to sample comparison by comparing the strains along the ND as well as gather information about the RD and TD. The samples were heated at a constant rate of 5.1 ^{o}C/min, and cooled at the fasted rate possible. The cooling rate was not constant but averaged to be 2.7 ^{o}C/min. A complete temperature history for the samples is shown in Figure 6.3.
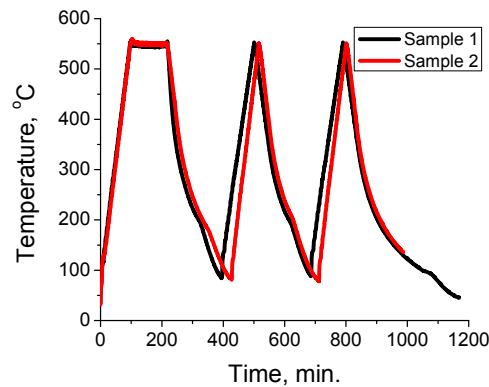
Figure 6.3: Plot of the temperature history for sample 1 and 2

After completion of the test, the neutron diffraction data was binned into 5 minute intervals. As such, it is assumed that the diffraction pattern represents the average pattern over this time

interval. Within each pattern, the peak positions were fitted using the single peak fit in GSAS

through the VDRIVE interface. The intensity of each peak was also fitted, and normalized by

the proton charge, which is a measure of the beam intensity. The intensity changes provide

indications of recrystallization, deformation twinning and texture evolution.

To compute lattice strains, which are comprised of the thermal and elastic strains, as was

the case in Chapter 2, single peak fits were conducted on the individual peaks. Not all of the

diffraction peaks can be fitted due to overlap at the high temperature. To compute the lattice

strain, the same method as presented in chapters 2-5 was employed, which is given by eq. 6.3.

$$\varepsilon_t^{hkl} = \frac{d^{hkl} - d_o^{hkl}}{d_o^{hkl}} \tag{6.3}$$

To compute the mechanical strain, the thermal strain was subtracted using eq. 6.4. This same

method is used in Chapter 2, and the functional forms for α are reported in that chapter.

$$\varepsilon_e^{hkl} = \varepsilon_t^{hkl} - \int \alpha_{hkl}(T)dT \tag{6.4}$$

The resulting mechanical strains were compared to thermo-elastic self-consistent predic-

tions of strains, which was also done in Chapter 2. In the simulation, the temperature de-

pendence of the thermo-elastic properties was incorporated. This comparison allows for the

identification of any potential plastic relaxation mechanisms as a break from this curve is ev-

idence of plastic relaxation. As will be seen, there was a change in texture during the initial

annealing, so for this calculation the texture came from the same annealed texture as used in

Chapter 2.

6.3   Results and Discussion

The results are divided into two phases: (1) initial heating and annealing and (2) thermal cycling.

6.3.1   Annealing

The researchers suspected the sample was not fully annealed based on mechanical behavior in non-published experiments and the strong texture in samples that were cut from the same plate. The sample was heated for ~80 minutes to achieve the temperature (550 ^{o}C) and held for 120 minutes. Figure 6.4 shows the evolution of the diffraction pattern for the ND and TD monitored through the initial heating and hold at 550 ^{o}C. In these spectra, the background is removed based on a calibration vanadium sample, and the total intensity (summation of all the counts) is normalized by the proton charge to allow for absolute comparison between collection periods. Any changes in intensity of a given peak is predominately due to volume fraction reorientation (i.e. texture evolution). Along the ND, the most distinct peak intensity change is seen in the {002} peak, which drops in intensity significantly. The two peaks which gain intensity are the {111} and {122}. The peak intensity changes occur when the sample reaches 550 ^{o}C, and do not change significantly thereafter. Recrystallization of clock rolled plates have been reported to achieve 90% within 17 minutes at 475 ^{o}C [72]. Since sample was above that temperature for more then 15 minutes to achieve 550 ^{o}C and increasing temperature accelerates the recrystallization, it seems reasonable to assume that all of the changes in intensity are due to recrystallization. This suggests that the reported anneal may have happened at an intermediate step in the clock rolling process, rather then after the final pass through the rollers. The exact deformation history, which is unknown for the sample in the current study, affects the rate of recrystallization, so the exact kinetics cannot be determined or predicted and may vary from those reported in the literature.
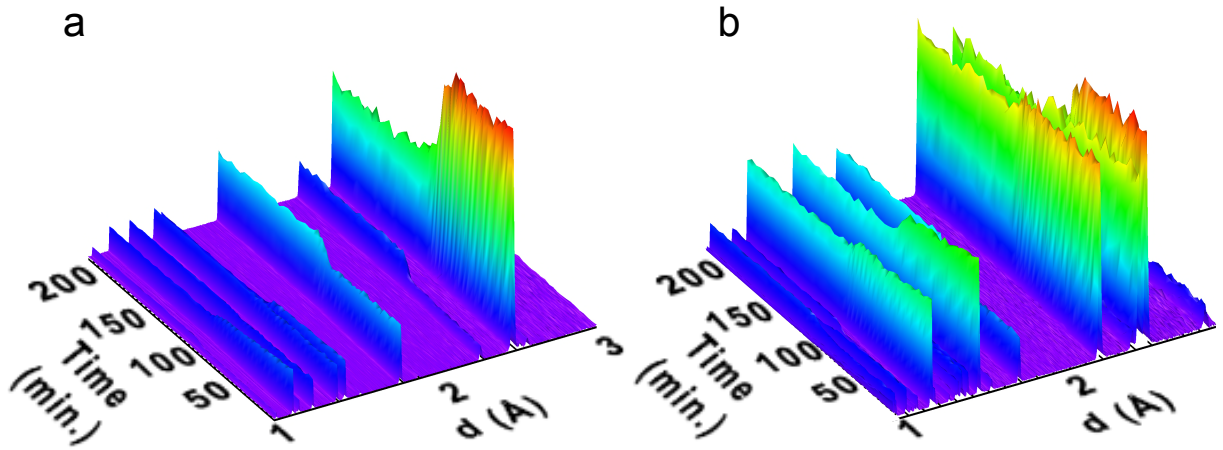
Figure 6.4: 3D projection of the evolution during the initial heating and anneal along the (a) ND and (b) TD

To more clearly show the changes in diffraction intensity, the diffraction spectra at 100^oC were compared between the initial heating, and two subsequent cycles. Figure 6.5 shows the diffraction spectra from the ND direction for three points. A clear difference is seen between the first and the second time, but little to no changes are observed between the second and third pattern, which provides even more evidence that the sample was not annealed after rolling, as the thermal cycling does not provide sufficient deformation to cause the drastic peak changes seen during the initial heating. The {002} peak is highlighted in the figure with a black arrow. It is seen that there is a decrease in this peak intensity while the other peaks gain in intensity by comparing the relative intensities of the largest peak to the smaller peaks.

Figure 6.6 presents the diffraction pattern for the TD sample taken during the initial heat up and after one cool. In this, the {131} peak drops in intensity, shown with the black arrow. The {112} peak increases drastically, which is highlighted by the red arrow. The blue arrow shows the region of 5 peaks discussed along the RD. The {040}, {200}, and {041} do not change in intensity during the anneal, while the {023} peak develops into a strong shoulder on the {200} peak. The {113} peak also grows and nearly doubles in size. All of these $in-situ$ observations
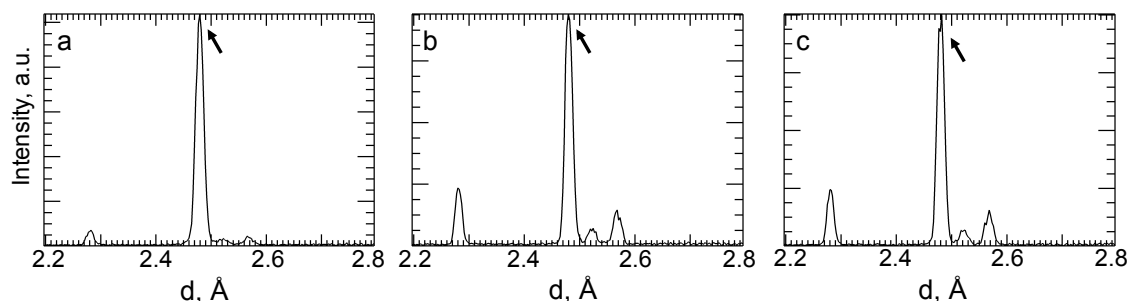
Figure 6.5: Diffraction spectra collected along ND at 100 ^{o}C comparing the pattern during (a) initial heating and (b) after 1st cool. Highlighting the {002} diffraction peak

of intensity changes are consistent with comparisons of the recalculated pole figures measured *ex − situ*.
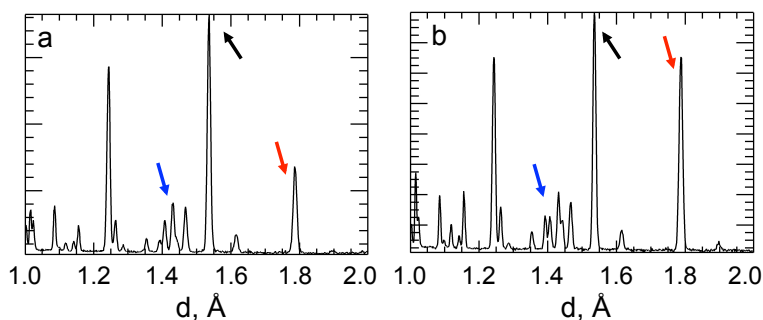
Figure 6.6: Diffraction spectra collected along TD at 100 ^{o}C comparing the pattern during (a) initial heating, (b) after 1st cool and (c) after the second cooling.

To further illustrate the affect of the anneal on the diffraction intensity of the {002} peak, the pole figure for this sample and an annealed sample from the hydrogen embrittlement study reported in Chapters 3 and 4 are compared in figure 6.7. Samples from that study were cut from the same plate at the same time as the samples used for this study, but were then annealed after cutting at a slightly higher temperature of 630 ^{o}C for 3 hours. Figure 6.7 shows a comparison of the recalculated {002} pole figure before and after the anneal at 630 ^{o}C. A strong effect is observed in this pole figure, where as the other pole figures showed more subtle changes in intensity.
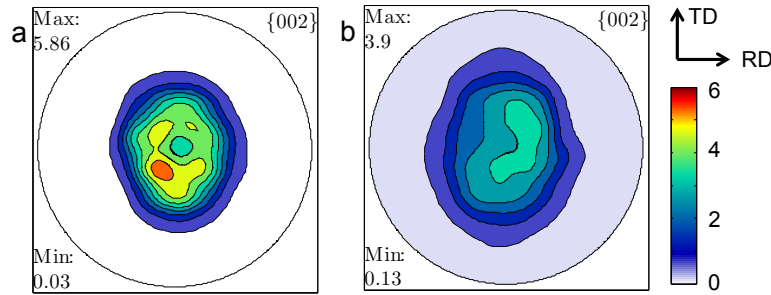
Figure 6.7: Comparison of the recalculated {002} pole figure for the (a) as received pole and (b) annealed sample reported in chapters 3 and 4.

6.3.2 Thermal Cycling

Figure 6.8 presents the contour plot of the diffraction spectra for the RD and ND directions through one thermal cycle. In other words, this is a top down view of the diffraction pattern through one cycle. It is seen that some peaks seem are stationary through one cycle while others shift to higher d-spacings, and others shift to lower d-spading. In a typical isotropic material, all of these peaks would shift proportionally to higher d-spacing with increasing temperature, because the strain would be uniform in all directions. The lattice spacings would undergo the same strain levels. In α-uranium, the CTE is anisotropic, so the peak shifting is not uniform. Most interestingly, some peaks merge into each other at higher temperatures. Some of these peaks are highlighted by the orange dashed boxes. Between the RD and ND, there are drastic differences due to texture. For example, the {020} peak appears, ~2.9 angstroms, in the RD spectra, but is not seen in ND. The nearly immobile peak seen strongly in the RD and faintly in the ND around 2.5 angstroms corresponds to the {021} peak, which has a CTE close to zero, so the peak position does not change. The peak with a slightly lower lattice spacing corresponds to the {002}, which is strongly textured.

Figure 6.9 shows a comparison of the diffraction spectra along the RD between the lower temperature ~100 ^{o}C and the higher temperature, 550 ^{o}C, in the neighborhood of the {002}, {021}, and {110} (increasing lattice spacing) along the RD. At the low temperature, three clear
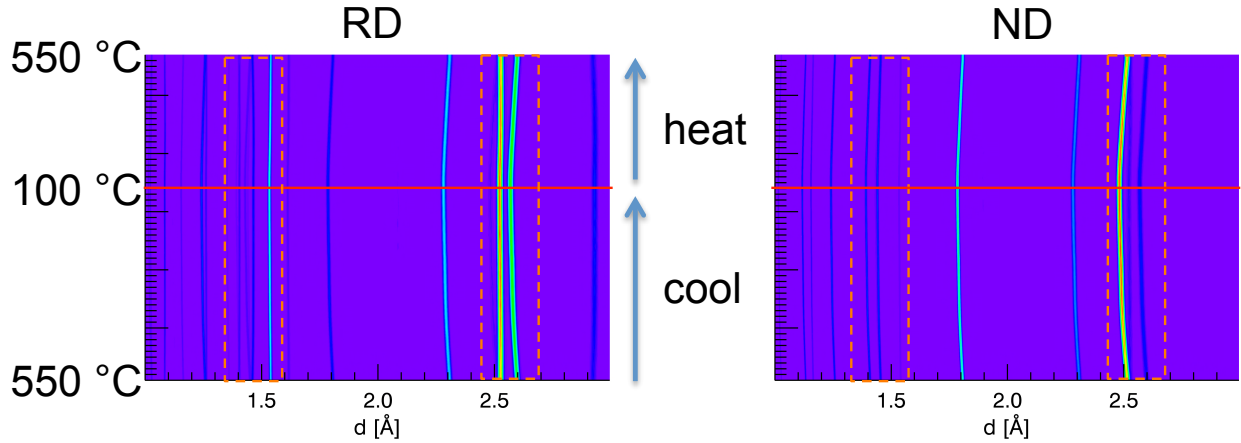
Figure 6.8: Contour plot of the diffraction pattern during one thermal cycle for the RD and ND directions. Highlighted are: the low temperature point of 89 ^{o}C with a red line and the regions where peaks merge into each other at higher temperatures with dashed orange lines

peaks are seen. At the higher temperature, the thermal expansion has shifted the {002} to coincide with the {021} peak. It is seen that the location of the {021} peak remains nearly identical between the two temperatures, while the {002} and {110} peaks increase lattice spacing with temperature.
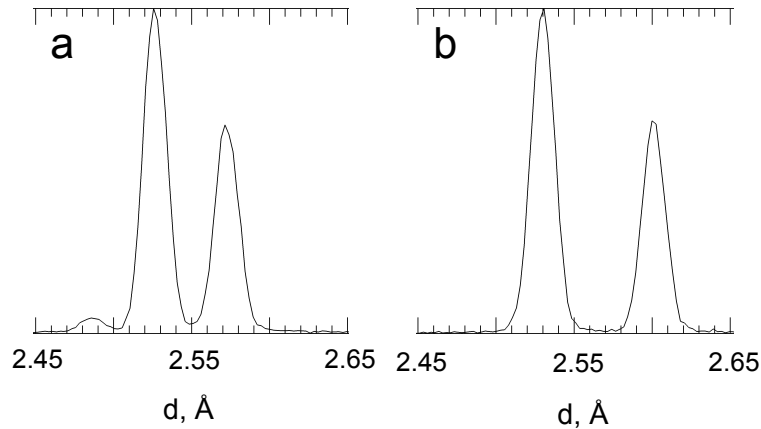
Figure 6.9: Comparison of the diffracted spectra between 2.45-2.65 Angstroms along the RD (a) after cooling to 100 ^{o}C and (b) at 550 ^{o}C showing the {002}, {021}, and {110} in ascending planar spacing

Figure 6.10 shows a side by side view of the diffraction spectra along the rolling direction at

100 ^{o}C and 550 ^{o}C. At the lower temperature, there are 7 distinct peaks in the spectra, and one of those is a spurious peak coming from the MgO that held the sample, which is highlighted by the red arrow, due to thermal expansion slight shifts in sample positioning. The rest of the peaks are labeled for their associated *hkl*. At the higher temperature, there are only 3 distinct peaks seen in the spectra, one of which has a slight shoulder. The {113} and the {041} peaks come together and at the higher temperature they appear as only one peak. The {200} and {023} peaks come together into a distinct peak and also start to merge with the {040} peak. If the temperature were to increase slightly higher, it is speculated that this these 3 peaks will all over lap. It is also seen that the position of all the peaks increase in spacing due to thermal expansion aside from the {040}, which decreases due to the negative thermal expansion.
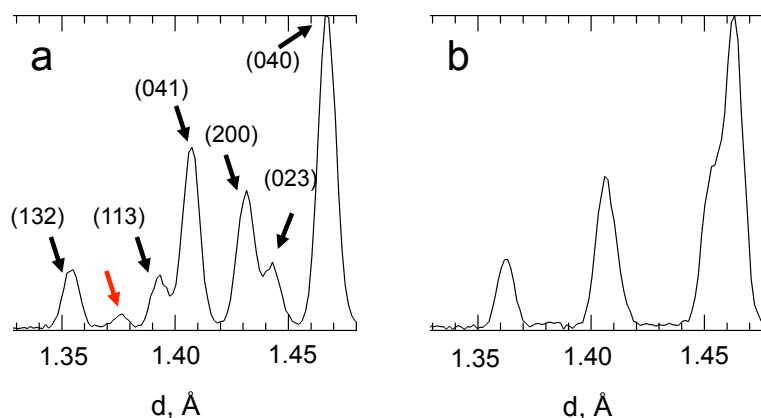
Figure 6.10: Comparison of the diffracted spectra between 1.33-1.47 Angstroms along the RD (a) after cooling to 100 ^{o}C and (b) at 550 ^{o}C. Highlighted is a spurious peak originating from the MgO crucible that held the sample.

A recent study by Monroe et al. on martensitic phase transformations identified a relationship between the directions of negative CTE in the low temperature martensite phase and their corresponding directions in their higher temperature austenite phase [29]. The authors identified a transformation between the principle axis directions between the austenite and martensite phase transformation for a variety of materials. Additionally, they viewed the allotropic α-uranium transformation in a pseudo martensitic transformation between the cubic,

γ, and orthorhombic, α phase, since α phase closely resembles a shear version of the γ phase. The authors also ignored the β phase, which does not share a shear relationship with the other phases. In their paper, it was assumed the [100] of the α phase corresponds to the [100] of the γ while the [010] and [001] correspond to the $\langle 110 \rangle$ directions in the γ. However, in an older paper [73], it was proposed that the [100], [010], and [001] correspond to the $\langle 111 \rangle$, $\langle 112 \rangle$ and $\langle 110 \rangle$, respectively. By doing the transformation and computing the lattice spacing on the resulting lattice plane, they showed that the CTE expands the lattice parameter to correspond to the higher temperature phase along the principle directions. In other words, the crystal structure in α migrates toward the higher temperature cubic γ phase, but the β phase eliminates a direct measure of the continuous transition. For example, the {020}, lattice spacing around 2.93 angstroms in α corresponds to the [0 0.85 0.85] in the cubic system which has a planar spacing of 2.92. This same logic extends to all three of the principle directions, and holds true for all crystallographic planes monitored. In all cases, the planes tend toward the lattice spacing of the higher temperature γ, and the amount of the shifts in d-spacing seem to correspond the difference between the two lattice spacings.

The lattice spacing of the {021} in α is almost exactly that of the corresponding γ {110}, so it does not shift during thermal cycling. The {002} is seen to have a large difference between its actual and corresponding lattice spacing and has a much large shift with temperature. Despite the differences in transformation, it is seen that the lattice spacings of their corresponding directions. One key difference is that the {002} and {021} correspond to the same vector in γ, {110} type, and converge upon this exact lattice spacing if the transformation reported by Hatt [73] but not for transformation reported by Monroe [29]. Additionally, the {040} and {023} tended toward the spacing of the {112} peak, which is the shared corresponding lattice direction in the γ. The {113} and {041} do not share an equivalent cubic diffraction vector with either transformation, but were seen to form together. The {040} and {023} do share a cubic equivalent and merge together. However, the same is not true with {200}, which is observed

to connect with the other two. As such, the cubic equivalent with the the gamma peaks do not completely explain the merging of lattice spacings. However, neither transformation predicts all the over lapping peaks in α-uranium higher temperatures to correspond to the same *hkl* in the γ. The tetragonal β phase was considered, but a similar relationship between the α and the β could not be determined.

Internal Strain Evolution

The overall internal strains were computed as described in the methods section. Figure 6.11 shows a comparison of the lattice strains computed using pure thermal expansion (without elastic deformation) and those measured during the experiments assuming that the material has no internal stress at the annealing temperature of 550 ^{o}C. It is clearly seen that there is a strong anisotropy in the internal strains, and the overall strain states follow the thermal expansion strains pretty closely, although some hysteresis is seen, especially in the {020} strains along along the RD direction. The strains along the TD are close to the predicted thermal strains. Thus, it is clearly seen that a majority of the internal strains are comprised of thermal strains, and their magnitude does not necessarily correlate to the stress state, which is of key interest to explain the ratcheting mechanism.

As the thermal strains are so large and are independent of the stress state, they can be subtracted from the total strains to yield the mechanical strains. Figure 6.12 shows a comparison of all of the mechanical strains through one thermal cycle. It is seen that the overall strain levels are really low, with a maximum of only 1000 $\mu\varepsilon$. During a uni-axial tension or compression curves (in Chapters 3-5), internal elastic strains are seen to reach nearly 10,000 $\mu\varepsilon$. This is a strong indication that significant plastic relaxation occurs. Some of the strains show a strong hysteresis that was not clear in the overall strains, mainly the {111} and {112} strains.

Figure 6.13 shows a comparison of the {020} strain evolution along the rolling direction between the first and second cooling and heating cycles. The same reference point was used
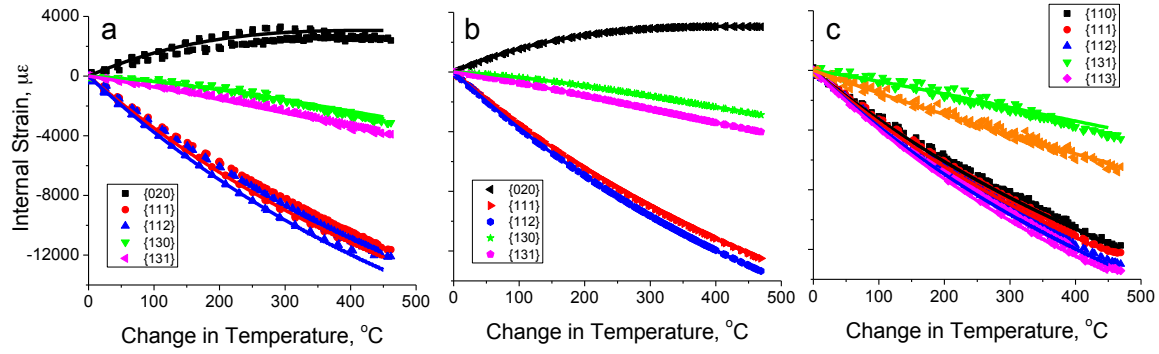
Figure 6.11: Comparison of the measured total (elastic+thermal) internal strain evolution with the thermal strains coming from CTE properties for all of the peaks measured along: (a) RD, (b) TD, and (c) ND.
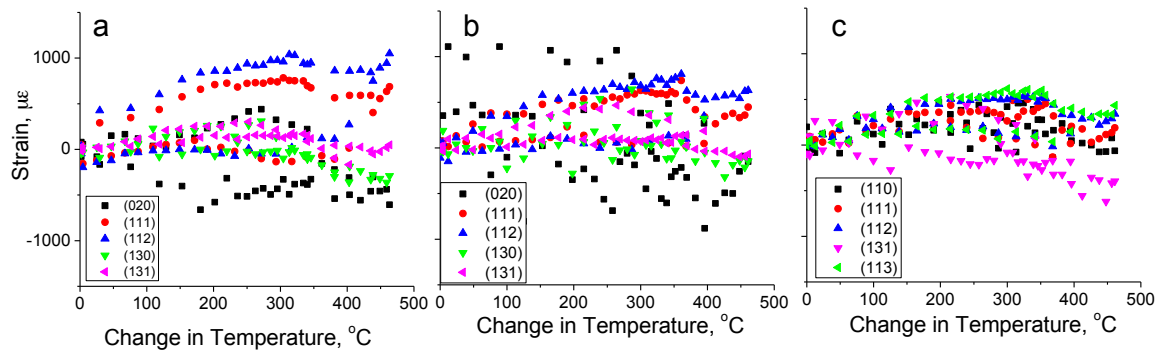
Figure 6.12: Comparison of the mechanical internal strain evolution for all of the peaks monitored along: (a) RD, (b) TD, and (c) ND.

for each of the samples, meaning both employed the same method to determine the d_o values. Upon cooling, the {020} strains become compressive, but reach a plateau maximum -750 $\mu\varepsilon$ after cooling 200 ^{o}C (or to ~ 350 ^{o}C), and does not continue to develop as cooling is continued. Upon heating, the strains seem to reverse and reach this same plateau around 500 $\mu\varepsilon$ before relaxing back to zero at the high temperature. This asymmetry might be real, but 250 $\mu\varepsilon$ in the mechanical strain is quite small compared to the magnitude of the overall lattice strains observed and the uncertainty in strain is roughly 250 $\mu\varepsilon$ for the total strain and even greater due to the approximations of the CTE. The cooling strain development is consistent with that of Chapter 2, but in that study there was not sufficient time to chart the heating. In the case of cyclic plasticity, it would be expected that upon reversal a residual stress would be developed and the elastic strain would not return to zero after a complete reversal, but some sort of high temperature relaxation is taking place. It is also seen that the strain evolution is nearly identical between the two cycles, despite one coming after a 2 hour anneal and the other directly after a heating then cooling, which further validates this is zero stress state.
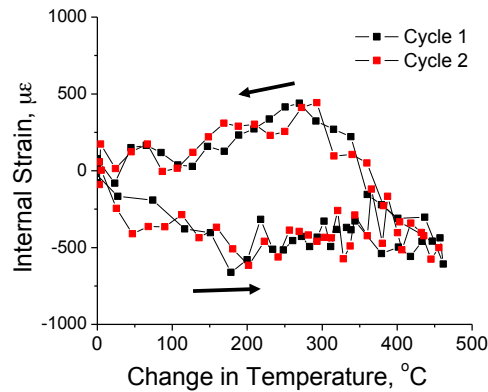
Figure 6.13: Comparison of the {020} mechanical strains along the RD between the first and second cycle.

To get a sense of the sample-to-sample variation, the strains along the ND direction were compared. Figure 6.14 shows a complete comparison of 2 internal strains for the first cool-

ing and heating cycle between the first and second sample. It is seen there is some sample to sample variation. The variation between these peaks was at most 500 $\mu\varepsilon$, which seems large, but is small compared to the thermal strain magnitudes and predicted thermo-elastic strain that is shown in the next section. One potential source for the disagreement is slight sample orientation differences between samples. The sample orientations were determined by comparing diffraction spectra to identify the two unknown processing directions, as TD was oriented along the cylinder axes of both of the samples. The samples were then placed in the MgO crucible and attached at the end of a sample holder. It is possible such a method led to slight mis-orientation between the two samples. However, the results are qualitatively quite similar.
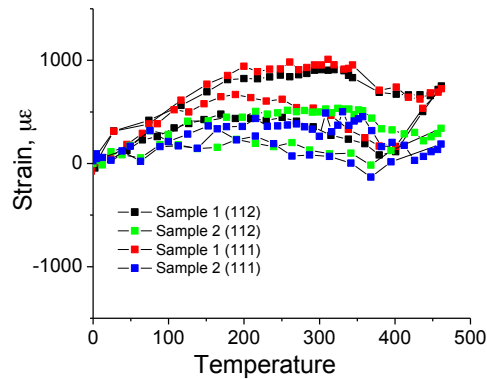
Figure 6.14: Comparison mechanical strain evolutions between the first and second sample along the ND direction

Comparison of with Elastic Strain Predictions

To understand the amount of relaxation that occurs, polycrystalline thermo-elastic (i.e. no plasticity) self-consistent simulations were conducted. Figure 6.15 shows a comparison of four crystallographic directions between the measured mechanical strain evolution and those predicted by the thermo-elastic model. As was seen in Chapter 2, the measured strains were drastically lower then the predicted strains. The deviation between predicted and measured

strains occurs after cooling only 25 ^{o}C. As such, the corresponding stress development can serve as an estimate of the onset of plasticity. It is also seen that the rank order of strain levels is consistent between the two scenarios. Due to the preferred orientation, there was not sufficient diffraction intensity to fit the diffraction peaks used here in the data presented in Chapter 2.
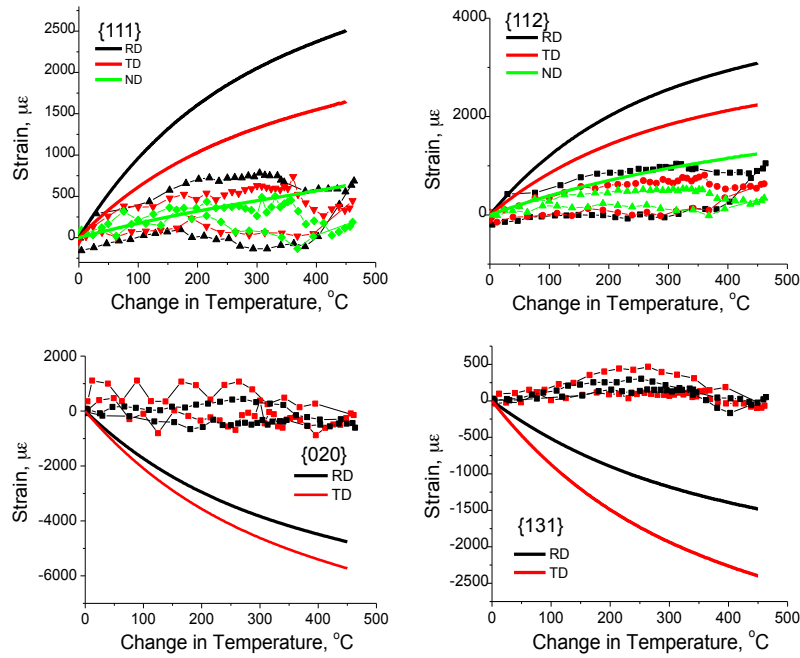
Figure 6.15: Comparison of the measured mechanical strains with the thermo-elastic predicted strains for 4 crystallographic directions along three sample directions where possible.

Discussion of the Induced Stress-State and Plastic Mechanisms

The thermo-elastic self-consistent predictions provide insight two key ways: (1) it provides an estimate of the required elastic stresses/strains to be relaxed, and (2) it allows for the estimation of the stress state at the onset of the plastic relaxation mechanisms. To address the first point, a simulation of a complete cooling cycle was conducted and the stresses and elastic strains inside the grains were analyzed. For the later point, simulations were conducted to the temperature

at which the internal strains varied greatly from the thermo-elastic predictions, which is seen after cooling 25 degrees.

In all of the thermo-elastic simulations at all temperatures, it was seen that the grains were in a multi-axial state, which included three unique non-zero principle stresses, independent of orientation grain orientation. When averaged in the specimen coordinates, the stress state of the grains averages to null, but in the crystallographic coordinates (meaning the stress state is transformed to the crystal coordinates for each grain) the average is non-zero. In the crystallographic coordinates, the principle stress directions were nearly identical to the crystallographic direction. Specifically, the stress-state was compressive along the *b*-direction, and tensile in the *a* and *c* directions. The combination of compressive and tensile stresses resulted a small hydrostatic pressure in the grains. To understand the multi-axial stress-state, it is helpful to use the Von Mises effective stress and strain, which are scalar reductions of a 2nd rank tensors based upon invariant quantities.

Figure 6.16 shows a distribution of the Von-Mises stress for all of the grains at 100 ^{o}C after cooling from 550 ^{o}C. If the mismatch strains are accommodated elastically, huge stresses are generated within the grains, which on average are nearly 1 GPa. However, the associated elastic strain from this is quite small. The Young's modulus can be approximated as 220 GPa, which would result in a strain of roughly 0.45% strain. This strain represents the amount of strain which could be accommodated by plasticity within each grain. As such, the thermal residual stress loading reflects that of a stress-relaxation experiment as opposed to a constant stress creep experiment. In both cases, the same plastic mechanisms are at play, but magnitudes and rates of strains vary. In a stress-relaxation experiment, a strain is fixed and the drop in stress is monitored, while in a creep experiment stress is applied and the strain rate is monitored. While these are thought of as two sides of the time coin, the difference is creep experiments give insights to the steady state creep response and relaxation gives insights into the primary creep regime. In the case of thermal residual stresses, a mismatch strain is imposed and then

plastically relaxed, so the plastic strains must be of the same order of magnitude as the thermal mismatch strains. A cooling cycle takes between 2-4 hours, this corresponds to an average strain rate of $\sim 10^{-7}$. This strain rate provides key insight that the relaxation mechanism is likely in the creep regime.
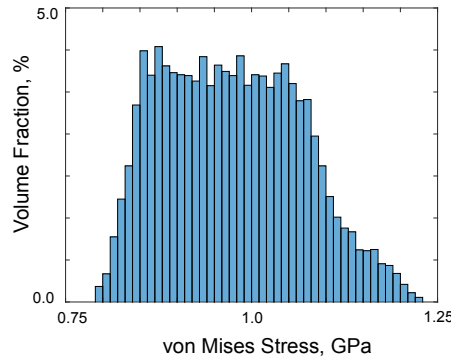
Figure 6.16: Distribution of the predicted thermo-elastic stress state shown as the Von-Misses stress after cooling from 550 to 100 ^{o}C

To get a full understanding of potential plastic deformation mechanisms, analyzing the stress states becomes critical. To estimate the stress state for plasticity, simulation of a 25 ^{o}C drop was conducted, representing the onset of plasticity. The average stress (in the crystal coordinates) was computed, and is shown below with the standard deviation:

$$\sigma = \begin{pmatrix} 32 \pm 6 & 0 \pm 4 & 2 \pm 3 \\ - & -48 \pm 5 & 0 \pm 6 \\ - & - & 15 \pm 6 \end{pmatrix} \text{MPa}$$

Despite similar thermal expansion properties, the stresses along the c-direction are lower than the stresses along the a-direction due to the texture. As seen in the pole figure (Fig. 6.2), the {100} direction does not show strong preferred orientation unlike the {001} which tends to align with the normal direction, which has the largest CTE, as shown in chapter 2. As such, the {001} orientations undergo a smaller mismatch strain then the {100} grains despite having

nearly identical thermal expansion coefficients. It is noted that under these conditions there is only a small hydrostatic pressure, ~ 1 MPa (trace of the stress tensor).

The potential deformation mechanisms are listed and discussed below:

Dislocation Glide- The stresses at the observed relaxation are far to low for rate insensitive glide to be the predominant deformation mechanism, especially considering the stress levels don't drastically increase as the sample cools to low temperatures, where one would expect thermal activation to play a predominant role. The RSS on the soft modes that are seen to be in the thermal activation plateau are not highly stressed, and therefore cannot relax the stresses. Power law creep would better explain the observed behavior. However, Chiswick reported that the level of thermal ratcheting increases with decreasing grain size on similarly textured material [14]. Power-Law glide is thought to be independent of grain size, so dislocation glide in the core of the grain would not fully explain the observed relaxation.

Deformation Twinning- As previously seen, dU readily twins under mechanical deformation. Twinning could explain the near temperature insensitivity of the relaxation observed, and the known twinning modes are highly stressed under the elastic stresses. However, twins were not observed in EBSD studies on as-cooled samples in two separate studies [1, 33] Also, twinning would not explain the thermal ratcheting, as the thermal cycles would likely lead to the twinning and de-twinning in a reversible way if they are the only mechanism for plastic strain accommodation.

*Coble/Nabaro Herring Creep-*Mass diffusion either through the grains (Nabbaro-Herring) or along the grain boundaries (Coble) creep could potentially explain the observed strain rates and stress levels. Using eq. 6.2 to estimate the maximum strain rate achievable at the observed stress level shows that the maximum strain rates at 500 ^{o}C with an imposed stress of 30 MPa are between $10^{-6} - 10^{-11}$ depending on the estimation of the activation energy term. If the activation energy is on the lower end, 0.4, this mechanism is definitely capable of relaxing the stresses observed in this material. Chiswick did not observe grain shape changes during his

thermal ratcheting experiment stop a net of 10% strain[14], which would be expected [70].

Grain Boundary Sliding (diffusion or slip accommodated)-Grain boundary sliding is consistent with the creep experiments that were run between 300-550 ^{o}C and at similar stress levels $\frac{\sigma}{\mu} \sim 10^{-4}$ [38], which saw a stress exponent of ~2.4. A similar stress exponent was reported elsewhere in the literature at similar temperatures [17, 69]. This falls in the range seen for grain boundary materials [74]. Grain boundary sliding could explain the void formation in the presence of impurities. Impurities are known to collect at the grain boundaries, and glide around them could pile up and create voids. The grain size dependence reported by Chiswick [14] would also be explained by such a mechanism, as grain boundary sliding is easier with decreasing grain size. Further, the formation of subgrains in large grained materials is characteristic of grain boundary sliding accommodated by the movement of intragranular dislocations but is not the case in finer grained materials where grain boundary sliding is accommodated by diffusion [74].

As such, grain boundary sliding and Coble creep are both considered most likely plastic relaxation mechanisms that can occur to explain the observed relaxation. Coble creep does not explain the development of subgrains that Chiswick reported [14], but dislocation accommodated grain boundary sliding would. Chiswick only reports the subgrains occurring in the large grain material, but it is possible that it developed in all the samples. Such an observation is consistent with the notion of switching from diffusion accommodated to dislocation accommodated region with decreasing grain size. Further testing is necessary to characterize this. Interestingly, grain boundary sliding and Coble creep are nearly isotropic. This begs the question: can an isotropic plastic mechanism interact with anisotropic thermo-elastic properties to induce ratcheting?

6.4   Conclusions

Based on in-situ neutron diffraction and thermo-elastic self-consistent modeling the following conclusions can be made:

- Despite reported annealing, the rolled material was seen to exhibit a texture change consistent with recrystallization during the heating and shortly after reaching the testing temperature of 550 ^{o}C. The time of the texture change was consistent with times for recrystallization reported in the literature. The apparent recrystallization caused a decrease in diffraction intensity of the {002} peaks along the plate normal direction while the {112} and {111} intensity increased. Along the TD and RD, the {131} peak dropped in intensity while the {112}, and {113} peaks gained in intensity. These changes in intensity were consistent with the textures on annealed samples presented in Chapters 3-5.

- The anisotropic CTE results in planar spacings increasing, decreasing or staying the same during heating or cooling. The {002} diffraction peak was seen to move toward the {021} diffraction peak, which does not appear to shift, as the sample was heated, and these two planes share a cubic equivalent plane to the {110} in the higher temperature BCC γ phase. The {113} and {041} peaks in the α phase were distinct at room temperature, but at elevated temperatures, they overlapped, and these two planes do not share a corresponding peak through the known shear transformation to the higher temperature phase. The {200}, {023} and {040} combined in a similar fashion, and only the {023} and {040} peak correspond to same peak in the higher temperature γ phase.

- The mechanical strains were much smaller in magnitude then the thermal strains, so the majority of internal strains were caused by thermal expansion/contraction. The measured mechanical strain evolutions differed from the thermo-elastic predictions within 25 ^{o}C of cooling, and were drastically smaller.

- Based on the strain rate and stresses at the onset of plasticity, it is believed that rate-sensitive mechanisms are responsible for the observed relaxation. The most likely relaxation mechanisms are grain boundary sliding accommodatedby dislocation motion, which would explain the grain size dependence, pore development around impurity based second phase particles, and the observed formation of subgrain boundaries. Such a mechanism of plasticity is expected to be much more isotropic than the low-temperature, high-stress plasticity mechanisms considered in the earlier chapters of this dissertation.

Chapter 7

Elasto-isotropic-ViscoPlastic Self-Consistent (EiVPSC) Modeling

C.A. Calhoun, L. Capolungo and S. R. Agnew

To address the potential for time-dependent isotropic plastic mechanisms discussed in the previous chapter, an Elasto-isotropic-ViscoPlastic Self-Consistent (EiVPSC) was developed to simulate the thermal cycling, and hopefully, predict thermal ratcheting. Unlike the Elasto-Plastic Self-Consistent scheme used in the previous chapters, the current model accounts for visco-plastic effects. In this model, the visco-plastic and elastic contributions are accounted for separately and summed in the aggregate, whereas the EPSC defined an elasto-plastic stiffness used in the averaging scheme. Elasto-ViscoPlastic Self-Consistent (EVPSC) modeling employs an additive decomposition of these two components to define the properties. Such an approach was described by Molinari to account for mechanical deformation [75]. More recently, this EVPSC approach was introduced in a crystal plasticity context and has achieved much success in capturing mechanical deformation [22]. Recently, it has even been utilized to predict related problem of the thermo-elastic residual stresses in zirconium alloys [76]. In

Zr alloys, however the thermal anisotropy is relatively small, so the internal strains can be accommodated elastically [20]. The current model employs the same mathematical backbone as EVPSC, but the single crystal yield surface is replaced with an isotropic visco-plastic response, hence terming this the EiVPSC approach. Additionally, the model is extended to account for plastic deformation resulting from thermal stresses.

7.1 Mathematical Model

In the self consistent scheme, a polycrystal is represented as a collection of grains, each having a unique orientation and volume fraction. Each grain is assumed to have a constitutive response, and together, they are "averaged" through the self-consistent scheme to predict the response of the polycrystal [20, 23, 75]. The aggregate is assumed to be a collection of ellipsoids embedded in a homogeneous effective. The averaging scheme invokes the Eshelby solution to determine the stress and strain state in an heterogeneous (meaning its response varies from that of the HEM) ellipsoid to help determine the stress state inside each grain. Such schemes were predominantly developed to predict the response of composite materials, and have been widely used to predict and understand deformation of polycrystals. In such a scheme, there are a few key ingredients: local response, linearization strategy, and micro-mechanical scheme.

7.1.1 Local-grain response

The underlying principle of the elasto-visco-plastic response is that the strain rate can be expressed as the sum of the different components of strain rates, based on the work of Molinari et al [75]. The total strain rate within a grain is described by the single crystal response which

can be written as:

$$\dot{\varepsilon} = \dot{\varepsilon}_T + \dot{\varepsilon}_e + \dot{\varepsilon}_p \tag{7.1}$$

where $\dot{\varepsilon}$, $\dot{\varepsilon}_T$, $\dot{\varepsilon}_e$, $\dot{\varepsilon}_p$ are the total, thermal, elastic and plastic strain rate, respectively. Temperature-dependent linear thermo-elastic response is assumed as was done in the previous chapters. The single crystal coefficients of thermal expansion and compliance were assumed to have the same temperature dependencies described in Chapter 2. The thermal strain-rate comes from the thermal expansion, α (again given by the single crystal response) and temperature rate, $\dot{T}$. The elastic component is given by the elastic compliance, $\mathbf{M_e}$, (given by the single crystal response) and the stress rate, $\dot{\sigma}$. For plasticity, an isotropic visco-plastic response is assumed. The viscoplastic component is given by the viscoplastic compliance, $\mathbf{M_p}$. $\dot{\varepsilon}_b$ is the back extrapolated term, which comes about since the tangent of the plastic flow curve does not intersect the origin, and the tangent moduli is a linearization of the local plastic response. The model employs the so-called secant linearization scheme. The total strain can be written as:

$$\dot{\varepsilon} = \alpha\dot{T} + \mathbf{M}_e : \dot{\sigma} + \mathbf{M}_p : \sigma + \dot{\varepsilon}_b \tag{7.2}$$

Visco-plastic response

As was discussed in the previous chapter, it was suspected that locally isotropic mechanisms could be responsible. As such, an isotropic visco-plastic law was used, which can be written as:

$$\dot{\varepsilon}_p = \dot{\varepsilon}_o \left(\frac{\sigma_v}{\sigma_{th}}\right)^n \frac{S_{ij}}{\sigma_v} \tag{7.3}$$

where, $\dot{\varepsilon}_o$, σ_{th}, n, σ_v, and S_{ij} are a visco-plastic constant, threshold stress, rate sensitivity exponent, Von-Mises stress, and the deviator stress, respectively. This can be reduced to:

$$\dot{\varepsilon}_p = A \, (\sigma_v)^{n-1} \, S_{ij} \tag{7.4}$$

The deviatoric stress is written as:

$$S_{ij} = \sigma_{ij} - \frac{\delta_{ij}}{3} \sigma_{kk} \tag{7.5}$$

Using the above definition, the Von Mises stress can be written as:

$$\sigma_v = \sqrt{\frac{3}{2} S_{ij} S_{ij}} \tag{7.6}$$

By taking the derivative of the constitutive law, the visco-plastic compliance tensor can be written as:

$$\mathbf{M}^p_{ijkl} = \frac{\partial \dot{\varepsilon}_p}{\partial \sigma} = A \left(\frac{3 S_{ij} S_{kl} (n-1)}{2} \sigma_v^{\,n-3} + (I_{ijkl} - \frac{\delta_{kl} \delta_{ij}}{3}) \sigma_v^{\,n-1} \right) \tag{7.7}$$

To account for the temperature sensitivity of the flow stress, the same exponential form from Chapter 5 was used. It is written as:

$$\sigma_{th} = \sigma_o \exp \left(\frac{-(T - T_{ref})}{\beta} \right) \tag{7.8}$$

where T_{ref} is a reference temperature, and β is the temperature sensitivity parameter. It is noted that the creep experiments reported a temperature dependence that was much more subtle (meaning the transitions is much smoother) for the steady state response [38]. It is noted that the magnitude of strains are such that deformation would be in the primary creep regime, so

parameters coming from steady-state creep are not directly applicable.

7.1.2 Polycrystal response

Based on the work of Molinari and co-workers, we also assume the polycrystal also has a response of the form:

$$\dot{E} = \bar{\alpha}\dot{T} + \bar{\mathbf{M}}_e : \dot{\Sigma} + \bar{\mathbf{M}}_p : \Sigma \tag{7.9}$$

where $\dot{E}$, $\dot{T}$, $\dot{\Sigma}$, and Σ are the total strain rate, temperature rate, volume average stress rate, and volume average stress, respectively. $\bar{\alpha}$, $\bar{\mathbf{M}}_e$, and $\bar{\mathbf{M}}_p$ are the effective thermal expansion, elastic compliance, and plastic compliance, respectively.

7.1.3 Micromechanics and self-consistency

Using the local constitutive response, the self consistent scheme allows for the prediction of the aggregate response. This is where the additive decoupling of Molinari is assumed [75]; the elastic and visco-plastic properties are solved for separately and then summed together. AS illustrated below, the effective thermal expansion of the polycrystal has a elastic and visco-plastic term. The self-consistent scheme between the visco-plastic and elastic is very similar, but solving for each varies. The differences stem from the fact that elastic compliance is independent of stress, where as the visco-plastic compliance varies with stress. As such, the solving of the visco-plastic stiffness is more involved. The equations listed below are derived from the assumption that the volume averaged stress and strain rate equals that of the aggregate. Below, only the relevant equations are listed.

Elastic

First for every grain, the interaction tensor must be computed for the elastic case.

$$\tilde{\mathbf{M}}_e = (\mathbf{I} - \mathbf{S}_e)^{-1} : \mathbf{S}_e : \bar{\mathbf{M}}_\mathbf{e} \tag{7.10}$$

$\tilde{\mathbf{M}}_e$ is the elastic interaction tensor. $\mathbf{S}_e$ is the Eshelby tensor computed using the elastic proper-ties of the aggregate $\bar{\mathbf{M}}_\mathbf{e}$, and the grain shape. Now to compute the localization tensor $\mathbf{V}$:

$$\mathbf{V} = (\mathbf{M}_e + \tilde{\mathbf{M}}_e)^{-1} : (\bar{\mathbf{M}}_e + \tilde{\mathbf{M}}_e) \tag{7.11}$$

Now that every grain has its localization tensor defined, the elastic compliance can be defined.

$$\bar{\mathbf{M}}_e = \langle \mathbf{M}_e : \mathbf{V} \rangle : \langle \mathbf{V} \rangle^{-1} \tag{7.12}$$

It is clear the $\mathbf{V}$ depends on the aggregate compliance, so this is solved using an iterative process.

Visco-Plastic

As with the elastic case, the first step necessary to compute the plastic compliance is to compute the interaction tensors:

$$\tilde{\mathbf{M}}_v = (\mathbf{I} - \mathbf{S}_p)^{-1} : \mathbf{S}_p : \bar{\mathbf{M}}_v \tag{7.13}$$

From there, the localization terms are computed. The plastic localization is computed.

$$\mathbf{B} = (\mathbf{M}_p + \tilde{\mathbf{M}}_p)^{-1} : (\bar{\mathbf{M}}_p + \tilde{\mathbf{M}}_p) \tag{7.14}$$

In a similar way to the elastic compliance, the plastic compliance is computed using the below equation:

$$\bar{\mathbf{M}}_p = \langle \mathbf{M} : \mathbf{B} \rangle : \langle \mathbf{B} \rangle^{-1} \tag{7.15}$$

Thermal

In this scheme, the elastic and plastic response are decoupled to get the effective thermal expansion properties. The elastic component of the effective CTE was provided by Qiao et al. [76] and written as:

$$\bar{\alpha}^e = \bar{\mathbf{M}}_e \langle (\mathbf{M}_e^{-1} + \tilde{\mathbf{M}}_e^{-1})^{-1} \rangle^{-1} \langle (\mathbf{M}_e^{-1} + \tilde{\mathbf{M}}_e^{-1})^{-1} \mathbf{M}_e^{-1} \alpha^T \rangle \tag{7.16}$$

Similarly the plastic component of the CTE can be written as:

$$\bar{\alpha}^p = \bar{\mathbf{M}}_p \langle (\mathbf{M}_p^{-1} + \tilde{\mathbf{M}}_p^{-1})^{-1} \rangle^{-1} \langle (\mathbf{M}_p^{-1} + \tilde{\mathbf{M}}_p^{-1})^{-1} \mathbf{M}_p^{-1} \alpha^T \rangle \tag{7.17}$$

To get the aggregate CTE, $\bar{\alpha}$, response it becomes:

$$\bar{\alpha} = \bar{\alpha}^p + \bar{\alpha}^e \tag{7.18}$$

7.1.4   Global

The localization law for the polycrystal is given by:

$$(\dot{\varepsilon} - \dot{E}) = -\tilde{\mathbf{M}}_e : (\dot{\sigma} - \dot{\Sigma}) - \tilde{\mathbf{M}}_p : (\sigma - \Sigma) \tag{7.19}$$

For the present case of thermal ratcheting under no applied load, the global stress state, Σ, is always zero, so $\dot{\Sigma} = 0$.

7.2 Algorithm

In order to solve the macroscopic properties, all 3 of the properties are computed. Fortunately, the elastic properties are decoupled from the stress state, and the elastic portion of thermal expansion is easily computed once the elastic and plastic compliances are determined. As such, the effective elastic compliance is solved iteratively using a straightforward elastic self consistent scheme. The basic premise is to begin with an initial guess for the elastic compliance of the polycrystal, typically the rule of mixtures or inverse rule of mixtures and then compute the localization tensors $\mathbf{V}$ for each grain. This depends on the calculation of the Eshelby tensor for the elastic compliance $\mathbf{S}_e$ to compute the interaction tensor (eq. 7.10). With the interaction tensor in hand, the localization tensors are computed (7.11). The elastic compliance is then computed (7.12). The recently computed compliance is compared with the initial guess. If the compliances vary too much, the computation is redone using the newly computed compliance as the initial guess. It is noted that both $\bar{\mathbf{M}}_e$ and $\tilde{\mathbf{M}}_e$ are both stored for later iterative solving. Once the elastic compliance is computed, the elastic portion of the thermal expansion properties can be computed (7.16). Fortunately, it does not require iteration.

Solving for the visco-plastic compliance is more intensive process than the thermo-elastic properties, because they are directly linked to the stress state. As such, it takes a nested loop structure to compute the viscoplastic compliance tensor and back extrapolated term. The bulk compliance is varied inside the inner loop, while the local stress and strain states are varied in the outer loop. Inside the inner loop, the individual stress states are assumed for each grain based off the last straining step or iteration of the outer loop, which provides a compliance given by eq. 7.7. Using the assumed macroscopic compliance, the Eshelby tensors are computed

($\mathbf{S}_p$). Then, the localization tensors are computed (7.13 and 7.14). The macroscopic visco-plastic compliance is then computed (7.15). The new compliance is compared with the input for the iteration, if they don't match another iteration is started using the new VP compliance. Once convergence is achieved, the plastic portion of the CTE is computed using eq. 7.17.

The macroscopic strain rate is ultimately computed using eq. 7.9 and the imposed boundary conditions. The stresses inside each grain are computed by solving the non-linear equation that comes from combining the localization equation (7.19), and the local constitutive response (7.2) through a Newton-Raphson Scheme described in the next section. Using the local stresses, the plastic strain rates are computed using the constitutive law and the local viscoplastic moduli is updated. The volume average stress and strain rate are thus computed. The average is compared with the macroscopic strain, and average stress is compared to see how close it is to a stress free condition. For each step this is carried out until a convergence is achieved, even if the average and macro response do not agree well. A residual error arose in the comparison of the average stress, so this was addressed with a correction in the 7.19 law. This error is a shortcoming of the assumption that the plastic and elastic strains can be decoupled, and this approach of handling the error minimized the discrepancy in the average stress state. The error was investigated and addressed in the upcoming section.

Compute Elastic and CTE

Assume local stresses, strain rates, and compliance

Assume macro compliance and back extrapolated term

Compute Eshelby tensor and interation tensors for VP

$$\mathbf{B} = (\mathbf{M}_p + \tilde{\mathbf{M}}_p)^{-1} : (\bar{\mathbf{M}}_p + \tilde{\mathbf{M}}_p)$$

Compute macro compliance and back exptrapolated term

$$\bar{\mathbf{M}}_p = \langle \mathbf{M} : \mathbf{B} \rangle : \langle \mathbf{B} \rangle^{-1}$$

Compare new macro compliance and back exptrapolated term

Apply imposed macro conditions to get macro stress and strain rate

$$\dot{\varepsilon} = \mathbf{M_e} : \dot{\sigma} + \mathbf{M_p} : \sigma + \alpha \dot{\mathbf{T}}$$

Compute local stresses Newton-Raphson

$$(\dot{\varepsilon} - \dot{\mathbf{E}}) = -\tilde{\mathbf{M}}_e : \dot{\sigma} - \tilde{\mathbf{M}}_p : \sigma$$

Compute local strain rates and compliances

$$\dot{\varepsilon} = \mathbf{M_e} : \dot{\sigma} + \mathbf{M_p} : \sigma + \alpha \dot{\mathbf{T}}$$

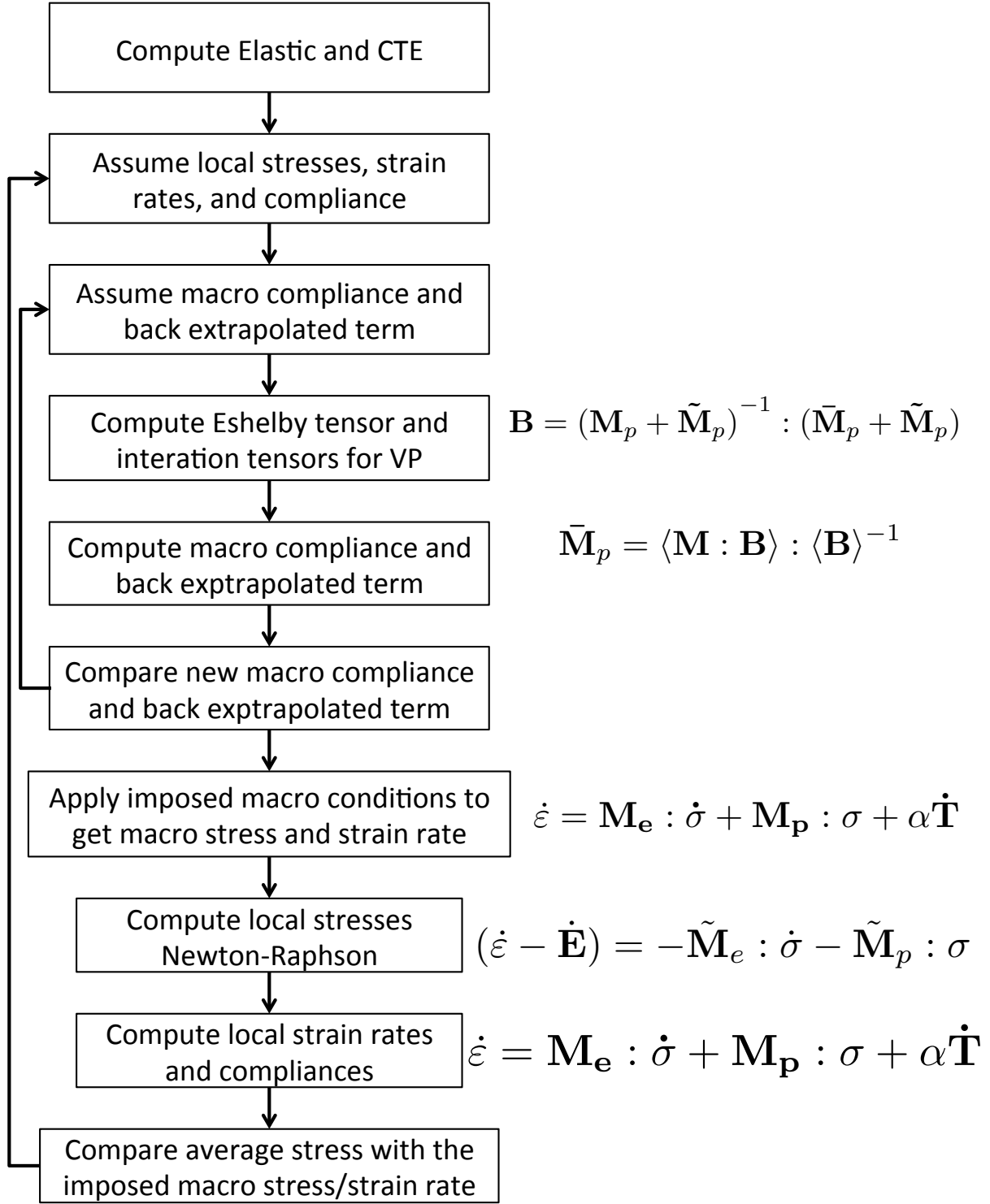Compare average stress with the imposed macro stress/strain rate

Figure 7.1: Flowchart of the employed EiVPSC modeling scheme.

7.2.1 Newton-Raphson Scheme

Once the macroscopic compliance is computed, the next step is to compute the local stresses using a Newton-Raphson scheme. This is an iterative process to solve for the stresses, using the localization equation (eq. 7.19), combined with the macroscopic boundary conditions, and the local constitutive response. Using the local constitutive law, the local strain rate is eliminated from the localization equation, which can be written as:

$$(\mathbf{M}_e : \dot{\sigma} + \dot{\varepsilon}_o \sigma_v{}^{n-1} S_{ij} + \alpha \dot{T} - \dot{E}) = -\tilde{\mathbf{M}}_e : \dot{\sigma} - \tilde{\mathbf{M}}_p : \sigma \tag{7.20}$$

Now the equation only has one unknown and that is the stress state. Rearranging this we can have an equation that equates to zero.

$$0 = (\mathbf{M}_e : \dot{\sigma} + \dot{\varepsilon}_o \sigma_v{}^{n-1} S + \alpha \dot{T} - \dot{E}) + \tilde{\mathbf{M}}_e : \dot{\sigma} + \tilde{\mathbf{M}}_p : \sigma \tag{7.21}$$

Now, the Newton-Raphson method can be used to iteratively solve for the stress state. The way it works is to find the zeros for a function, which we will call everything on the right side of the above equation, and the way in which is solved

$$\sigma_i^n = \sigma_i^{n-1} - \frac{\partial F_i}{\partial \sigma_j} F_j \tag{7.22}$$

where n is the iteration, and F is the function (eq. 7.21) which is being solved for zero.

$$\frac{\partial F_i}{\partial \sigma_j} = M_{ij}^e dt^{-1} + \dot{\varepsilon}_o \sigma_v{}^{n-1} \frac{\partial S_i}{\partial \sigma_j} + \dot{\varepsilon}_o S_i \frac{\partial (\sigma_v{}^{n-1})}{\partial \sigma_j} + \tilde{M}_{ij}^e dt^{-1} + \tilde{M}_{ij}^p \tag{7.23}$$

Substituting in equation 7.7

$$\frac{\partial F_i}{\partial \sigma_j} = M_{ij}^e dt^{-1} + M_{ij}^p + \tilde{M}_{ij}^e dt^{-1} + \tilde{M}_{ij}^p \qquad (7.24)$$

7.3 Texture

A discrete texture is necessary for the model. Since the neutron experiments (see previous chapters) did not yield reliable macroscopic strain evolution data during thermal cycles, the simulations aimed to explain the observations of Chiswick [14]. In his study, the samples came from extruded bars. Based on the reported straight rolled texture [8], the extrusion process likely oriented the (020) pole along the extrusion direction, since this orientation is known to orient with the rolling direction. In rolling, the (002) orientations fall along the normal direction. Due to the symmetry of the processing, likely the (200) and (002) orientations would be evenly distributed transverse to the extrusion direction. This reduces to a (020) fiber texture. Fortunately, fiber textures can be readily simulated with MTEX [65]. Figure 7.2 shows a resulting texture. In this, orthorhombic sample symmetry is imposed which reduces the required pole figures to quarter circles as opposed to the complete circles reported in the previous chapters.
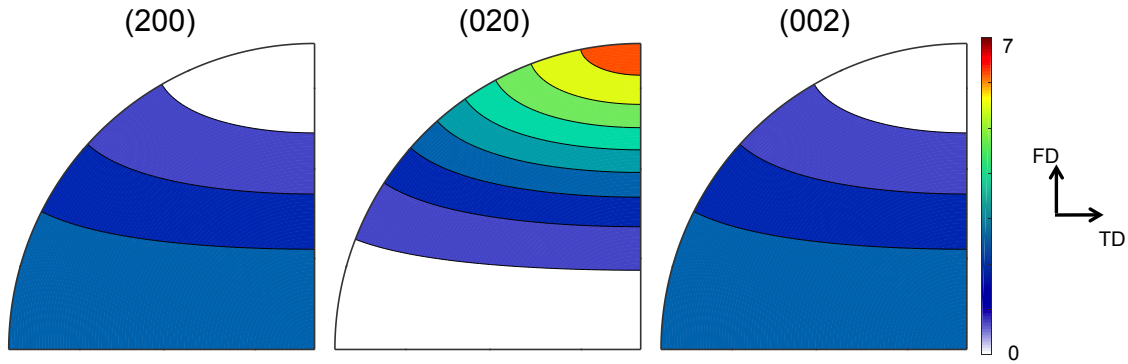

Figure 7.2: Pole figures from simulated fiber texture used from ratcheting simulations.

7.4 Investigation of Residual Errors

After completion of the initial coding, preliminary thermal ratcheting simulations were conducted. A variety of parameters were run, and the strain response through thermal cycling was investigated. Figure 7.3 shows a plot of predicted strain response as well as the resulting average stress in the aggregate. Parameters for this simulation where chosen to provide an example of ratcheting. Not all of the simulations resulted in ratcheting, and that will be discussed in the results section of this chapters. In the simulations that had ratcheting, the polycrystal lengthens along the (020) fiber direction (termed the fiber direction for the rest of the chapter), which is analogous to the extrusion direction, and shrinks along the transverse direction, which qualitatively agrees with the experimental investigation [14]. One downside of this simulation is that a residual macroscopic stress develops within the aggregate. Ideally, the volumetric average stress would be zero, but due to short comings of the additive decoupling of the strains, this is not the case. The stress is seen to be tensile along the fiber direction and compressive along the transverse direction.
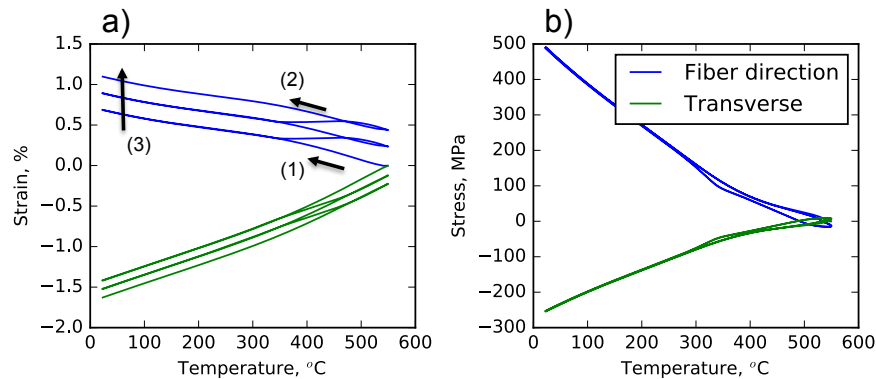

Figure 7.3: Plot of the predicted (a) strain and (b) the average stress during thermal cycling with $\sim \dot{T}$=10 ^{o}C/min, n=20, σ_o=50 MPa and β=100 K. Highlighted are: (1) initial cooling curve, (2) the third cooling cycle and (3) the increasing strain with increased cycling

In an effort to eliminate the residual error stress, different numerical strategies were taken.

Mainly, an imaginary error stress, Σ_{err} was added. The error stress was defined as the average stress in the previous stress increment. This was viewed as an aggregate stress (i.e. Σ). This aggregate stress is seen in two of the governing equations: 1.) the aggregate response (eq. 7.9) and 2.) the localization equation (eq. 7.19). Table 7.4 shows the equations imposed in the 3 correction strategies. The localization equation is used to compute the local stresses, which is what is being averaged to get the error stress. It is noted that definitionally Σ_{err} should be zero, so adding a term equal to zero does not invalidate any of the above equations. This approach is essentially synthetically imposing the negative of the error stress.

Table 7.1: Summary of the different approaches for eliminating the residual error in the modeling scheme.

Approach	Macro-equation	Localization eq.
none	$\dot{\varepsilon} = \bar{\alpha}\dot{T}$	$(\dot{\varepsilon} - \dot{E}) = -\tilde{\mathbf{M}}_e : (\dot{\sigma}) - \tilde{\mathbf{M}}_p : (\sigma)$
1	$\dot{\varepsilon} = \bar{\alpha}\dot{T}$	$(\dot{\varepsilon} - \dot{E}) = -\tilde{\mathbf{M}}_e : (\dot{\sigma} + \frac{\Sigma_{err}}{t_{inc}}) - \tilde{\mathbf{M}}_p : (\sigma + \Sigma_{err})$
2	$\dot{\varepsilon} = \bar{\alpha}\dot{T} + \bar{M}_p\Sigma_{err}$	$(\dot{\varepsilon} - \dot{E}) = -\tilde{\mathbf{M}}_e : (\dot{\sigma} + \frac{\Sigma_{err}}{t_{inc}}) - \tilde{\mathbf{M}}_p : (\sigma + \Sigma_{err})$
2	$\dot{\varepsilon} = \bar{\alpha}\dot{T} + \bar{M}_p\Sigma_{err}$	$(\dot{\varepsilon} - \dot{E}) = -\tilde{\mathbf{M}}_e : (\dot{\sigma}) - \tilde{\mathbf{M}}_p : (\sigma)$

The correction strategies were coded and employed in various simulations. To get an idea of the shift in errors of different algorithms, it was important to define the error terms. In self-consistent approaches, it is common to compare the average strain/stress with the aggregate strain/stress. In this case, the aggregate stress was taken to be zero. As such, the error in stress was computed to be the sum of the average stress tensor components. The error in strain was computed as the norm of the difference between the aggregate and average strain divided by the norm of the average of these two tensors. Figure 7.4 shows a plot of error values for two sets of

simulations with varying values of the rate sensitivity exponent, *n*. In both sets of simulations, it is seen that the error in stress is quite large. In typical mechanical deformation simulations, this value was less then 1 %. In the first set of simulations, it is seen that the lowest error in strain occurs in the third correction approach, which has the error stress added to only the aggregate response. This approach does not improve the error in residual stress. Adding the error stress to the localization drastically reduces the overall stress in the error, but increases the error in the strain.

Figure 7.4: Plot of the residual error values for the 4 different approaches for two trial cases, n= 2(a &b) and n=20 (c & d). The error in strain between the average strain and the computed aggregate is shown in subfigures (a & c) and the errors in stress is shown in subfigures (b & d).

For thoroughness, it is helpful to see the variation in the predicted strain responses between the simulation approaches. Figure 7.5 shows the predicted strains for the two sets of simula-tions with varying correction approaches. When *n* = 2, ratcheting is only predicted when the

error stress is added to the localization equation and not the macroscopic response. All of the approaches predicted qualitatively correct ratcheting when *n*=20, although degree of ratcheting varies between the approaches.
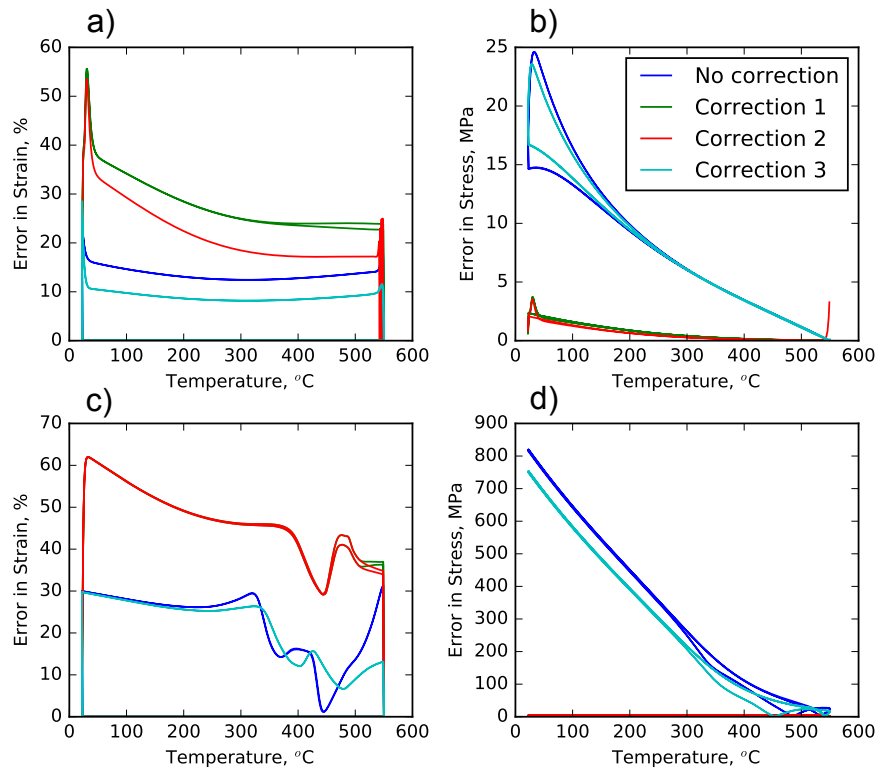

Figure 7.5: Plot of the residual error values for the 4 different approaches for two trial cases, n= 2(a &b) and n=20 (c & d). Subfigures a & c show strain long the fiber direction, and subfigures (b & d) show the predicted strain along the transverse direction.

Again for thoroughness, comparison of the average stresses can also been seen. Figure 7.6 shows a plot of the stresses for the two simulation sets. The stresses in the case when *n*=2 shows a positive stress in both principle directions, and are almost completely eliminated with the error stress is included in the localization equation. When *n*=20, it is seen the error stress is tensile along the fiber direction and compressive with a magnitude about half of the fiber direction. This average tensile stress along the fiber direction explains the increased ratcheting in the simulations that did not have the error stress in the localization equation. At the risk

of redundancy, the ratcheting is still predicted for the case where the residual stress error is corrected at the end of every time step, so that essentially no net stress is applied.
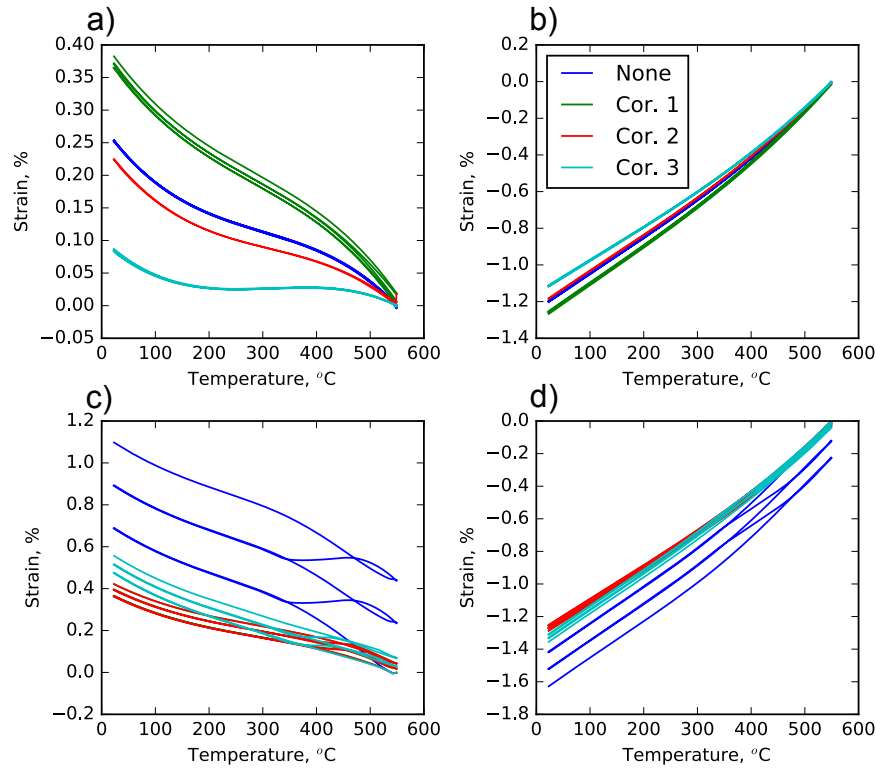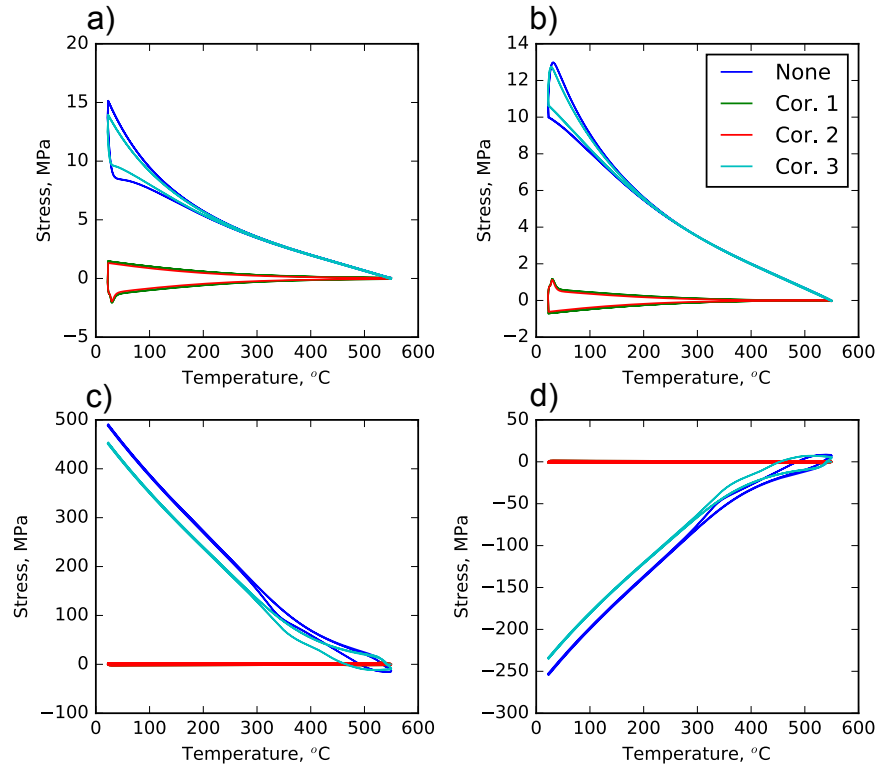

Figure 7.6: Plot of the residual error values for the 4 different approaches for two trial cases, n= 2(a &b) and n=20 (c & d). Subfigures a & c show average stress long the fiber direction, and subfigures (b & d) show the average stress along the transverse direction.

After comparing these approaches, it was determined that correction 2, would be used for all subsequent simulations. The rest of the results in this chapter have the error stresses added to both the macroscopic response as well as the localization equation. It is noted that strategy 3 (only having a error stress in the macroscopic response), predicts similar response. Conclusions made in subsequent sections can be drawn from either of these two strategies.

7.5 Results and Discussion

A large set of simulations have been conducted to explore the parameter space, and a few of the results have been selected to provide an understanding of the model predictions. As a starting point, it is beneficial to see the results from a single simulation. Figure 7.7 shows the predicted results from a simulation between 550 ^{o}C and 25 ^{o}C, for 2 complete thermal cycles between 550 ^{o}C and 25 ^{o}C and a subsequent cooling to 25 ^{o}C. Each simulation presented in the remainder of this chapter assumed that cooling and heating cycle took 6000 seconds, which corresponds to a relatively fast cooling ~10 ^{o}C/s. In this simulation, n was set to 4, with σ_o=50 MPa, and β=100 ^{o}C. These parameter values made physical sense, mainly due to the relatively low rate sensitivity exponent. Thermal ratcheting is clearly seen along the direction of the (020) fiber texture as a positive strain is developed during the cycling, and is subtly seen in the transverse direction. The ratcheting is volume conserving, and the total strain in the transverse directions is much larger in magnitude, and the ratcheting strain is halved in magnitude. As such, the ratcheting strain is often lost when looking at the overall strain in the transverse directions. The magnitude of this plastic strain is ~0.01 % per cycle with the current parameter set. In the extreme, Chiswick reported nearly 500 % strain over 3000 thermal cycles, so which reduces to ~0.16% per cycle [14]. However, he typically found about 100 - 300 $\mu\varepsilon$ per cycle or alternatively, 0.01 - 0.03% per cycle, in the first cycle. This range directly overlaps with the current model.

To get an idea of the heating and cooling rate dependence on the predicted ratcheting, simulations were conducted in which varied the cooling rate. Figure 7.8 shows the results of three simulations where all parameters were held constant aside from the heating and cooling rates. The heating and cooling rates were consistent within each simulation and varied by an order of magnitude. It is seen that the overall predicted thermal ratcheting is independent of the cycling rate. Slight variations in the strain evolution are seen, but the strains at the highest

Figure 7.7: Plot of the predicted predicted strain along the (a) the fiber and (b) transverse directions during thermal cycling showing predicted thermal ratcheting ($\dot{T}$=10 ^{o}C/min, n=4, σ_o= 50 MPa and β=100 K).

and lowest temperatures are consistent across all of the experiments.

Figure 7.8: Plot of the predicted predicted strain along the (a) the fiber and (b) transverse directions during thermal cycling showing predicted effects of heating and cooling rate ($\dot{T}$=10 ^{o}C/min, n=10, σ_o= 50 MPa and β=100 K).

7.5.1   Model Parameter Exploration

Due to the relative simplicity of this model, it is possible to parametrically study the effects of each model parameter. There are only 3 independent parameters to describe the plasticity in this model, as compared to the ~16 parameters used to describe the anisotropic response

for mechanical deformation. As such, results from different slices of the parameter space are presented to provide insight into the sensitivities in the model. For the sake of consistency, all of the following simulations used the texture shown in Figure 7.2 unless otherwise noted. Additionally, all of the following simulations inputed cycling times of 6000 s.

The first parameter slice examined is the rate sensitivity exponent, n from eq 7.4. Figure 7.9 shows the results of simulations in which all parameters and inputs were kept constant aside from the rate sensitivity exponent. It is seen that increasing the rate sensitivity exponent even to values beyond what is typically considered in the 'creep' regime increases the amount of ratcheting predicted. However, it is noted that ratcheting is predicted at all values of n. Furthermore, it was seen that ratcheting could be predicted with n as low as 2. As such, the sensitivity to this exponent is present and a detailed experimental study and model calibration is required to determine this parameter and to identify which mechanistic regime is being activated during ratcheting through the exponent.
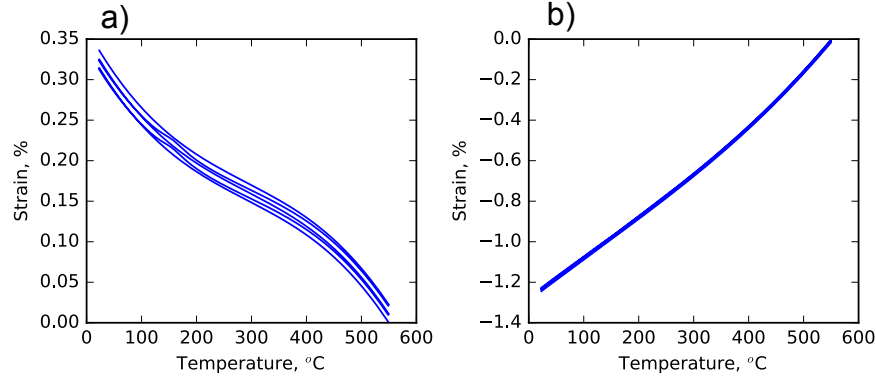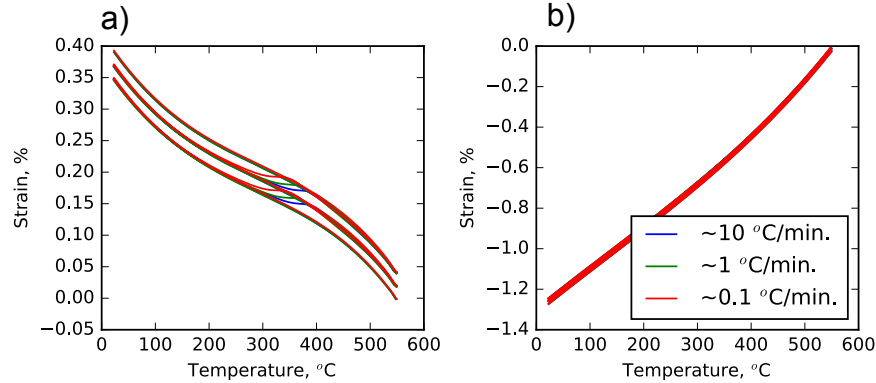

Figure 7.9: Plot of the predicted predicted strain along the (a) the fiber and (b) transverse directions during thermal cycling showing the effect of the rate sensitivity exponent ($\dot{T}$=10 ^{o}C/min,σ_{th}= 50 MPa and β=100 K).

The next parameter explored is the flow stress term, σ_{th} from equation 7.4. Figure 7.10 shows the results of simulations with all things identical except the σ_{th} value. It is seen that this parameter does not have a drastic effect on the overall predicted ratcheting, as all of the

3 simulations predicted nearly identical levels of ratcheting. The strain paths during heating and cooling varied, but the end levels were pretty consistent among the three scenarios. If the threshold stress is increased much more (~500 MPa at this temperature sensitivity), then the ratcheting is eliminated completely, and the deformation remains purely thermo-elastic. It is noted that the σ_{th} parameter is mathematically linked with the value of ε_o, which was chosen to be 1 for all of the simulations presented here. A different choice of this value can affect the sensitivity of the model to the threshold stress.
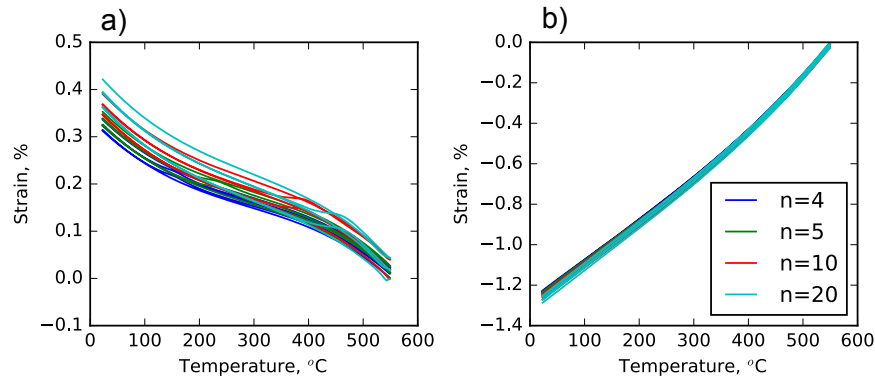

Figure 7.10: Plot of the predicted predicted strain along the (a) the fiber and (b) transverse directions during thermal cycling showing the effect of the σ_{th} parameter ($\dot{T}$=10 ^{o}C/min, n=4 and β=100 K).

The last model parameter explored is the temperature sensitivity, β from eq. 7.8. Figure 7.11 shows the resulting strains from simulations that were identical aside from the temperature sensitivity parameter. It is seen that the amount of ratcheting increases with decreasing the temperature sensitivity parameter. The β parameter is such that a low value implies a high temperature sensitivities, and a high value would imply slight temperature sensitivities. As such, the model predicts that temperature sensitivity is critical for ratcheting if an isotropic mechanism is the source of the plastic deformation. For reference, β values between 160-1000 K were reported for the slip modes at lower temperature [35].
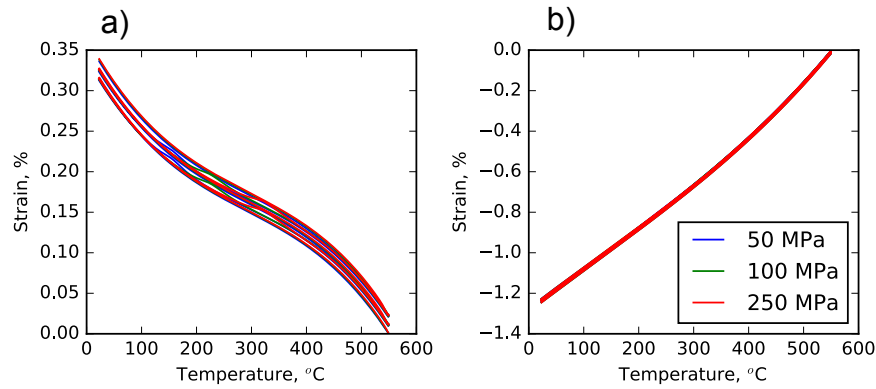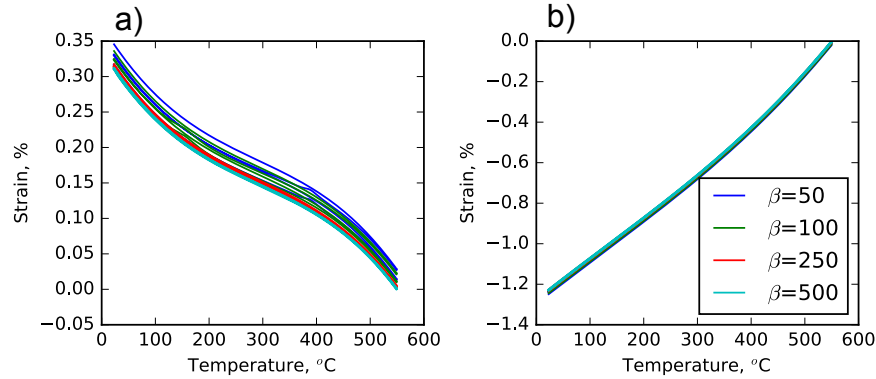
Figure 7.11: Plot of the predicted predicted strain along the (a) the fiber and (b) transverse directions during thermal cycling showing the effect of the temperature sensitivity parameter (β) ($\dot{T}$=10 ^{o}C/min, n=4 and σ_o= 50 MPa).

7.5.2 Effect of Texture

Chiswick observed an increase in ratcheting with an increase in preferred orientation [14]. To investigate the model implications of texture, additional fiber textures were generated and used in subsequent simulations. Figure 7.12 shows pole figures of the 6 textures used for this study. In the first texture, the fiber texture is the strongest. Since a and c directions exhibit nearly identical thermal expansion, this case should develop the lowest amount of thermal residual stresses. To the extreme, this would be the case of a single crystal which does not exhibit thermal ratcheting due to the lack of thermal mis-match strains. Likely, the study of Chiswick was not able to reach this threshold of texture being too intense. In the other extreme, a completely random texture will develop large thermal residual stresses, but will likely not ratchet because all of the local plasticity will average to no net ratcheting.

Using the above textures, thermal cycling simulations were conducted. Figure 7.13 shows plots of the predicted strain evolution for the simulated textures. It is seen that as the fiber strength is increased, the direction of the thermal strain changes, as is to be expected. In the random case, the expansion is isotropic, and is negative as it cools. As the texture strength increases the direction changes to be positive during cooling, due to the negative CTE value
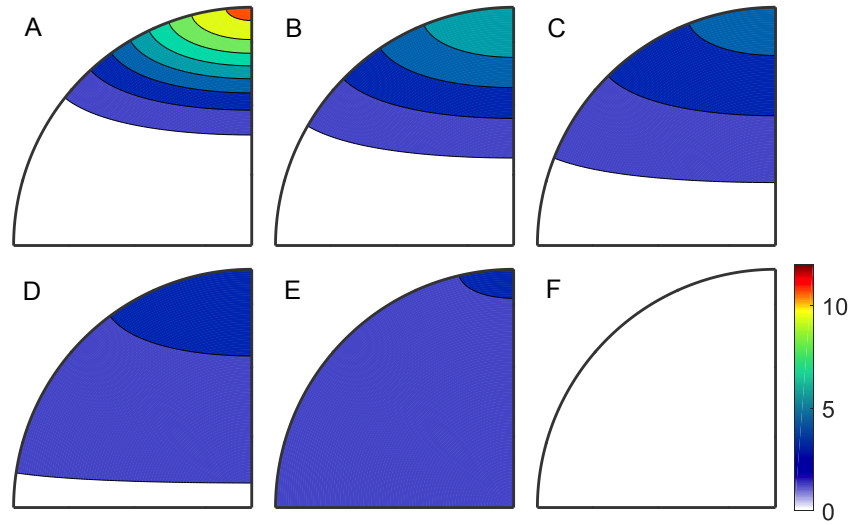
Figure 7.12: Comparison of (020) pole figures from simulated fiber textures used from ratcheting simulations ordered from most intense to completely random.

along the *b*-direction. In regards to the ratcheting, it is seen that the completely random texture exhibits no ratcheting, which provides a good sanity check that the model is not fictitiously imposing a strain. As the fiber strength increases, the amount of thermal ratcheting initially increases before saturating and ultimately drops. The largest ratcheting is seen to occur in texture c, which has a peak intensity in the (020) pole figure around 4. This is around the peak strength of textures reported in the literature [1, 8, 31, 35]. As such, it is unlikely that Chiswick was able to experimentally observe textures much stronger than this case. As such, he likely would not observe the saturation in ratcheting strain. However, this saturation must exist, and provides another qualitative check that the model working properly.

7.6 Conclusions

An Elasto-isotropic-Visco-Plastic Self Consistent model was presented to predict the the plastic response during thermal cycling of α-uranium. From the results of this model, the following conclusions are made:
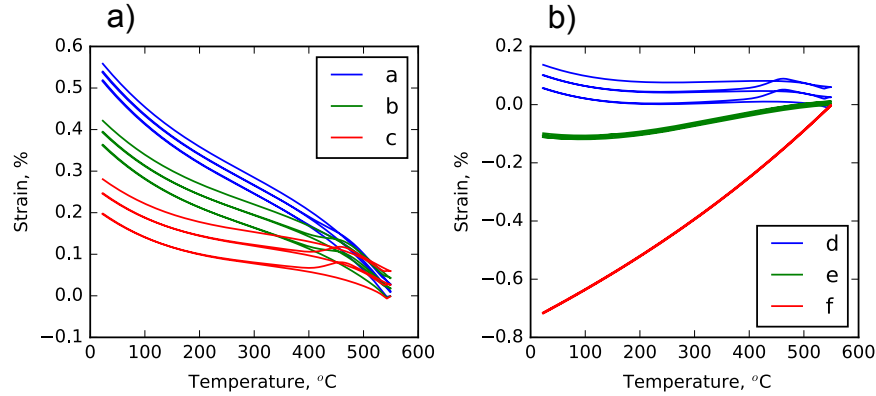
Figure 7.13: Plot of the strains along the fiber direction for varying texture strengths. ($\dot{T}$=10 ^{o}C/min, σ_{th}=50 MPa, β=100, and n=4)

- Thermal ratcheting in polycrystalline α-uranium is explained through the interaction of anisotropic thermo-elastic response of the single crystal with rate sensitive isotropic plasticity mechanisms. A model that captured the isotropic plasticity only required 3 independent parameters (thresh-hold stress, temperature sensitivity, and rate-sensitive exponent) and was able to predict thermal ratcheting.

- The EiVPSC approach resulted in a numerical error stress being imposed on the aggregate, which can be drastically reduced by adding a fictitious error correction stress into the localization and aggregate response.

- The model, which only has 4 free parameters, predicts resulting ratcheting strains which are qualitatively and quantitatively correct[14].

- The EiVPSC model predicts thermal ratcheting to be rate insensitive across two orders of magnitude in heating and cooling rate.

- The temperature sensitivity of the plastic flow was critical to predict ratcheting. Furthermore, the temperature sensitivity needed to be quite drastic.

- Increasing the rate sensitivity exponent increases the amount of predicted ratcheting, but

was predicted at values of *n* as low as 2. As such, more detailed experiments are needed to determine this parameter and investigate potential deformation mechanisms.

- The level of predicted ratcheting was not sensitive to the flow/threshold stress parameter, as compared to the rate and temperature sensitivity parameters.

- The model predicts that textures can be too strong or weak to induce thermal ratcheting, which provides a good sanity check of the model.

- The peak ratcheting, when varying the texture strength, occurs at textures that are on the higher end of what would be experimentally achievable, so achieving the saturation level would likely be unattainable.

Chapter 8

Conclusions and Future Work

8.1 Conclusions

This dissertation presents progress in the understanding of the thermo-mechanical deformation of polycrystalline α-uranium. Three chapters have focused on the development of thermal stresses and their effects on mechanical deformation. One chapter analyzed deformation in the presence of hydrogen. The last two chapters focused on thermal ratcheting.

8.1.1 Development of Thermal Residual Stresses

It was seen the thermal residual stresses are much smaller then what would be predicted from the thermo-elastic calculation. In Chapter 2, it was seen that crystal plasticity models can be used to approximate the residual stress state that can then be used to predict subsequent deformation. In the 6th and 7th chapters, it is shown that the relaxation is likely due to an isotropic, rate-sensitive creep mechanisms, rather than the glide-based crystal plasticity mechanisms originally assumed. However, the magnitude and implications (considered in detail below) of those internal stresses remain unchanged.

8.1.2 In-situ Neutron Diffraction Insights on Mechanical Deformation

Two of the chapters of this dissertation focused on the deformation clock rolled α-uranium under uni-axial deformation. In both chapters, it was shown that the thermal residual stresses play a significant role in the activation of plastic mechanism, but do not drastically affect the macroscopic stress-strain response. The only difference seen in between the macroscopic curves is during the elasto-plastic transition. In Chapter 3, the predictive capabilities of the model are tested as the model was calibrated off of RD tension and compression and used to predict TD tension. In Chapter 5, the thermally activated nature of the slip modes was employed to show the shifts in mechanical response at elevated temperatures. An apparent increase in strength was observed in the {130} twinning with elevated temperatures, but EPSC modeling revealed this observation is explained by the shifts in thermal residual stresses.

8.1.3 Hydrogren Embrittlement in α-Uranium

In Chapter 4, it was shown that the activation of plastic mechanisms are not affected by the presence of hydrogen, and a transition from transgranular to intergranular cracking was observed with increasing hydrogen content, and it is speculated that the source of embrittlement was due to the formation of hydrides along the grain boundaries which lowers their cohesive strength.

8.1.4 Thermal Ratcheting

The use of polycrystalline thermo-elastic-plastic modeling plus in-situ neutron diffraction experiments revealed that: 1.) the thermal ratcheting can be explained through an isotropic plastic mechanism, and 2.) the thermo-elastic anisotropy alone (without plastic anisotropy) is sufficient to explain the ratcheting. A model was developed that qualitatively and quantitatively predicted ratcheting and explained the texture dependence of the ratcheting response. It was

seen that the temperature dependence of the plastic mechanisms was critical to predict any thermal ratcheting.

8.2 Future Work

As is typically the case in science, answering a question has lead to the creation of many more. Continued efforts on the twinning model, and better calibration of the residual stress model will improve upon the results presented in Chapters 2-6. The so-called Twinning-DeTwinning [47] model would be great place to start. As for the ratcheting, Chiswick's experiments were cutting edge at the time they were conducted and were very thorough. However, key measurements that are now standard practice would greatly increase the insights and the strength of the current modeling effort. Careful experiments on samples with known textures would allow for quantitative validation of the model. Postmortem microstructural characterization would glean valuable insights into the microstructure evolution, and determine the validity of a diffusional grain boundary mechanism, as this would lead to grain shape changes through cycling. Ideally, the modeling effort could be used to explain the thermal ratcheting seen in the so-called 'tailored thermal expansion' alloys [29].

Bibliography

[1] R. McCabe, L. Capolungo, P. Marshall, C. Cady, and C. Tomé, "Deformation of wrought uranium: Experiments and modeling," *Acta Materialia*, vol. 58, no. 16, pp. 5447–5459, 2010.

[2] J. Daniel, B. Lesage, and P. Lacombe, "The influence of temperature on slip and twinning in uranium," *Acta Metallurgica*, vol. 19, no. 2, pp. 163–173, 1971.

[3] E. Fisher and H. McSkimin, "Adiabatic elastic moduli of single crystal alpha-uranium," *Journal of Applied Physics*, vol. 29, no. 10, pp. 1473–1484, 1958.

[4] L. T. Lloyd, "Thermal expansion of alpha-uranium single crystals," *Journal of Nuclear Materials*, vol. 3, no. 1, pp. 67–71, 1961.

[5] J. Korn, "An investigation of the cones of zero expansion and thermal coefficients for single crystal of α-uranium," *Journal of Nuclear Materials*, vol. 71, no. 2, pp. 320–326, 1978.

[6] R. Cahn, "Plastic deformation of alpha-uranium; twinning and slip," *Acta metallurgica*, vol. 1, no. 1, pp. 49–70, 1953.

[7] M. Yoo, "Slip modes of alpha uranium," *Journal of Nuclear Materials*, vol. 26, no. 3, pp. 307–318, 1968.

[8] M. Knezevic, L. Capolungo, C. N. Tomé, R. A. Lebensohn, D. J. Alexander, B. Mihaila, and R. J. McCabe, "Anisotropic stress–strain response and microstructure evolution of textured α-uranium," *Acta Materialia*, vol. 60, no. 2, pp. 702–715, 2012.

[9] U. Kocks, C. Tomé, and H. Wenk, *Texture and Anisotropy*.

[10] A. Crocker, "The crystallography of deformation twinning in alpha-uranium," *Journal of Nuclear Materials*, vol. 16, no. 3, pp. 306–326, 1965.

[11] R. Field, R. McCabe, D. Alexander, and D. Teter, "Deformation twinning and twinning related fracture in coarse-grained α-uranium," *Journal of Nuclear Materials*, vol. 392, no. 1, pp. 105–113, 2009.

[12] E. Garlea, R. Bridges, V. O. Garlea, D. Carpenter, M. Hemphill, and J. Morrell, "Characterization of a grain size refinement process in cast uranium," *Materials Science and Engineering: A*, vol. 559, pp. 210–216, 2013.

[13] J. W. Christian and S. Mahajan, "Deformation twinning," *Progress in materials science*, vol. 39, no. 1, pp. 1–157, 1995.

[14] H. Chiswick, "The plastic deformation of uranium on thermal cycling," *Transactions of the ASM*, vol. 38, pp. 622–654, 1956.

[15] K. Merckx and K. Wheeler, "Deformation of uranium under constant load and cyclic temperature," *Journal of Basic Engineering (US) Divided into J. Eng. Mater. Technol. and J. Fluids Eng.*, vol. 83, 1962.

[16] J. Kench, J. Chamberlain, and A. Young, "Incremental collapse in α-uranium subjected to thermal cycles while undergoing creep," *Journal of Nuclear Materials*, vol. 7, no. 2, pp. 165–181, 1962.

[17] W. Blackburn, G. Harnby, and J. Stow, "The effect of thermal cycling on the creep of uranium," *Journal of Nuclear Energy. Part A. Reactor Science*, vol. 12, no. 4, pp. 162–171, 1960.

[18] A. Bochvar and G. Tomson, "Formation of porosity in uranium under the action of thermal cycling," *The Soviet Journal of Atomic Energy*, vol. 2, no. 6, pp. 637–643, 1957.

[19] R. Lebensohn and C. Tomé, "A self-consistent anisotropic approach for the simulation of plastic deformation and texture development of polycrystals: application to zirconium alloys," *Acta metallurgica et materialia*, vol. 41, no. 9, pp. 2611–2624, 1993.

[20] P. Turner and C. Tomé, "A study of residual stresses in zircaloy-2 with rod texture," *Acta metallurgica et Materialia*, vol. 42, no. 12, pp. 4143–4153, 1994.

[21] B. Clausen, C. Tomé, D. Brown, and S. Agnew, "Reorientation and stress relaxation due to twinning: modeling and experimental characterization for mg," *Acta Materialia*, vol. 56, no. 11, pp. 2456–2468, 2008.

[22] H. Wang, P. Wu, C. Tomé, and Y. Huang, "A finite strain elastic–viscoplastic self-consistent model for polycrystalline materials," *Journal of the Mechanics and Physics of Solids*, vol. 58, no. 4, pp. 594–612, 2010.

[23] J. Hutchinson, "Elastic-plastic behaviour of polycrystalline metals and composites," *Proceedings of the Royal Society of London. A. Mathematical and Physical Sciences*, vol. 319, no. 1537, pp. 247–272, 1970.

[24] U. Kocks and H. Mecking, "Physics and phenomenology of strain hardening: the fcc case," *Progress in Materials Science*, vol. 48, no. 3, pp. 171–273, 2003.

[25] I. Beyerlein and C. Tomé, "A dislocation-based constitutive law for pure zr including temperature effects," *International Journal of Plasticity*, vol. 24, no. 5, pp. 867–895, 2008.

[26] M. Knezevic, I. J. Beyerlein, D. W. Brown, T. A. Sisneros, and C. N. Tomé, "A polycrystal plasticity model for predicting mechanical response and texture evolution during strain-path changes: application to beryllium," *International Journal of Plasticity*, vol. 49, pp. 185–198, 2013.

[27] M. Bourke, D. Dunand, and E. Ustundag, "Smarts–a spectrometer for strain measurement in engineering materials," *Applied Physics A*, vol. 74, no. 1, pp. s1707–s1709, 2002.

[28] X.-L. Wang, T. Holden, G. Q. Rennich, A. Stoica, P. K. Liaw, H. Choo, and C. R. Hubbard, "Vulcan—the engineering diffractometer at the sns," *Physica B: Condensed Matter*, vol. 385, pp. 673–675, 2006.

[29] J. Monroe, D. Gehring, I. Karaman, R. Arroyave, D. Brown, and B. Clausen, "Tailored thermal expansion alloys," *Acta Materialia*, vol. 102, pp. 333–341, 2016.

[30] C. Calhoun, J. Wollmershauser, D. Brown, R. Mulay, E. Garlea, and S. Agnew, "Thermal residual strains in depleted α-u," *Scripta Materialia*, 2013.

[31] C. Calhoun, E. Garlea, T. Sisneros, and S. Agnew, "Effects of hydrogen on the mechanical response of α-uranium," *Journal of Nuclear Materials*, vol. 465, pp. 737–745, 2015.

[32] C. Calhoun, E. Garlea, R. Mulay, T. Sisneros, and S. Agnew, "Investigation of the effect of thermal residual stresses on deformation of α-uranium through neutron diffraction measurements and crystal plasticity modeling," *Acta Materialia*, vol. 85, pp. 168–179, 2015.

[33] D. Brown, M. Bourke, B. Clausen, D. Korzekwa, R. Korzekwa, R. McCabe, T. Sisneros, and D. Teter, "Temperature and direction dependence of internal strain and texture evolution during deformation of uranium," *Materials Science and Engineering: A*, vol. 512, no. 1, pp. 67–75, 2009.

[34] S. Rothman, J. Hines, J. Gray, and A. Harkness, "Anisotropy of self-diffusion in alpha uranium," *Journal of Applied Physics*, vol. 33, no. 6, pp. 2113–2116, 1962.

[35] M. Knezevic, R. J. McCabe, C. N. Tomé, R. A. Lebensohn, S. R. Chen, C. M. Cady, G. T. Gray III, and B. Mihaila, "Modeling mechanical response and texture evolution of α-uranium as a function of strain rate and temperature using polycrystal plasticity," *International Journal of Plasticity*, 2012.

[36] W. Hutchinson and M. Barnett, "Effective values of critical resolved shear stress for slip in polycrystalline magnesium and other hcp metals," *Scripta materialia*, vol. 63, no. 7, pp. 737–740, 2010.

[37] B. Raeisinia, S. R. Agnew, and A. Akhtar, "Incorporation of solid solution alloying effects into polycrystal modeling of mg alloys," *Metallurgical and Materials Transactions A*, vol. 42, no. 5, pp. 1418–1430, 2011.

[38] A. Young, K. Gardiner, and W. Rotsey, "The plastic deformation of alpha-uranium," *Journal of Nuclear Materials*, vol. 2, no. 3, pp. 234–247, 1960.

[39] E. Ruedl and S. Amelinckx, "Electron microscopic observation of dislocation networks and radiation damage in -uranium," *Journal of Nuclear Materials*, vol. 9, no. 1, pp. 116 – 119, 1963.

[40] E. Garlea, H. Choo, G. Y. Wang, P. K. Liaw, B. Clausen, D. W. Brown, J. Park, P. D. Rack, and E. A. Kenik, "Hydride-phase formation and its influence on fatigue crack propagation behavior in a zircaloy-4 alloy," *Metallurgical and Materials Transactions A*, vol. 41, no. 11, pp. 2816–2828, 2010.

[41] M. Knezevic, R. J. McCabe, R. A. Lebensohn, C. N. Tomé, C. Liu, M. L. Lovato, and B. Mihaila, "Integration of self-consistent polycrystal plasticity with dislocation density

based hardening laws within an implicit finite element framework: application to low-symmetry metals," *Journal of the Mechanics and Physics of Solids*, vol. 61, no. 10, pp. 2034–2046, 2013.

[42] H.-R. Wenk, L. Lutterotti, and S. Vogel, "Texture analysis with the new {HIPPO} {TOF} diffractometer," *Nuclear Instruments and Methods in Physics Research Section A: Accelerators, Spectrometers, Detectors and Associated Equipment*, vol. 515, no. 3, pp. 575 – 588, 2003.

[43] X.-L. Wang, Y. Wang, and J. Richardson, "Experimental error caused by sample displacement in time-of-flight neutron diffractometry," *Journal of applied crystallography*, vol. 35, no. 5, pp. 533–537, 2002.

[44] E. Garlea, B. Clausen, E. Kenik, D. Ciurchea, S. Vogel, J. Pang, and H. Choo, "Intergranular strain evolution in a zircaloy-4 alloy with basketweave morphology," *Metallurgical and Materials Transactions A*, vol. 41, no. 5, pp. 1255–1260, 2010.

[45] M. Daymond, M. Bourke, R. Von Dreele, B. Clausen, and T. Lorentzen, "Use of rietveld refinement for elastic macrostrain determination and for evaluation of plastic strain history from diffraction spectra," *Journal of Applied Physics*, vol. 82, no. 4, pp. 1554–1562, 1997.

[46] R. Hill, "Continuum micro-mechanics of elastoplastic polycrystals," *Journal of the Mechanics and Physics of Solids*, vol. 13, no. 2, pp. 89–101, 1965.

[47] H. Wang, P. Wu, C. Tomé, and J. Wang, "A constitutive model of twinning and detwinning for hexagonal close packed polycrystals," *Materials Science and Engineering: A*, vol. 555, pp. 93–98, 2012.

[48] D. Brown, S. Agnew, M. Bourke, T. Holden, S. Vogel, and C. Tomé, "Internal strain and texture evolution during deformation twinning in magnesium," *Materials Science and Engineering: A*, vol. 399, no. 1, pp. 1–12, 2005.

[49] C. Aydiner, J. Bernier, B. Clausen, U. Lienert, C. Tomé, and D. Brown, "Evolution of stress in individual grains and twins in a magnesium alloy aggregate," *Physical Review B*, vol. 80, no. 2, p. 024113, 2009.

[50] H. El Kadiri and A. Oppedal, "A crystal plasticity theory for latent hardening by glide twinning through dislocation transmutation and twin accommodation effects," *Journal of the Mechanics and Physics of Solids*, vol. 58, no. 4, pp. 613–624, 2010.

[51] H. Wang, B. Raeisinia, P. Wu, S. Agnew, and C. Tomé, "Evaluation of self-consistent polycrystal plasticity models for magnesium alloy az31b sheet," *International Journal of Solids and Structures*, vol. 47, no. 21, pp. 2905–2917, 2010.

[52] H. K. Birnbaum and P. Sofronis, "Hydrogen-enhanced localized plasticity—a mechanism for hydrogen-related fracture," *Materials Science and Engineering: A*, vol. 176, no. 1, pp. 191–202, 1994.

[53] R. P. Gangloff, "Hydrogen assisted cracking of high strength alloys," DTIC Document, Tech. Rep., 2003.

[54] C. Coleman and J. Ambler, "Solubility of hydrogen isotopes in stressed hydride-forming metals," *Scripta Metallurgica*, vol. 17, no. 1, pp. 77–82, 1983.

[55] D. Shih, I. Robertson, and H. Birnbaum, "Hydrogen embrittlement of α titanium:*in situ* tem studies," *Acta Metallurgica*, vol. 36, no. 1, pp. 111–124, 1988.

[56] N. Magnani, "Hydrogen embrittlement and stress corrosion cracking of uranium and uranium alloys," *Advances in Corrosion Science and Technology*, vol. 6, pp. 81–161, 1976.

[57] R. Rundle, "The structure of uranium hydride and deuteride1," *Journal of the American Chemical Society*, vol. 69, no. 7, pp. 1719–1723, 1947.

[58] A. Hughes, S. Orman, and G. Picton, "The embrittlement of u by h 2 o and hydrogen," *Corrosion Science*, vol. 10, no. 4, pp. 239–244, 1970.

[59] C. Beevers and G. Newman, "Hydrogen embrittlement in uranium," *Journal of Nuclear Materials*, vol. 23, no. 1, pp. 10–18, 1967.

[60] J. Bingert, R. Hanrahan Jr, R. Field, and P. Dickerson, "Microtextural investigation of hydrided α-uranium," *Journal of alloys and compounds*, vol. 365, no. 1, pp. 138–148, 2004.

[61] S. Spooner, G. Ludtka, J. Bullock, R. Bridges, and G. Powell, "Sans measurement of hydrides in uranium," Oak Ridge Y-12 Plant, TN (US), Tech. Rep., 2001.

[62] J. Huddart, J. Harding, and P. Bleasdale, "The effect of strain rate on the tensile flow and fracture of α-uranium," *Journal of Nuclear Materials*, vol. 89, no. 2, pp. 316–330, 1980.

[63] G. L. Powell, "The uranium–hydrogen binary system," in *Uranium Processing and Properties*. Springer, 2013, pp. 173–188.

[64] J. Pehl, S. Matthies, H. Wenk, L. Lutterotti, and S. C. Vogel, "Quantitative texture analysis with the hippo tof diffractometer," in *Materials Science Forum*, vol. 495. Trans Tech Publ, 2005, pp. 113–118.

[65] R. Hielscher and H. Schaeben, "A novel pole figure inversion method: specification of the mtex algorithm," *Journal of Applied Crystallography*, vol. 41, no. 6, pp. 1024–1037, 2008.

[66] D. Brown, M. Bourke, C. Tomé, R. Varma, T. Holden, and B. Clausen, "A neutron diffraction and modeling study of uniaxial deformation in polycrystalline beryllium," *Metallurgical and Materials Transactions A*, vol. 34, no. 7, pp. 1439–1449, 2003.

[67] P. Rangaswamy, M. A. Bourke, D. W. Brown, G. C. Kaschner, R. B. Rogge, M. G. Stout, and C. N. Tomé, "A study of twinning in zirconium using neutron diffraction and polycrystalline modeling," *Metallurgical and Materials Transactions A*, vol. 33, no. 13, pp. 757–763, 2002.

[68] R. Mulay, B. Clausen, and S. Agnew, "In-situ neutron diffraction study of the bauschinger effect in b2 structured cozr," *Metallurgical and Materials Transactions A*, vol. 42, no. 1, pp. 60–70, 2011.

[69] W. Blackburn, "The effect of internal stresses due to irradiation growth and thermal cycling on the creep of uranium, in the cases of both elastic and plastic behaviour," *Journal of Nuclear Energy. Parts A/B. Reactor Science and Technology*, vol. 14, no. 1, pp. 107–116, 1961.

[70] T. Courtney, *Mechanical Behavior of Materials*.

[71] Y. Adda and A. Kirianenko, "Etude de l'autodiffusion de l'uranium en phase ," *Journal of Nuclear Materials*, vol. 6, no. 1, pp. 130 – 134, 1962. [Online]. Available: http://www.sciencedirect.com/science/article/pii/0022311562902246

[72] R. McCabe, A. Richards, C. DR, K. Clarke, I. Beyerlein, and M. Knezevic, "Microstructure effects on the recrystallization of low-symmetry alpha-uranium," *Journal of Nuclear Materials*, vol. 465, pp. 189–195, 2015.

[73] B. Hatt, "The orientation relationship between the gamma and alpha structures in uranium-zirchonium alloys," *Journal of Nuclear Materials*, vol. 19, pp. 133–141, 1966.

[74] T. G. Langdon, "Grain boundary sliding revisited: Developments in sliding over four decades," *Journal of Materials Science*, vol. 41, no. 3, pp. 597–609, 2006.

[75] A. Molinari, S. Ahzi, and R. Kouddane, "On the self-consistent modeling of elastic-plastic behavior of polycrystals," *Mechanics of Materials*, vol. 26, pp. 43–62, 1997.

[76] H. Qiao, P. Wu, H. Wang, M. Gharghouri, and M. Daymond, "Evaluation of elastic–viscoplastic self-consistent polycrystal plasticity models for zirconium alloys," *International Journal of Solids and Structures*, vol. 71, pp. 308–322, 2015.

Appendix A

Derivations of Necessary Equations

Proof of Equation 7.7 Derivation of the Tangent Modulus

$$S_{ij} = \sigma_{ij} - \frac{\delta_{ij}}{3}\sigma_{kk} \tag{A.1}$$

$$\sigma_v = \sqrt{\frac{3}{2}S_{ij}S_{ij}} \tag{A.2}$$

$$\dot{\varepsilon}_p = A\left(\sigma_v\right)^{n-1} S_{ij} \tag{A.3}$$

$$\mathbf{M}^p_{ijkl} = \frac{\partial \dot{\varepsilon}_p}{\partial \sigma} = A\left[\left(\sigma_v\right)^{n-1}\frac{\partial S_{ij}}{\partial \sigma_{kl}} + S_{ij}\left(\frac{\partial}{\partial \sigma_{kl}}\left(\left(\sigma_v\right)^{n-1}\right)\right)\right] \tag{A.4}$$

Break this expression into two terms $(\sigma_v)^{n-1} \frac{\partial S_{ij}}{\partial \sigma_{kl}}$ and $S_{ij}\left(\frac{\partial}{\partial \sigma_{kl}}\left((\sigma_v)^{n-1}\right)\right)$. First term:

$$(\sigma_v)^{n-1} \frac{\partial S_{ij}}{\partial \sigma_{kl}} = (\sigma_v)^{n-1} \frac{\partial}{\partial \sigma_{kl}}\left(\sigma_{ij} - \frac{\delta_{ij}}{3}\sigma_{nn}\right) \tag{A.5}$$

$$= (\sigma_v)^{n-1}\left(\frac{\partial \sigma_{ij}}{\partial \sigma_{kl}} - \frac{\delta_{ij}}{3}\frac{\partial \sigma_{nn}}{\partial \sigma_{kl}}\right) \tag{A.6}$$

$$= (\sigma_v)^{n-1}\left(I_{ijkl} - \frac{\delta_{ij}\delta_{kl}}{3}\right) \tag{A.7}$$

Now the second term $S_{ij}\left(\frac{\partial}{\partial \sigma_{kl}}\left((\sigma_v)^{n-1}\right)\right)$:

$$S_{ij}\left(\frac{\partial}{\partial \sigma_{kl}}\left((\sigma_v)^{n-1}\right)\right) = S_{ij}(n-1)(\sigma_v)^{n-2}\frac{\partial \sigma_v}{\partial \sigma_{kl}} \tag{A.8}$$

$$= S_{ij}(n-1)(\sigma_v)^{n-2}\frac{\partial}{\partial \sigma_{kl}}\left(\frac{3}{2}S_{mn}S_{mn}\right)^{\frac{1}{2}} \tag{A.9}$$

$$= \frac{3}{4}S_{ij}(n-1)(\sigma_v)^{n-2}\left(\frac{3}{2}S_{mn}S_{mn}\right)^{-\frac{1}{2}}\frac{\partial}{\partial \sigma_{kl}}S_{mn}S_{mn} \tag{A.10}$$

$$= \frac{3}{4}S_{ij}(n-1)(\sigma_v)^{n-3}\frac{\partial}{\partial \sigma_{kl}}S_{mn}S_{mn} \tag{A.11}$$

$$= \frac{3}{4}S_{ij}(n-1)(\sigma_v)^{n-3}(2S_{kl}) \tag{A.12}$$

$$= \frac{3}{2}S_{ij}S_{kl}(n-1)(\sigma_v)^{n-3} \tag{A.13}$$

To get from A.11 to A.12

$$\frac{\partial}{\partial \sigma_{kl}} S_{mn} S_{mn} = \frac{\partial}{\partial \sigma_{kl}} \left(\left(\sigma_{ij} - \frac{\delta_{ij}}{3} \sigma_{kk} \right) \left(\sigma_{ij} - \frac{\delta_{ij}}{3} \sigma_{kk} \right) \right) \tag{A.14}$$

$$= \frac{\partial}{\partial \sigma_{kl}} \left(\sigma_{ij} \sigma_{ij} - \frac{2}{3} \delta_{ij} \sigma_{ij} \sigma_{kk} + \frac{\delta_{ij} \delta_{ij}}{9} \sigma_{kk} \sigma_{kk} \right) \tag{A.15}$$

$$= \frac{\partial}{\partial \sigma_{kl}} \left(\sigma_{ij} \sigma_{ij} - \frac{2}{3} \sigma_{jj} \sigma_{kk} + \frac{\sigma_{kk} \sigma_{kk}}{3} \right) \tag{A.16}$$

$$= \frac{\partial}{\partial \sigma_{kl}} \left(\sigma_{ij} \sigma_{ij} - \frac{\sigma_{kk} \sigma_{kk}}{3} \right) \tag{A.17}$$

$$= 2\sigma_{kl} - \frac{2}{3} \delta_{kl} \sigma_{mm} \tag{A.18}$$

$$= 2 \left(\sigma_{kl} - \delta_{kl} \sigma_{mm} \right) \tag{A.19}$$

$$= 2 S_{kl} \tag{A.20}$$

When we combine A.7 and A.13

$$\mathbf{M}^p_{ijkl} = \frac{\partial \dot{\varepsilon}_p}{\partial \sigma} = A \left(\frac{3 S_{ij} S_{kl} (n-1)}{2} \sigma_v^{n-3} + (I_{ijkl} - \frac{\delta_{kl} \delta_{ij}}{3}) \sigma_v^{n-1} \right) \tag{A.21}$$